

AKARI and Spinning Dust Emission

A look at microwave dust emission via the Infrared

Doctoral Thesis

Submitted to The University of Tokyo

DRAFT

Aaron Christopher Bell

December 13, 2017

# Contents

1	2	<b>Abstract</b>	vii
3	3	<b>1 Introduction</b>	1
4	1.1 All-sky Astronomy . . . . .	1	
5	1.2 Infrared astronomy . . . . .	1	
6	1.3 Microwave foregrounds . . . . .	4	
7	1.3.1 Anomalous Microwave Emission . . . . .	5	
8	1.3.2 Proposed explanations . . . . .	8	
9	1.3.3 Excitation factors . . . . .	10	
10	1.3.4 AME vs. IR in the literature . . . . .	11	
11	1.4 Scope of this Dissertation . . . . .	12	
12	1.4.1 An application of all-sky archival data . . . . .	12	
13	1.4.2 Testing the spinning PAH hypothesis . . . . .	12	
14	1.4.3 Limitations . . . . .	12	
15	1.4.4 Code availability . . . . .	13	
16	<b>2 Data Sources</b>	14	
17	2.1 A collection of skies . . . . .	14	
18	2.2 AKARI . . . . .	16	
19	2.2.1 AKARI/Infrared Camera (IRC) . . . . .	16	
20	2.2.2 The AKARI Far Infrared Surveyor (FIS) . . . . .	21	
21	2.2.3 Planck Observatory High Frequency Instrument (HFI) . . . . .	21	
22	2.3 Infrared Astronomical Satellite (IRAS) . . . . .	22	
23	2.4 Planck COMMANDER Parameter Maps . . . . .	23	
24	2.4.1 Synchrotron . . . . .	23	
25	2.4.2 Free-free emission . . . . .	25	
26	2.4.3 Thermal dust emission . . . . .	25	
27	2.4.4 AME data . . . . .	25	
28	2.5 All-sky Data Processing . . . . .	31	
29	<b>3 Analysis of an interesting AME region: <math>\lambda</math> Orionis</b>	32	
30	3.1 An interesting AME region . . . . .	32	
31	3.1.1 Where does the ring come from? . . . . .	32	
32	3.1.2 A well-studied region . . . . .	33	
33	3.2 Investigative approach . . . . .	33	
34	3.3 Data preparation . . . . .	36	
35	3.3.1 Extraction from HEALPix maps . . . . .	36	
36	3.3.2 Point-source and artifact masking . . . . .	36	
37	3.3.3 PSF Smoothing . . . . .	37	
38	3.3.4 Background subtraction . . . . .	40	
39	3.4 Multi-wavelength characterization . . . . .	40	
40	3.4.1 Bootstrap analysis . . . . .	43	

41	3.5 Comparison with SED Fitting . . . . .	43
42	3.5.1 Comparison with unmasked results . . . . .	45
43	3.6 Discussion . . . . .	53
44	3.6.1 PAH Ionization fraction . . . . .	53
45	<b>4 All-sky Analysis</b>	<b>56</b>
46	4.1 Resolution matching . . . . .	56
47	4.2 All-sky cross correlations . . . . .	57
48	4.3 Masked Comparison . . . . .	60
49	4.3.1 Pixel mask . . . . .	60
50	4.3.2 Effect of mask application . . . . .	62
51	4.4 Spatial variation of correlations . . . . .	66
52	4.5 Discussion . . . . .	69
53	4.5.1 AME and interstellar radiation fields . . . . .	70
54	4.5.2 Microwave foreground component separation . . . . .	70
55	4.5.3 Optical depth . . . . .	72
56	4.5.4 Comparison of $\lambda$ Orionis vs. All-sky results . . . . .	73
57	4.5.5 Implications of an absent PAH-AME correlation . . . . .	73
58	4.6 Future Works . . . . .	74
59	<b>5 Summary</b>	<b>76</b>

# 60 List of Figures

61	1.1	An example of a potential makueup of microwave emission components. Photometry 62 points are extracted from the Planck and WMAP all-sky maps (Planck Collaboration 63 et al. 2014b), for a part of the region well-known for prominent AME, $\rho$ Ophiuchus 64 (Planck Collaboration et al. 2011b). The AME curve is produced from a warm neu- 65 tral medium spinning dust template (Ali-Haïmoud et al. 2009), with a frequency-shift 66 applied to approximately fit the microwave data s in Planck Collaboration et al. (2016b) . . . . .	6
67	1.2	Two AME prominent regions investigated by Planck Collaboration et al. (2011b); Tibbs 68 et al. (2011), $\rho$ Ophiuchus and Perseus, as they appear in the PAH-feature-tracing 69 AKARI/IRC 9 $\mu\text{m}$ all-sky data at native resolution (Ishihara et al. 2010). White con- 70 tours show AME at 1-degree resolution, extracted from the map by Planck Collabo- 71 ration et al. (2016b). The IRC data shown here is of a much finer resolution than 72 the AME data, at around 10'', demonstrating the critical gap in resolvability of all-sky 73 AME-tracing data itself vs. the IR dust tracers we hope to compare it to. . . . .	7
74	2.1	Relative spectral response curves of the bands used in this study. Expected dust emis- 75 sion components, assuming the dust SED model by (Compiègne et al. 2011) are also 76 shown. The components are summarized as emission from big grains (BGs, dashed 77 yellow line), emission from very small grains (VSGs, dashed blue line), and emission 78 from PAHs (dashed grey line). . . . .	15
79	2.2	The I12 (orange) and A9 (green) filters coverage of modeled ionized (PAH1, red) and 80 neutral (PAH0, purple)components of PAH features by Compiègne et al. (2011). The 81 difference in the PAH feature coverage mainly comes from the 6.2 $\mu\text{m}$ and the 7.7 $\mu\text{m}$ 82 feature. . . . .	17
83	2.3	Coverage of MIR wavelengths by the filters used in this work. An Spitzer/IRS spectrum 84 (see AOT4119040) of the galactic plane (thin blue line) demonstrates how IRC and 85 IRAS photometric bands trace these features on an all-sky basis (Ishihara et al. 2007). 86 Strong PAH features overlap with the A9 and I12, while the A18 and I25 micron bands 87 only trace much weaker features. . . . .	18
88	2.4	In-band contributions from charged (PAH1) neutral (PAH0) PAHs, to the emission 89 detected by the I12 and A9 filters. These assume a model galactic cirrus spectrum 90 simulated with the SED template of Compiègne et al. (2011). . . . .	19
91	2.5	Ionization fraction of PAHs vs. band ratios of I12, I25, to A9, for two ISRF strengths: 92 Top: $U = 1$ , Bottom: $U = 10$ . These ratios are determined by assuming the SED 93 template of Compiègne et al. (2011) . . . . .	20
94	2.6	AKARI/IRC 9 $\mu\text{m}$ to IRAS 12 $\mu\text{m}$ intensity ratio. . . . .	21
95	2.7	AKARI/IRC 9 $\mu\text{m}$ to IRAS 25 $\mu\text{m}$ intensity ratio. . . . .	22
96	2.8	$r_s$ cross correlation matrix of the PCCS maps: temperature $T$ , emissivity index $\beta$ , and 97 amplitude at 545 GHz $I_{dust}(545)$ of thermal dust; intensity of free-free emission $ff$ at 98 ; intensity of synchrotron emisison at 4 MHz $Sync$ ; intensity of the AME var. freq. 99 component $AME$ at 22.8 GHz. . . . .	24
100	2.9	The peak frequencies of the varying component $AME_{var}$ . The pink shaded region 101 indicates frequencies not covered by either WMAP or Planck The green line at 33.5 GHz 102 indicates the peak frequency of $AME_{fix}$ . . . . .	26

103	2.10	Histograms of the peak intensity AME maps calculated from the original COMMANDER-AME reference frequency maps. The dominant component, $AME_{var}$ is indicated in blue, for all pixels in the map, with their spinning dust intensities evaluated their peak frequencies (see Fig. 2.9.) $AME_{fix}$ gives the peak intensity of the spatially-constant frequency component, indicating it is essentially always the weaker component. . . . .	27
104	2.11	All-sky map of the peak frequencies of the varying component $AME_{var}$ , corresponding to Fig. 2.9. Virtually all of the purple regions of the map correspond to pixels flagged for point sources in the LFI data. There are very few notable structures in the frequency map overall, other than the galactic plane itself, $\rho$ Ophiuchus, and Perseus. . . . .	28
105	2.12	Spdust template spinning dust profiles fitted by PC15X when calculating $AME_{var}$ . The reference frequency, 22.8 GHz is indicated by the vertical green line. Each template has the same $AME_{var}$ amplitude of 100 $\mu$ K, indicated by the horizontal green line, plotted to highlight the potential deviation between $AME_{var}$ and the actual peak intensity. . . . .	29
106	2.13	All-sky map of the ratio of two COMMANDER components- the frequency-varying AME component divided by the intensity of thermal dust emission at 545 GHz. There are some recognizable AME emission regions, such as $\lambda$ Orionis. Large-scale patches of AME excess are noted to correspond to synchrotron emission (Hensley et al. 2016) . . . . .	30
110	3.1	$\lambda$ Orionis as it appears in the AKARI 9 $\mu$ m data. Contours indicate the AME, as given by the Planck PR2 AME map. The image is smoothed to a 1° PSF (much larger than the original 10 arcsec map). The $\lambda$ Orionis star itself is approximately located at the center of the image. . . . .	34
114	3.2	$\lambda$ Orionis as it appears in H-alpha emission by Finkbeiner (2003). Contours indicate AME emission, from the variable frequency component. The colorbar indicates $H\alpha$ emission in Rayleighs. The field of view is slightly larger than that used for the final processed IR comparison (Fig. 3.6). . . . .	35
118	3.3	The $\lambda$ Orionis region and its surroundings in AKARI FIS data, where A65 is blue, A90 is green, and A140 is red. The missing stripe patterns are visible, and affect all 3 bands shown here as well as the A160 data. . . . .	37
122	3.4	The $\lambda$ Orionis region in the A9 band at near-native resolution. This is a mosaic created from the 3x3 degree all-sky survey tiles by Ishirara et al. (in prep.) Missing stripes are less of a problem than with the A18 band (Fig. 3.5), but point sources are more pronounced. Betelgeuse, in the lower left of the image, is bright enough in this band to produce a ring-shaped artifact. . . . .	38
126	3.5	The $\lambda$ Orionis region in the A18 band at near-native resolution, demonstrating the regions affected by missing stripe errors, but less affected by point-sources than A9 (Fig. 3.4). . . . .	39
130	3.6	Processed data at each wavelength for $\lambda$ Orionis. A flat background has been subtracted from each frame based on the mean of pixels within the red rectangle. The pixel width is 0.25°, with the data PSF smoothed to 1° spatial resolution. Masked pixels (point sources, stripe errors, convolution artifacts) are shown as white. The frames share the same FOV and GAL-TAN projection. Colorbars indicate the intensity in MJy/sr. . . . .	41
134	3.7	$r_s$ correlation matrix for all of the data used in the $\lambda$ Orionis analysis, similar to that presented for the Planck Commander component maps in Fig. 2.8. The shade and annotation for each cell indicates the $r_s$ score, where $r_s$ of 1 indicates a monotonically increasing relationship for a given pair of images. The two AME components, as described in Ch. 2, are listed separately: $AME_{var}$ for the frequency-varying component, and $AME_{fix}$ for the constant frequency component. . . . .	42
138	3.8	Re-sampled (Bootstrap) correlation tests for IR emission in $\lambda$ Orionis vs. AME, for both $r_p$ (upper) and $r_s$ (lower) cases. Each band's $r$ distribution is shown in a different color (the same color scheme for both plots). The width of the distribution indicates the error for the given data in the correlation coefficient. The mean and standard deviation of the scores are given in the legend of each plot. The plot ranges only show positive values, since no negative scores were produced. . . . .	44
142			
146			
150			
154			

156	3.9	Observed (black circles and errors) and synthetic photometry (gray dots) SED of a pixel within $\lambda$ Orionis, along with the dust SED model fit results. Two SED fits are shown: on for the Bayesian fitting (magenta), and another showing the standard least-squares result for comparison (yellow). The fitted ISRF strength $U$ , and fraction of mass in PAHs, $q_{PAH}$ are also given. . . . .	46
157	3.10	The same as Fig. 3.9, but for a different pixel position. Corresponds to galactic coordinates. . . . .	47
158	3.11	Scatter plot with error ellipses generated through the Bayesian SED fitting, of total dust mass $M_{dust}$ vs. $I_{AME}$ scaled by $U$ . . . . .	48
159	3.12	The same comparison is given by 3.11, but showing total mass of PAHs ( $M_{PAH}$ ) rather than total dust mass on the y-axis. . . . .	49
160	3.13	The same as in Figs. 3.11 and 3.12 , but specifically comparing an estimate of the charged component of PAH mass $M_{PAH+}$ . This includes anions and cations, since we cannot distinguish between these two spectroscopically. . . . .	50
161	3.14	A grid of thumbnails showing the $\lambda$ Orionis region's structure, at 12 wavelengths, along with AME contours (shown in white countours. Spatial correlation seems to be the best at the shortest and longest wavelengths (AKARI/IRC 9 $\mu m$ and Planck/HFI 550 $\mu m$ ). The images are only smoothed and interpolated, for demonstration of the effects with- out other image processing steps (i.e. background subtraction, point source masking). Figure 3.1 demonstrates the actual pixel grid used for the SED fitting and intensity correlation tests. . . . .	51
162	3.15	Intensity cross-correlation for all pixels in the $\lambda$ Orionis cut-out region. $r_s$ indicates the Spearman rank correlation coefficient for each plot. . . . .	52
163	3.16	The Bayesian correlation probability distributions of Pearson's $\rho$ ) for the three physical parameters vs. the AME intensity: total dust mass, $\rho_{dust}$ (red); total PAH mass $\rho_{PAH}$ (green); and only the ionized PAH mass $\rho_{PAH+}$ (blue). Also given are the probabilities of either PAH component being better correlated with AME than dust mass, as well as the probability that ionized PAH mass correlates better than total PAH. 54	54
164	4.1	Point-density distributions of the log $AME_{var}$ intensity (Y-axis) vs. log IR bands' intensities. In this case no pixel mask is applied, in order to show overall trend of the full data-set. However a random sampling is used due to computational contraints. The plots show a random set of 20% of the full-sky data. Darker shaded regions indicate a higher density of pixels. . . . .	58
165	4.2	ALL-SKY cross-correlation matrix for the 12 infrared bands sampled, as well as the PC component maps described in Ch. 2: the two AME components evaluated at their peak frequencies $AME_{var}$ , $AME_{fix}$ ; Syncrotron, and free-free), and ancilliary maps of $N_H$ , $H\alpha$ emission, and 408 MHz emission Haslam et al. (1982). The color-scale indicates ( $r_s$ ). Results are based on the unmasked sky, but are split by Galactic latitude: pixels with $ \beta  < 15^\circ$ (left) and $ \beta  > 15^\circ$ (right). The color and annotations indicate $r_s$ as in Fig. 3.7. . . . .	59
166	4.3	All-sky map in A9 emission after applying the combined masks: ecliptic plane, galactic plane, point sources, and pixels with $S/N < 3$ . This mask essentially outlines the galaxy, except for the most confused regions. Diffuse galactic emission is essentially removed by the mask due to low S/N in the MIR bands. In the full sky map of $\sim 700,000$ pixels, there are $\sim 50,000$ unmasked pixels remaining. . . . .	60
167	4.4	The same comparison as shown for Fig. 4.1, but with the mask applied as in Fig. 4.3.	62
168	4.5	Cross-correlation ( $r_s$ matrix for the IR intensities (unscaled) vs. each other, esssentially the same comparison as in Fig. 4.2, except that the pixel mask is applied, and we do not perform a split by Galactic latitude— after the mask is applied, over 90% of pixels are within $10^\circ$ of the galactic plane. . . . .	63
169	4.6	Cross-correlation ( $r_s$ matrix for the $U$ -normalized IR intensities vs. each other, and also against the AME components, other PC products, and ancilliary data. In the left panel, only the IR maps are divided by $U$ - other data is unchanged from. In the panel at right, both the the AME and IR intensities are divided by $U$ . Fig. 4.5) . . . . .	64

---

210	4.7	Cross-correlation ( $r_s$ matrix for the residual correlations between IR intensities, AME, and other microwave components. All of the maps in this case are normalized by $R$ . )	65
211	4.8	Re-sampled (Bootstrap) correlation tests for IR emission vs. AME, performed on the masked all-sky maps. Each band's $r_s$ distribution is shown in a different color. The width of the distribution indicates the error for the given data in the correlation coefficient. The mean and standard deviation of the scores are given in the legend of each plot. The plot ranges only show positive values, since no negative scores were produced.	66
212	4.9	Spatial map of $r_s$ between the AME and IR intensity for A9. $r_s$ is calculated for all NSIDE 256 pixels within each NSIDE 8 pixel-sized bin. The correlation score is calculated with the unmasked maps. The colorbar indicates $r_s$ , ranging from -1 (negative monotonic relationship) to +1 (positive monotonic relationship).	67
213	4.10	Spatial map of $r_s$ between the AME and IR intensity for I12, calculated as in Fig. 4.9.	67
214	4.11	Spatial map of $r_s$ between the AME and IR intensity for I25, calculated as in Fig. 4.9.	67
215	4.12	Spatial map of $r_s$ between the AME and IR intensity for A140, calculated as in Fig. 4.9.	68
216	4.13	Spatial map of $r_s$ between the AME: $U$ and A9: $U$ , a tracer of the column density of PAHs emitting within the A9 filter. The correlations are calculated as in Fig. 4.9.	68
217	4.14	Spatial map of $r_s$ between the AME: $U$ and I12: $U$	68
218	4.15	Spatial map of $r_s$ between the AME: $U$ and A18: $U$	69
219	4.16	Spatial map of $r_s$ between the AME: $U$ and I25: $U$	69
220	4.17	The ratio of $AME_{var}$ and PC dust radiance $R$ , tracing fluctuations in AME per thermal dust emission. The contours trace the PC synchrotron (black) and free-free (white) components, to highlight various correlations between these components and PC AME fluctuations. Both free-free and synchrotron can be seen to correlate and anti-correlate with the AME to dust ratio.	71
221	4.18	The same as Fig. 4.17, but with $AME_{fix}/R$ as the all-sky image.	72
235	1	Explained variance decline for principal component analysis performed on a set of 12 all-sky infrared maps. The first three components account for over 99% of the total variance. The PCA fit is performed on the whole sky, after whitening the data, using the “scikitlearn	80
236			
237			
238			

<sup>239</sup> **Abstract**

<sup>240</sup> The anomalous microwave emission (AME) still lacks a conclusive explanation. This excess of  
<sup>241</sup> emission, roughly between 10 and 50 GHz, tends to defy attempts to explain it as synchrotron  
<sup>242</sup> or free-free emission. The overlap with frequencies important for cosmic microwae background  
<sup>243</sup> explorations, combined with a strong correlation with interstellar dust, drive cross-disciplinary  
<sup>244</sup> collaboration between interstellar medium and obervational cosmology. The apparent relation-  
<sup>245</sup> ship with dust has prompted a “spinning dust” hypothesis: electric dipole emission by rapidly  
<sup>246</sup> rotating, small dust grains. Magnetic dipole emission by grains with magnetic inclusions (“mag-  
<sup>247</sup> netic dust”), while less suppported, has not been ruled out. Even assuming a spinning dust  
<sup>248</sup> scenario, we are far from concluding which category of dust contributes. The typical peak  
<sup>249</sup> frequency range of the AME profile implicates grains on the order of 1nm. This points to poly-  
<sup>250</sup> cyclic aromatic hydrocarbon molecules (PAHs). We use data from the AKARI/Infrared Camera  
<sup>251</sup> (IRC)Onaka et al. (2007); Ishihara et al. (2010), due to its thorough PAH-band coverage, to  
<sup>252</sup> compare AME from the Planck Collaboration Planck Collaboration et al. (2016b). astrophysi-  
<sup>253</sup> cal component separation product) with infrared dust emission. We look also at infrared dust  
<sup>254</sup> emission from other mid IR and far-IR bands. The results and discussion contained here apply  
<sup>255</sup> to an angular scale of approximately 1°. In general, our results support an AME-from-dust  
<sup>256</sup> hypothesis. We look both at  $\lambda$  Orionis, a region highlighted for strong AME, and find that  
<sup>257</sup> certainly dust mass correlates with AME, and that PAH-related emission in the AKARI/IRC  
<sup>258</sup> 9  $\mu$ m band may correlate slightly more strongly. These results are compared to an all-sky  
<sup>259</sup> analysis, where we find that potential microwave emission component separation imperfections  
<sup>260</sup> among other issues, make an all-sky, delocalized comparsion very challenging. In any case the  
<sup>261</sup> AME-to-dust correlation persists even in the all-sky case, but tests of relative variations from  
<sup>262</sup> different dust SED components are largely inconclusive. We emphasize that future efforts to  
<sup>263</sup> understand AME should focus on individual regions, and a detailed comparsion of the PAH  
<sup>264</sup> features with the variation of the AME SED. Further all-sky analyses seem unlikely to help

265 resolve this issue. Non-PAH carriers of the AME, such as nanosilicates, cannot be ruled out

266 either.

<sup>267</sup> **Chapter 1**

<sup>268</sup> **Introduction**

<sup>269</sup>        *“It is now plain that about 75% of the data we would like to have can be obtained from  
270        good ground-based sites”*

<sup>271</sup>        -H. Johnson, 1966

<sup>272</sup> **1.1 All-sky Astronomy**

<sup>273</sup> All-sky astronomy is not new. Indeed, the notion of capturing a particular “object” or “source”  
<sup>274</sup> with a camera and saving it for later investigation would be completely alien to the first as-  
<sup>275</sup> tronomers and astronavigators. Absence of telescopes forced us to describe the sky in terms  
<sup>276</sup> of its larger patterns, brightest characters. What is new however is the notion of preparing an  
<sup>277</sup> archive of the sky itself for not only the research whims of a single investigator, team, insti-  
<sup>278</sup> tute, or even a single nation rather, all-sky surveys tend to be international endeavors in their  
<sup>279</sup> production, and even more so in their utilization.

<sup>280</sup> **1.2 Infrared astronomy**

<sup>281</sup> Infrared astronomy was essentially non-existent as recently as the 1920s, if we judge by the first  
<sup>282</sup> IR observations (Pettit & Nicholson 1922, 1928). Mainstream IR astronomy is perhaps much  
<sup>283</sup> younger, only really taking off — literally — in the post-war era, via balloon and rocket borne  
<sup>284</sup> experiments (Johnson 1966). Compare this to visible wavelengths, a field so old we name it  
<sup>285</sup> after the bio-evolutionary advent of sight, itself. Even radio astronomy with its own logistical  
<sup>286</sup> and technological challenges, has been around since at least 1932.

<sup>287</sup> Astronomers have not been content to be constrained by atmospheric IR windows, even

TABLE 1.1 Timeline of all-sky surveys

---

1983	IRAS	Neugebauer et al. (1984)
1989	COBE	Boggess et al. (1992)
1990	ROSAT	Truemper (1982)
2001	WMAP	Bennett et al. (2003b)
2003	2MASS	Skrutskie et al. (2006)
2003	GALEX	Martin et al. (2005)
2006	AKARI	Murakami et al. (2007)
2008	Fermi	Atwood et al. (2009)
2009	Planck	Planck Collaboration et al. (2011a)
2009	WISE	Wright et al. (2010)

288 from the best of ground-based sites. Or perhaps interests have shifted so dramatically since  
 289 1966, that all of the investigations enabled by rocket-based, space-based, even Boeing 747-  
 290 based IR astronomy (e.g. SOFIA, the Stratospheric Observatory for Infrared Astronomy, Young  
 291 et al. (2012)) would have bored 75% of astronomers in the '60s. The meaning of "far infrared"  
 292 has even redshifted, so to speak, from the Johnson (1966) definition of "4 to 22  $\mu\text{m}$ " — consider  
 293 the "Far Infrared Surveyor" instrument onboard the AKARI satellite (Murakami et al. 2007),  
 294 which observed from 50 to 180  $\mu\text{m}$  (Kawada et al. 2007a)

295 For our purposes, we consider the FIR to cover 60 to 550  $\mu\text{m}$ , partially out of convenience—  
 296 FIR bands, in this paper, means the Infrared Astronomical Satellite (IRAS) 60 and 100  $\mu\text{m}$   
 297 (Neugebauer et al. 1984), all four FIS bands, and the Planck Observatory's High Frequency  
 298 Instrument (HFI) 857 GHz and 545 GHz bands (Planck Collaboration et al. 2011a, 2014b).  
 299 The two AKARI Infrared Camera (IRC) (Onaka et al. 2007; Ishihara et al. 2010) bands and  
 300 the IRAS 12 and 25  $\mu\text{m}$  bands we will refer to collectively as the mid-infrared (MIR) bands.

301 The ability to map and archive the sky with satellites - not only in the optical and infrared,  
 302 but well into the microwave regime — has enabled interdisciplinary research of the ISM. The  
 303 merits of multiwavelength based investigations arise from the simple fact that the ISM is very  
 304 complex— both in terms of the myriad forms of matter present, from plasmas to dust grains —  
 305 and in countless physical processes at play. Consider the complex case of a supernova remnant  
 306 influencing surrounding ISM: through a combined analysis of radio, mid-far infrared, and X-ray  
 307 data, Lau et al. (2015) were able to characterize the history of dust production, heating, and  
 308 destruction within the Sgr A East supernova remnant.

In the case of interstellar dust emission, especially, multi-wavelength analysis is crucial to understanding the individual components of interstellar dust emission. If we assume that grains in local thermal equilibrium emit in an essentially classical manner, we will quickly become frustrated by multi-band IR observations. It is believed that factors such as variations in the optical properties of dust grains leads to a deviation from blackbody emission. The intensity of such emission has come to be represented by a “modified blackbody” function, provided in Onaka et al. (1999) as follows:

$$I_d(\nu) \propto \nu^{\beta_d} B_\nu(T_d), \quad (1.2.1)$$

where  $\beta$  is known as the “emissivity index”, and  $T_d$  is the dust temperature. Tracing this emission from microwave to IR wavelengths, in the diffuse Milky Way, Planck Collaboration et al. (2016d) find a typical value of  $1.6 \pm 0.1$  for  $\beta$ , and  $19.4 \pm 1.3$  K for the dust temperature (assuming a single temperature component).

Even after adopting a modified blackbody, we will still be unable to explain dust emission if we include wavelengths from the mid to Far-IR. A modified blackbody underestimates dust emission on the Wiens side, such as that traced by IRAS, an effect first reported by Boulanger et al. (1985), and also found later in data collected by the Cosmic Background Explorer (COBE)’s Diffuse Infrared Background Experiment (Sodroski et al. 1987, 1994). This excess cannot be explained by temperature variations of grains large enough to be in thermal equilibrium, and likely comes from a smaller population of interstellar dust grains (Purcell 1976; Sellgren 1984; Dwek 1986; Draine & Li 2001a).

From the mid-to-near IR however, spectroscopic observations enabled and required the simple-two populations model of larger and smaller dust (e.g. Mathis et al. (1977)), to be expanded. “Unidentified IR bands” from 3 to 11  $\mu\text{m}$  (hereafter, UIR bands), demonstrate another divergence from the canonical dust emission story. The UIR bands were first reported at 8 to 13  $\mu\text{m}$  in planetary nebulae and HII regions by Gillett et al. (1973, 1975) in ground-based observations. Observations by Merrill et al. (1975) noted another unexplained feature at 3.27  $\mu\text{m}$ , noting: “[...] similarities in the 8-13  $\mu\text{m}$  spectra of NGC 253, NGC 7027, and BD +30°3639 Gillett et al. (1975)”. Features at 6.2 and 7.7  $\mu\text{m}$  were reported by Russell et al. (1977) using the first airplane-mounted IR telescope and predecessor to SOFIA, the Kuiper Airborne Observatory. Sellgren et al. (1983) reported features at 3.3 and 3.4  $\mu\text{m}$  being detected in reflection nebulae.

339 From this point, the UIR bands become much less of property of select objects in targeted  
340 observations, are seen observed throughout the Milky Way. Balloon-based observation by Giard  
341 et al. (1994) confirmed that the  $3.3\ \mu\text{m}$  feature pervades throughout the Galactic plane. The  
342 first-ever airborne IR observatory, Kuiper Several years later, space-based spectroscopy with  
343 the Infrared Telescope in Space (IRTS)(Murakami et al. 1996) and Infrared Space Observatory  
344 (ISO)(Kessler et al. 1996) enabled confirmation by Onaka et al. (1996) and Mattila et al. (1996)  
345 that the mid-infrared UIR features are not limited to selection objects, but are present even  
346 in the diffuse galactic ISM by. Dwek et al. (1997) even reported that photometric excess in  
347 the COBE/DIRBE  $12\ \mu\text{m}$  band may be caused by the UIR bands, in and suggested they may  
348 be from these UIR features have come to be explained via polycyclic aromatic hydrocarbons  
349 (PAHs), a possibility which had been considered earlier by Allamandola et al. (1985); Puget  
350 et al. (1985). PAHs are a class of molecules composed primarily of fused carbon rings such as  
351 corannulene. PAHs and/or similar amalgams containing aromatic structures (e.g. quenched car-  
352 bonaceous composites (QCCs), Sakata et al. (1984)) have been incorporated into dust mixture  
353 SED models over the last two decades (Draine & Li 2001b, 2007a; Hony et al. 2001; Compiègne  
354 et al. 2011; Galliano et al. 2011; Jones et al. 2013, 2017).

355 Moving in the opposite direction, into the Rayleigh-Jeans regime of thermal dust emis-  
356 sion, multi-wavelength observations have opened up a new discipline: the disentagnlement of  
357 interstellar dust emission from non-dust emission components. Most notably, separating fluc-  
358 tuations in the cosmic microwave background (CMB) from the microwave extent of thermal  
359 dust emission. Those studying the Milky Way itself, from the far IR into microwave and radio  
360 frequencies, are now collaborating closely with those interested in the precise nature of the  
361 CMB.

### 362 1.3 Microwave foregrounds

363 Much of the motivation between recent galactic microwave emission research has little to do with  
364 galactic ISM astronomy itself. Rather, our galaxy presents an inconvenience to observational  
365 cosmology in that it 'contaminates' observations of the CMB. The avereage SED of the CMB  
366 is simple enough to model, with a  $2.755\ \text{K}$  blackbody function. This temperature however  
367 means that the peak occurs between several microwave foreground components, from interstellar

368 dust and gas, as displayed in Fig. 1.1. The difficulty of decomposing the microwave sky into  
 369 galactic ISM, extragalactic, and CMB components has brought the detailed decomposition of  
 370 the microwaveradio regime of ISM to the forefront of Planck Collaboration paper titles (Planck  
 371 Collaboration et al. 2011a, 2014a, 2016a). Without extragalactic research, there would be no  
 372 need for the word “foreground” in describing galactic microwave emission.

373 The ISM has intruded into cosmological studies perhaps most prominently with the first  
 374 claimed detection of B-mode polarization (Hanson et al. 2013; BICEP2 Collaboration et al.  
 375 2014; Flauger et al. 2014), and multiple response papers. The main consensus being that the  
 376 validation of CMB-related claims require a careful estimate of the contribution, in intensity and  
 377 polarization, from interstellar dust and the subsequent counterclaim that this detection arose  
 378 from galactic dust(Planck Collaboration et al. 2017; Sheehy & Slosar 2017). More recently AMI  
 379 Consortium et al. (2012) had noted a peculiar SunyaevZeldovich effect based galaxy cluster  
 380 detection, AMI-CL J0300+2613. Perrott et al. (2018) have since proposed that this may in  
 381 fact arise from high galactic latitude dust via “anomalous microwave emission” (AME).

### 382 1.3.1 Anomalous Microwave Emission

383 In our efforts to decompose and understand galactic microwave emission itself, there remains a  
 384 constant antagonist. Galactic foregrounds had been broken down into 3 dominant components:  
 385 free-free emission from ionized regions, synchrotron emission generated by electrons relativis-  
 386 tically by the Milky Way’s magnetic field, and the microwave extent of thermal dust emission  
 387 (Bennett et al. 2003a; Leach et al. 2008; Planck Collaboration et al. 2014c). Deviations from  
 388 this understanding began to appear in the early 1990s, with efforts by Kogut et al. (1996);  
 389 Leitch et al. (1997) to carefully investigate the CMB. They had found a component of the mi-  
 390 crowave sky which implied unlikely spectral indices for free-free or synchrotron emission. AME  
 391 generally takes the form of an ‘excess’ continuum emission source, having a peak somewhere  
 392 between 10 to 40 GHz (see Fig. 1.1). This excess defies predictions for known microwave emis-  
 393 sion mechanisms. AME still lacks a concrete physical explanation. Also, the term itself can  
 394 be a bit confusing, as the word “anomalous” tends to imply localized outlier. The AME is  
 395 shown to be more than an isolated anomaly, but an added component of microwave emission  
 396 appearing throughout the galaxy (de Oliveira-Costa et al. 1997; Bennett et al. 2003a; Dickinson  
 397 et al. 2013). Fig 1.2 shows two prominent AME regions,  $\rho$  Ophiuchus and the Persues Molec-

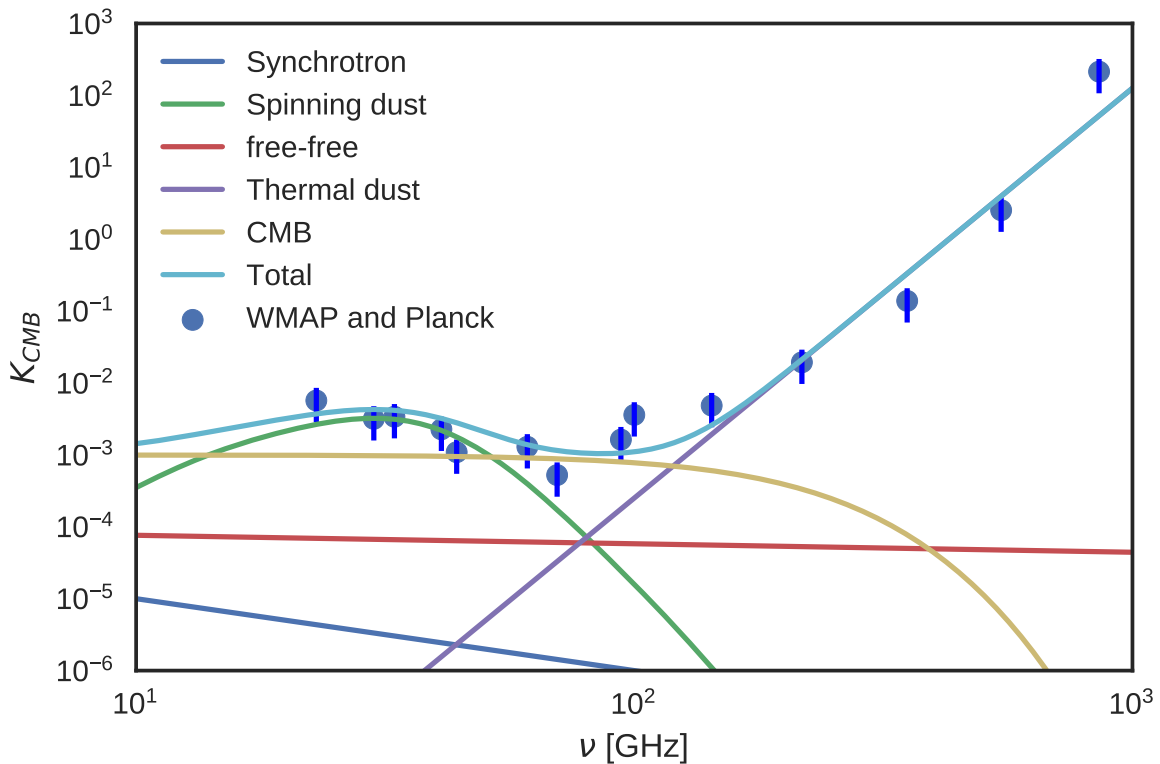


Figure 1.1: An example of a potential makueup of microwave emission components. Photometry points are extracted from the Planck and WMAP all-sky maps (Planck Collaboration et al. 2014b), for a part of the region well-known for prominant AME,  $\rho$  Ophiuchus (Planck Collaboration et al. 2011b). The AME curve is produced from a warm neutral medium spinning dust template (Ali-Haïmoud et al. 2009), with a frequency-shift applied to approximately fit the microwave data s in Planck Collaboration et al. (2016b)

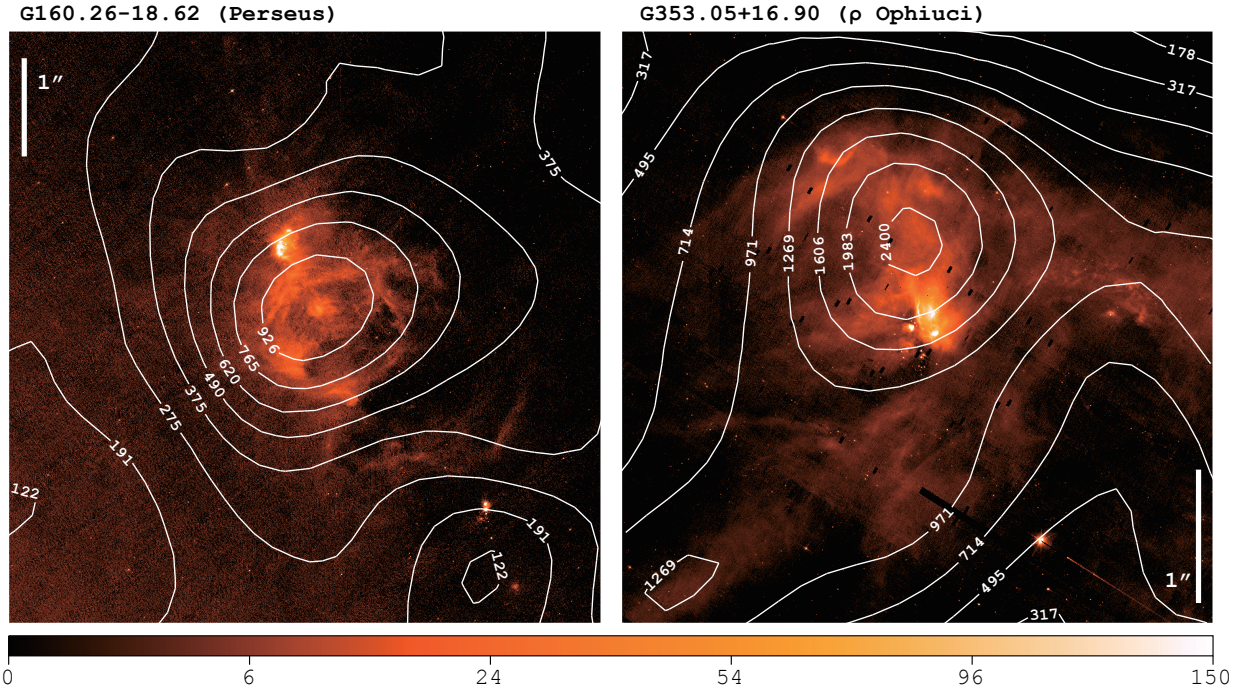


Figure 1.2: Two AME prominent regions investigated by Planck Collaboration et al. (2011b); Tibbs et al. (2011),  $\rho$  Ophiuchus and Perseus, as they appear in the PAH-feature-tracing AKARI/IRC  $9\mu\text{m}$  all-sky data at native resolution (Ishihara et al. 2010). White contours show AME at 1-degree resolution, extracted from the map by Planck Collaboration et al. (2016b). The IRC data shown here is of a much finer resolution than the AME data, at around  $10''$ , demonstrating the critical gap in resolvability of all-sky AME-tracing data itself vs. the IR dust tracers we hope to compare it to.

398 ular Cloud investigated by Tibbs et al. (2011); Planck Collaboration et al. (2011b), as they  
 399 appear in AKARI/IRC  $9\mu\text{m}$  all-sky map (Ishihara et al. 2010). In this section we will explain  
 400 that while there is indeed much mystery as to the exact mechanism(s) producing the AME,  
 401 what causes its spectral variations, and what might be its physical carrier(s) - it is by now,  
 402 perhaps less than anomalous. Following subsections will discuss the history of AME and the  
 403 produced physical explanations, as well comparisons between the AME and infrared emission  
 404 from interstellar dust.

#### 405 Correlation with dust

406 Since its first detection in early microwave observations, AME has been found to be a widespread  
 407 feature of the microwave Milky Way (see the review Dickinson et al. (2013), and an updated  
 408 state-of-play of AME research by Dickinson et al. (in prep). Kogut et al. (1996); de Oliveira-  
 409 Costa et al. (1997) showed that the AME correlates very well with infrared emission from

dust, via COBE/DIRBE and IRAS far-IR maps. Finkbeiner et al. (2002) reported the first detection of a “rising spectrum source at 8 to 10 GHz” in an observation targeting galactic ISM cloud. de Oliveira-Costa et al. (2002) further argued that this emission is in fact “ubiquitous”. The exact mechanism and carrier/s remain mysterious however. More recent works, employing observations by the Wilkinson Micrwave Anisotropy Probe (WMAP), Spitzer Space Telescope, the latest IR to microwave all-sky maps by Planck, and various ground based radio observations have strongly confirmed a relationship between interstellar dust emission and AME (Ysard & Verstraete 2010; Tibbs et al. 2011; Hensley et al. 2016). Exactly which physical mechanisms produces the AME however is still an open question, even if we assume a dusty AME origin. We equally puzzled as to the chemical composition and morphology of the carrier(s). We also lack an all-sky constraint on the emissivity of the AME spectrum at frequencies short of the WMAP cut-off, around 23 GHz. The typical peak frequency of AME, in those cases where it is constrained, does give us a clue.

### 1.3.2 Proposed explanations

From the observed spatial correlation between AME and dust emerged two prevailing hypotheses:

1) Electric dipole emission by spinning small dust grains, a mechanism proposed in Erickson (1957) and Hoyle & Wickramasinghe (1970), with further discussion in Ferrara & Dettmar (1994). Draine & Lazarian (1998b) give the earliest thorough theoretical prediction of a spinning dust spectrum. A decade later Ali-Haïmoud et al. (2009) contributed substantial updates, expanded modeling of grain excitation mechanisms and adoption of an updated grain size distribution by Weingartner & Draine (2001). Ysard & Verstraete (2010) introduced the first model of a spinning dust spectrum based on rotational emission from polycyclic aromatic hydrocarbons (PAHs), which are implicated due to their size. Draine & Lazarian (1998b), gives the expected rotational frequency of spinning dust oscillators  $\omega$ , as follows:

$$\frac{\omega_T}{2\pi} = \langle\nu^2\rangle^{1/2} \approx 5.60 \times 10^9 a_{-7}^{-5/2} \xi^{-1/2} T_2^{1/2} \text{ Hz}, \quad (1.3.1)$$

where  $T$  is the gas temperature,  $a$  is the grain size, and  $\xi$  represents the deviation from a spherical moment of inertia. For example, we can take a typical peak frequency of the AME

437 of  $\sim$ 20 GHz, a gas temperature of 100 K, roughly spherical grains, and a dipole moment on the  
 438 order of 1 debye, and get:

$$\frac{\omega_T}{2\pi} = 20 \text{ GHz} \left( \frac{T}{100K} \right)^{1/2} \left( \frac{\rho}{3gcm^{03}} \right)^{-1/2} \left( \frac{a}{5\text{\AA}} \right)^{-5/2} \quad (1.3.2)$$

439 implying an oscillator size of approximately 1 nm. Thus PAHs, as considered by Ysard &  
 440 Verstraete (2010), are a primary candidate spinning dust carrier, due to their expected size  
 441 range.

442 2) Magnetic dipole emission, caused by thermal fluctuations in grains with magnetic inclu-  
 443 sions, proposed by Draine & Lazarian (1999). More recently, modeled spectra for potential  
 444 candidate carriers have appeared in the literature: PAHs, grains with magnetic inclusions  
 445 (Draine & Hensley 2013; Ali-Haïmoud 2014; Hoang et al. 2016).

446 A third, but not widely accepted, possible explanation for AME is discussed in Jones (2009).  
 447 They have suggested that the emissivity of dust, in the spectral range related to AME, could  
 448 contain features caused by low temperature solid-state structural transitions.

#### 449 Spinning dust

450 Spinning dust need not be the only emission mechanism, a convention as arisen in AME obser-  
 451 vational works. The photometric signature of the AME is frequently interepreted via spinning  
 452 dust parameters (Ysard et al. 2011; Ali-Haimoud 2010). Archival all-sky AME data products  
 453 exclusively assume a spinning dust SED templates. Both WMAP and Planck used a base tem-  
 454 plate with 30 GHz peak frequency, and an assumed cold neutral medium evironment. Using  
 455 the “spdust” spinning dust SED model code to fit excess microwave foreground emission has  
 456 become analagous fitting a modified blackbody function to the far IR.

457 We explore the case that the AME signature arises from spinning dust emission. If the  
 458 AME is carried by spinning dust, the carrier should be small enough that it can be rotationally  
 459 excited to frequencies in the range of 10-40 GHz, and must have a permanent electric dipole.  
 460 Within contemporary dust SED models, only the polycyclic aromatic hydrocarbon family of  
 461 molecules (PAHs), or nanoscale amorphous carbon dust fit these criteria. Those PAHs which  
 462 have a permanent electric dipole (i.e. coranulene, but not symmetric molecules like coronene),  
 463 can emit rotationally. However the carrier need not be carbon-based. Indeed, Hensley & Draine  
 464 (2017) claim that AME can be explained without carbonaceous carriers, using only spinning

465 nanosilicates.

466 **Spinning PAHs?**

467 Assuming the rotational emission model of Draine & Lazarian (1998b), the AME signature  
468 (consistent with peaked, continuum emission having a peak between 15 and 50 GHz ) implies  
469 very small oscillators ( $\sim 1$  nm).

470 In any case, the PAH class of molecules are the only spinning dust candidate so far which  
471 show both:

- 472 1) Evidence of abundance in the ISM at IR wavelengths, and  
473 2) A predicted range of dipole moments (on order of 1 debye), to produce the observed AME  
474 signature (Draine & Lazarian 1998b; Lovas et al. 2005; Thorwirth et al. 2007).

475 However, it should be noted that although nanosilicates have not yet been detected in the  
476 ISM, Hensley & Draine (2017) propose that an upper bound on the abundance of nanosilicates  
477 by Li & Draine (2001) (based on IRTS observations by Onaka et al. (1996)), allow such small  
478 spinning grains to be composed primarily of silicates.

479 While neither nanosilicates nor any particular species of PAHs have been conclusively iden-  
480 tified in the ISM, there is far more empirical evidence for PAH-like dust than for nanosilicates.  
481 Mid-infrared features associated with PAH-like aromatic materials have been observed. In fact,  
482 “the PAH features” are ubiquitous in the ISM (Giard et al. 1994; Onaka et al. 1996; Onaka  
483 2000), such that the carriers must be abundant. Andrews et al. (2015) strongly argue for the  
484 existence of a dominant “grandPAH” class, containing 20 to 30 PAH species.

485 **1.3.3 Excitation factors**

486 In the spinning dust model, there are several possible excitation factors for spinning dust.  
487 For the grains to have rotational velocities high enough to create the observed AME, they  
488 must be subject to strong excitation mechanisms. The dominant factors that would be giving  
489 grains their spin, are broken down by Draine (2011) into basically two categories: 1) Collisional  
490 excitation. 2) Radiative excitation, the sum of which could lead to sufficient rotational velocities  
491 for sufficiently small grains. However the extent of excitation will depend on environmental  
492 conditions, i.e. there will be more frequent encounters with ions and atoms in denser regions  
493 (so long as the density is not high enough to coagulate the small grains), and more excitation

due to photon emission with increasing ISRF strength (Ali-Haïmoud et al. 2009; Ali-Haïmoud 2014). One of the strongest potential excitation mechanisms listed in Draine (2011) is that of negatively charged grains interacting with ions. Thus not only must we consider environmental factors, grain composition and size, but also the ionization state of the carriers. (For example, ionized vs. neutral PAHs.) The dependence of the observed AME on ISM density is modeled by Ali-Haimoud (2010).

### 1.3.4 AME vs. IR in the literature

The overall pattern among large-scale studies seems to show that all of the dust-tracing photometric bands correlate with the AME (and each other) to first-order. On an all-sky, pixel-by-pixel basis, at  $1^\circ$  angular resolution, Ysard et al. (2010) find that  $12 \mu\text{m}$  emission, via IRAS, correlates slightly more strongly with AME (via WMAP) than with  $100 \mu\text{m}$  emission. They also find that scaling the IR intensity by the interstellar radiation field strength (given as  $U$ , a measure of ISRF relative to that of the solar neighborhood) improves both correlations. They interpret this finding as evidence that AME is related to dust, and more closely related to the small stochastically emitting dust — predominantly PAHs — that is traced by  $12 \mu\text{m}$  emission. The improvement of the correlations after scaling by  $U$  is expected, as long as the  $12 \mu\text{m}$  or  $9 \mu\text{m}$  photometric bands are by stochastic emission from PAHs, in other words:

$$I_{12 \mu\text{m}} \propto U N_{PAH}, \quad (1.3.3)$$

where  $N_{PAH}$  is the column density of emitting PAHs (Onaka 2000). Thus it implies that  $I_{12 \mu\text{m}}/U$  is giving us a measure of the column density of spinning dust.

In a similar work however Hensley et al. (2016) report a lack of support for the spinning PAH hypothesis. Finding that fluctuations in the ratio of PAH-dominated  $12 \mu\text{m}$  emission (via WISE) to dust radiance,  $R$ , (via Planck) do not correlate with the ratio of AME intensity to  $R$ , they conclude that the AME is not likely to come from PAHs. In terms of emission intensity however, their findings are consistent with Ysard et al. (2010) in that  $I_{12 \mu\text{m}}$  correlates well with  $I_{AME}$ . Thus there remains an open question as to what the actual carrier of the AME is.

The story is no more clear when looking at the average properties of individual regions. Planck Collaboration et al. (2014d) find that among 22 high-confidence “AME regions” (galactic

521 clouds such as the  $\rho$  Ophiuchus cloud and the Perseus molecular cloud complex) AME vs.  $12\ \mu\text{m}$   
522 shows a marginally weaker correlation than AME vs.  $100\ \mu\text{m}$  (via IRAS). Tibbs et al. (2011)  
523 examined the AME-prominent Perseus Molecular Cloud complex, finding that while there is  
524 no clear evidence of a PAH-AME correlation, they do find a slight correlation between AME  
525 and  $U$ .

## 526 1.4 Scope of this Dissertation

527 We attempt to add to the understanding of AME and the possibility of spinning dust emission.  
528 With ample multiwavelength data now available, and a new PAH-focused all-sky survey in  
529 preparation by AKARI, we further test the PAH hypothesis, and assess how the IR to AME  
530 correlation changes as a function of wavelength.

### 531 1.4.1 An application of all-sky archival data

532 This is an astrophysical data archive based work. The primary goal is to highlight a particular  
533 application of multiwavelength (mid-IR to radio), cross-archive all-sky data analysis. We de-  
534 scribe the interrelatedness between mid to far IR dust emission and possible microwave emission  
535 from dust. This is accomplished through an investigation of photometric all sky maps mainly  
536 from AKARI, IRAS, and Planck.

### 537 1.4.2 Testing the spinning PAH hypothesis

538 For the present work, we consider the spinning PAH hypothesis to have the highest degree of  
539 testability, due to the well-established presence of aromatic emisison features in the ISM. We  
540 do not argue against the physical plausibility of nanosilicates to produce the AME. Indeed,  
541 there is no argument to date that these potential physicalities are mutally exclusive, as long as  
542 both potential carriers are sufficiently abundant. Nor does spinning dust emission theoretically  
543 exclude magnetic dipole emission or microwave thermal dust emissivity fluctuations.

### 544 1.4.3 Limitations

545 We do not explore the modeling of microwave dust emission itself, rather we refer to estimates  
546 of spinning dust emisison provided in the literature (Planck Collaboration et al. 2014c; Bennett

et al. 2003a) in the form of archival data and parameter maps. We consider this problem first on an all-sky basis, not focusing on any pre-selected object of the sky — in order to assess if there any general pattern between the IR and the AME, beyond the AME-dust correlation already described above. We then focus on a region highlighted by the Planck Collaboration as being especially worthy of further investigation (Planck Collaboration et al. 2016b), and has a resolvable topology even at  $1^\circ$  resolution. Essentially all of the analyses and conclusions presented in this work apply to an angular scale of approximately  $1^\circ$ , and only for the given component separation methods (Solar system, galactic, extragalactic) used by each of the data providers.

#### 1.4.4 Code availability

Because this work is intended to contribute working examples for future students, in addition to making a research contribution, this thesis is accompanied by a `github` repository (to be made available upon acceptance of the thesis).<sup>1</sup> Most of analyses code are available in that repository, in the form of Jupyter notebooks. Most of the figures, and code used to generate them, are also included. The dust SED fitting code is not part of that repository, but is described in Galliano et al. (in prep.)

---

<sup>1</sup> Available at: <https://github.com/aaroncnb/CosmicDust>.

<sup>563</sup> **Chapter 2**

<sup>564</sup> **Data Sources**

<sup>565</sup> **2.1 A collection of skies**

<sup>566</sup> This work relies completely on all-sky surveys. All of the maps utilized are photometric-band  
<sup>567</sup> infrared maps, except for the AME data, which is an all-sky component separation analysis  
<sup>568</sup> product, from the Planck Collaboration's efforts to separate galactic foregrounds from the CMB. Table 2.1 summarizes the observational data used in this thesis. In total, we employ

Table 2.1: Observational data sources used in this article

Instrument	Central Wavelength	FWHM	Cali	Reference
AKARI/IRC	9 $\mu\text{m}$	$\sim 10''$	<10%	<sup>1</sup>
AKARI/IRC	18 $\mu\text{m}$	$\sim 10''$	<10%	"
AKARI/FIS	65 $\mu\text{m}$	63''	<10%	<sup>2</sup>
AKARI/FIS	90 $\mu\text{m}$	78''	<10%	"
AKARI/FIS	140 $\mu\text{m}$	88''	<10%	"
AKARI/FIS	160 $\mu\text{m}$	88''	<10%	"
IRAS/IRIS	12 $\mu\text{m}$	4.0'	<5.1%	<sup>3</sup>
IRAS/IRIS	25 $\mu\text{m}$	4.0'	<15.1%	"
IRAS/IRIS	60 $\mu\text{m}$	4.2'	<10.4%	"
IRAS/IRIS	100 $\mu\text{m}$	4.5'	<13.5%	"
Planck/HFI	345 $\mu\text{m}$	4.7'		<sup>4</sup>
Planck/HFI	550 $\mu\text{m}$	4.3'		"

<sup>569</sup> all-sky maps from 12 photometric bands, spanning the wavelength range of 6.9  $\mu\text{m}$  to 550  $\mu\text{m}$   
<sup>570</sup> as shown in Fig. 2.1. The following sections give the details of the observational data from each

---

<sup>1</sup>Ishihara et al. (2010)

<sup>2</sup>Doi et al. (2015); Takita et al. (2015)

<sup>3</sup>Miville-Deschénes & Lagache (2005)

<sup>4</sup>Planck Collaboration et al. (2014b)

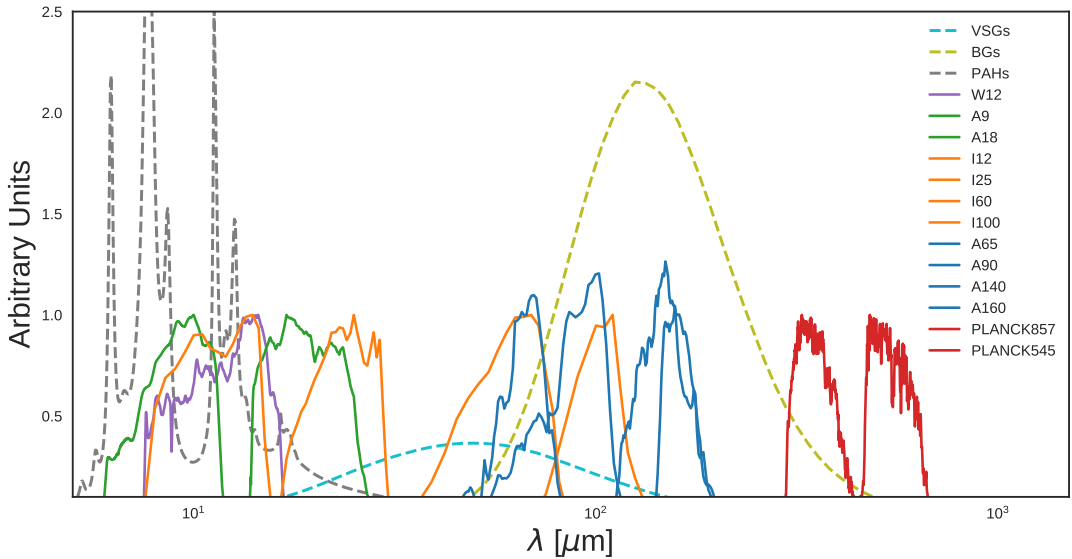


Figure 2.1: Relative spectral response curves of the bands used in this study. Expected dust emission components, assuming the dust SED model by (Compiègne et al. 2011) are also shown. The components are summarized as emission from big grains (BGs, dashed yellow line), emission from very small grains (VSGs, dashed blue line), and emission from PAHs (dashed grey line).

instrument as well as of the parameter maps provided in Planck Collaboration et al. (2016b).<sup>5</sup>  
 572 From this point in the thesis, we will mostly use abbreviations to refer to the different bands,  
 573 as follows: 'A' indicates AKARI; 'D', DIRBE; 'I', IRAS, and 'P' Planck. The number after  
 574 each letter indicates the band central nominal wavelength in microns (or frequency in GHz, in  
 575 the case of the Planck bands.)

Table 2.2: Ancillary data

Product	Relevant Freq./Wavelen	FWHM	Reference/URL
$H\alpha$	658.5 nm	36'	6
$N(H)$	21 cm	36'	7
PC $R$ (PR1)	353 GHz	5'	8
PC $\tau_{353}$ (PR1)	353 GHz	5'	"
Haslam MHz	408 MHz	56'	9
PC Synchrotron (PR2)	408 MHz	60'	10
PC $AME_{var}$ (PR2)	22.8 GHz	60'	11
PC $AME_{fix}$ (PR2)	41.0 GHz	60'	"
PC free-free (PR2)	N/A	60'	12

<sup>5</sup>Planck bands are named according to their central frequency, not wavelength.

## 576 2.2 AKARI

577 The AKARI infrared space telescope revealed an entire sky of infrared light, from the mid to  
578 far infrared, via two instruments (Murakami et al. 2007) the Infrared Camera (IRC)(Onaka  
579 et al. 2007) and the Far Infrared Surveyor (FIS) (Kawada et al. 2007b). In this section we will  
580 discuss the all-sky surveys produced by these two instruments.

### 581 2.2.1 AKARI/Infrared Camera (IRC)

582 IRC provided us with both spectroscopic and photometric data from the near to mid-infrared.  
583 In this work, we utilize the all-sky maps centered at 9 and 18  $\mu\text{m}$ , created during by the IRC's  
584 fast-scanning mode. We utilize the most recent version of the IRC data (Ishihara, et al., in  
585 prep.) This version has had an updated model of the Zodiacaal light, fitted and subtracted. The  
586 details of the improved Zodi-model, which offers an improvement over that used for the IRAS  
587 all-sky maps, are given in Kondo et al. (2016).

### 588 PAH feature coverage

589 The A9 all-sky map demonstrates the abundance of the PAH bands carrier in the Milky Way  
590 (Ishihara et al. 2010). Figure 2.2 shows the coverage of the PAH features (from both ionized  
591 and neutral PAH components), as they are theoretically determined in Compiègne et al. (2011).  
592 The A9 band uniquely covers major ionized PAH features at 6.2 and 7.7  $\mu\text{m}$ ; as well as neutral  
593 PAH features at 8.6 and 11.2  $\mu\text{m}$  across the entire sky (Onaka et al. 2007). The I12 band covers

---

<sup>6</sup>Finkbeiner (2003):

[https://lambda.gsfc.nasa.gov/product/foreground/halpha\\_map.cfm](https://lambda.gsfc.nasa.gov/product/foreground/halpha_map.cfm)

<sup>7</sup>Kalberla, P. M. W. et al. (2005):

[https://lambda.gsfc.nasa.gov/product/foreground/fg\\_LAB\\_HI\\_Survey\\_get.cfm](https://lambda.gsfc.nasa.gov/product/foreground/fg_LAB_HI_Survey_get.cfm)

<sup>8</sup>):  
[http://irsa.ipac.caltech.edu/data/Planck/release\\_1/all-sky-maps/previews/HFI\\_CompMap\\_ThermalDustModel\\_2048\\_R1.20/index.html](http://irsa.ipac.caltech.edu/data/Planck/release_1/all-sky-maps/previews/HFI_CompMap_ThermalDustModel_2048_R1.20/index.html)

<sup>9</sup>Haslam et al. (1982):

<sup>10</sup>Planck Collaboration et al. (2016b):

[http://irsa.ipac.caltech.edu/data/Planck/release\\_2/all-sky-maps/previews/COM\\_CompMap\\_Synchrotron-commander\\_0256\\_R2.00/index.html](http://irsa.ipac.caltech.edu/data/Planck/release_2/all-sky-maps/previews/COM_CompMap_Synchrotron-commander_0256_R2.00/index.html)

<sup>11</sup>[http://irsa.ipac.caltech.edu/data/Planck/release\\_2/all-sky-maps/previews/COM\\_CompMap\\_AME-commander\\_0256\\_R2.00/index.html](http://irsa.ipac.caltech.edu/data/Planck/release_2/all-sky-maps/previews/COM_CompMap_AME-commander_0256_R2.00/index.html)

<sup>12</sup>[http://irsa.ipac.caltech.edu/data/Planck/release\\_2/all-sky-maps/previews/COM\\_CompMap\\_freefree-commander\\_0256\\_R2.00/index.html](http://irsa.ipac.caltech.edu/data/Planck/release_2/all-sky-maps/previews/COM_CompMap_freefree-commander_0256_R2.00/index.html)

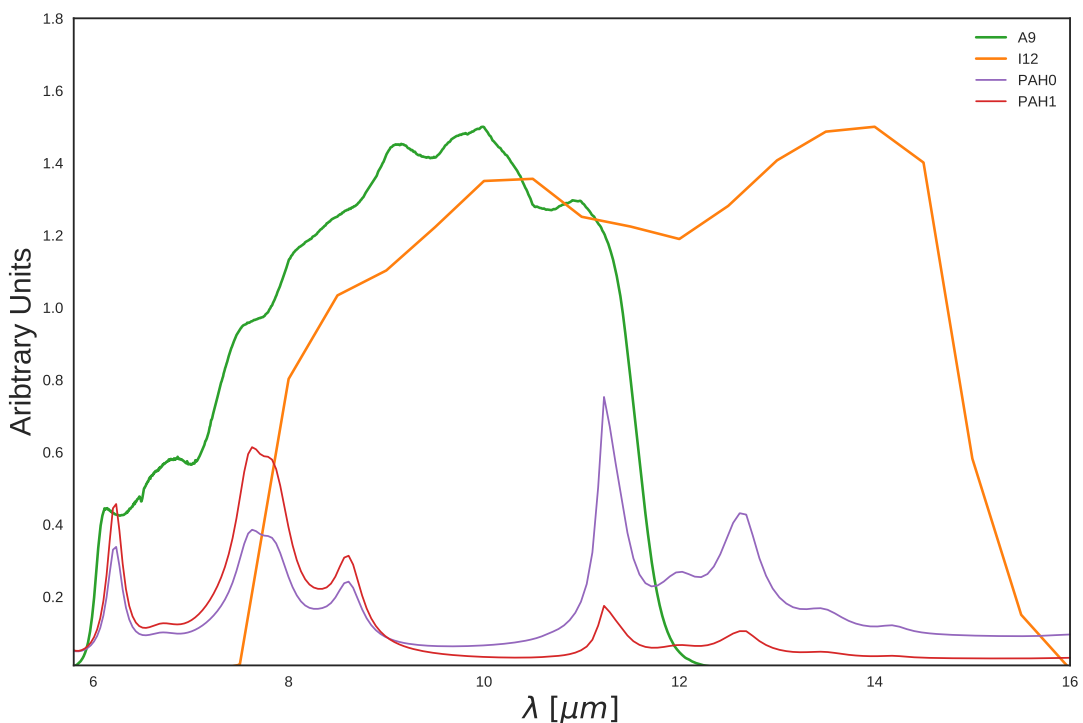


Figure 2.2: The I12 (orange) and A9 (green) filters coverage of modeled ionized (PAH1, red) and neutral (PAH0, purple) components of PAH features by Compiègne et al. (2011). The difference in the PAH feature coverage mainly comes from the  $6.2 \mu m$  and the  $7.7 \mu m$  feature.

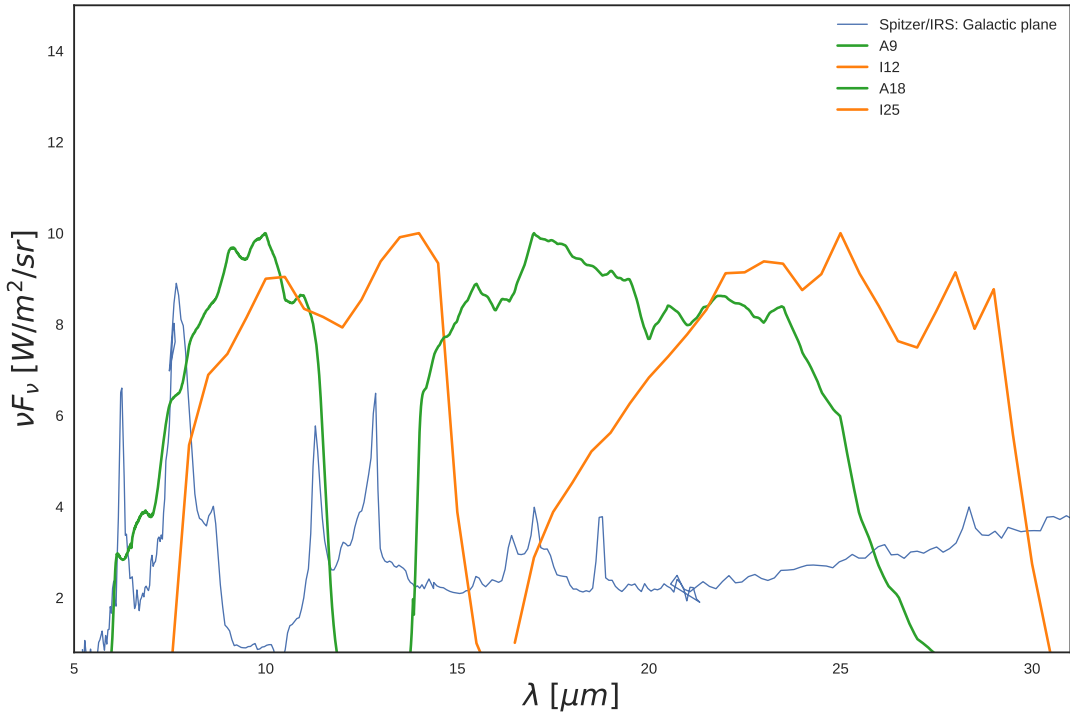


Figure 2.3: Coverage of MIR wavelengths by the filters used in this work. An Spitzer/IRS spectrum (see AOT4119040) of the galactic plane (thin blue line) demonstrates how IRC and IRAS photometric bands trace these features on an all-sky basis (Ishihara et al. 2007). Strong PAH features overlap with the A9 and I12, while the A18 and I25 micron bands only trace much weaker features.

594 the 11.2 and 8.6  $\mu\text{m}$  features, and the similarly-shaped W12 band covers primarily the 11.2  $\mu\text{m}$   
 595 feature but do not cover the 7.7  $\mu\text{m}$  completely. According to the distribution of PAH features  
 596 across the response filters in Fig. 2.2, and referring back to the various dust components in  
 597 Fig. 2.1 it is also expected that the A9 band is most dominated by PAH emission even with  
 598 increasing  $U$ . This may seem counter-intuitive, since, as described in Ch. 1, the PAH spectral  
 599 shape does not show a temperature variation. However as  $T$  increases, the MIR extent of  
 600 thermal dust emission and emission from VSGs encroach on I12 and WI2 sooner than A9,  
 601 diluting emission from PAHs. In some ionized regions, I12 may also include non-significant  
 602 contributions from the [NeII] line at 12.8  $\mu\text{m}$ . Figure 2.3 demonstrates an example observational  
 603 galactic cirrus spectrum in the MIR, from Spitzer Infrared Spectrograph (IRS) (Werner et al.  
 604 2004) data, along with filters for all of the MIR bands used in this study. It indicates that the  
 605 other MIR bands, A18 and I25, do cover strong PAH features and are expected to be dominated  
 606 rather by emission from very small grains (VSGs), as was indicated in Fig. 2.1.

607 To help demonstrate how the relative contribution from PAHs will change for each band,

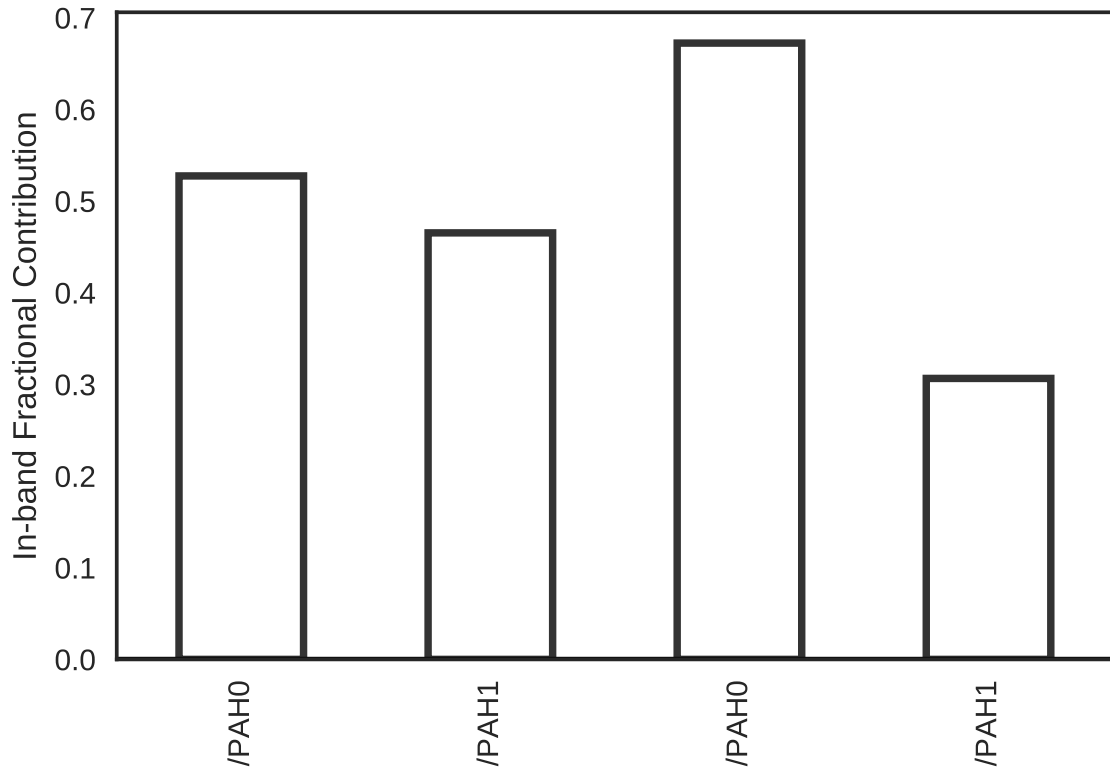


Figure 2.4: In-band contributions from charged (PAH1) neutral (PAH0) PAHs, to the emission detected by the I12 and A9 filters. These assume a model galactic cirrus spectrum simulated with the SED template of Compiègne et al. (2011).

for different ISRF strengths, Fig. 2.4 gives just such a calculation. These contributions remain relatively constant out to a  $U$  of about 100, with the contribution from warm dust becoming a larger factor for the I12 and W12 bands. Thus, according to the DL01 template, A9 should have the highest contribution from PAHs out to extreme radiation fields. At least to the extent with which PAHs can endure harsh UV radiation, as PAHs are expected to evaporate in strong enough radiation fields (Allain et al. 1996a,b; Bocchio et al. 2012; Pilleri et al. 2012; Pavlyuchenkov et al. 2013).

### PAH ionization

Figure 2.2 indicates that expected emission from ionized PAHs may preferentially contribute to the A9 band, even though both I12 and A9 cover ionized and neutral features. A PAH SED model calculation, using the Compiègne et al. (2011) SED template, supports that for Galactic cirrus ISM conditions, emission detected by the A9 band would have a higher contribution from charged PAHs than the I12 band. This is demonstrated in Fig. 2.4. To be clear, both bands are sensitive to both charged and neutral PAHs, however the relative contribution from charged

Figure 2.5: Ionization fraction of PAHs vs. band ratios of I12, I25, to A9, for two ISRF strengths: Top:  $U = 1$ , Bottom:  $U = 10$ . These ratios are determined by assuming the SED template of Compiègne et al. (2011)

PAHs is expected to be higher for A9. Thus we might expect that the ratio of intensities in this two bands, for a given line of sight (towards which PAHs are not destroyed), could trace the fraction of charged PAHs. Estimating the extent of this effect, Fig. 2.5 gives the results of a calculation of I12/A9 and I25/A9 band ratios for two ISRF strengths. This calculation is again based on Compiègne et al. (2011). It suggests that at least for  $U < \sim 10$ , the fraction of charged PAHs may be estimated as a function of the I12/A9 ratio.

Examining how this might look in the data themselves, Fig. 2.6 and Fig. 2.7 show the R(A9:I12) and R(A9:I25) ratio maps, demonstrating the relative variations in these MIR bands across the sky—or at least the portions of the sky where S/N is sufficient. While from visual inspection the various MIR intensity all-sky maps appear to essentially trace the same structures of the galaxy, the ratio maps reveal that there are indeed differences to be explored. In regions where noise is dominant, ascertaining the ionization fraction will be quite difficult. This can be easily seen upon visual inspection of the ratio maps, in that there is a clear deliniation between brighter emission towards lower galactic latitudes, and the high latitude sky where the ratio shows very little discernible structure (except for the Zodi-residual patterns which differ

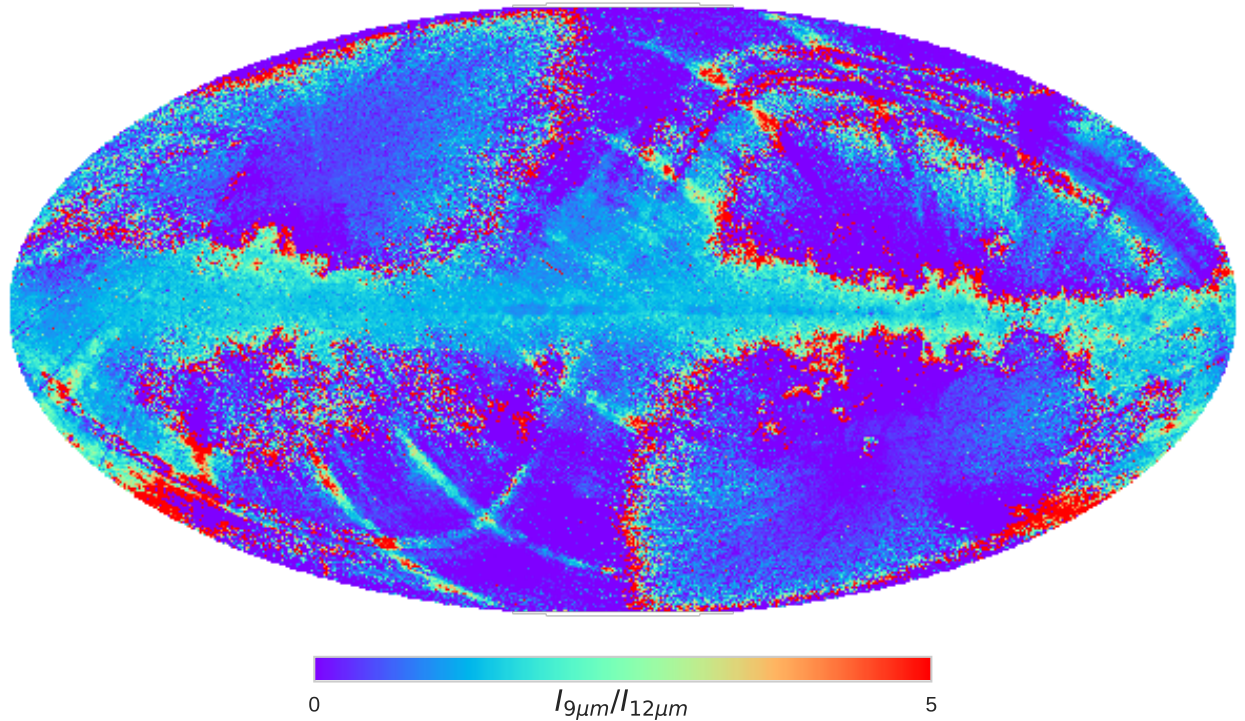


Figure 2.6: AKARI/IRC 9  $\mu\text{m}$  to IRAS 12  $\mu\text{m}$  intensity ratio.

between IRC and IRAS.) Thus there may a large portion of the sky where the S/N may be high enough to allow us to trace the PAH ionization fraction. This possibility is explored in Ch. 3, in looking at the PAH distribution within  $\lambda$  Orionis.

### 2.2.2 The AKARI Far Infrared Surveyor (FIS)

FIS gives us photometric data around the peak of the typical thermal dust SED. FIS was equipped with four wavebands: two narrow bands centered at 65  $\mu\text{m}$  and at 160  $\mu\text{m}$ , and two wide bands at 90  $\mu\text{m}$  and at 140  $\mu\text{m}$ . An all-sky survey was carried out at each band (Kawada et al. 2007a), and the processed maps have been publicly released (Doi et al. 2015).

### 2.2.3 Planck Observatory High Frequency Instrument (HFI)

The HFI all-sky maps, spanning 100 to 857 GHz (Planck Collaboration et al. 2014b) help constrain the far IR dust emissivity. This study utilizes the 857 GHz (345  $\mu\text{m}$ ) and 545 GHz (550  $\mu\text{m}$ ) bands.

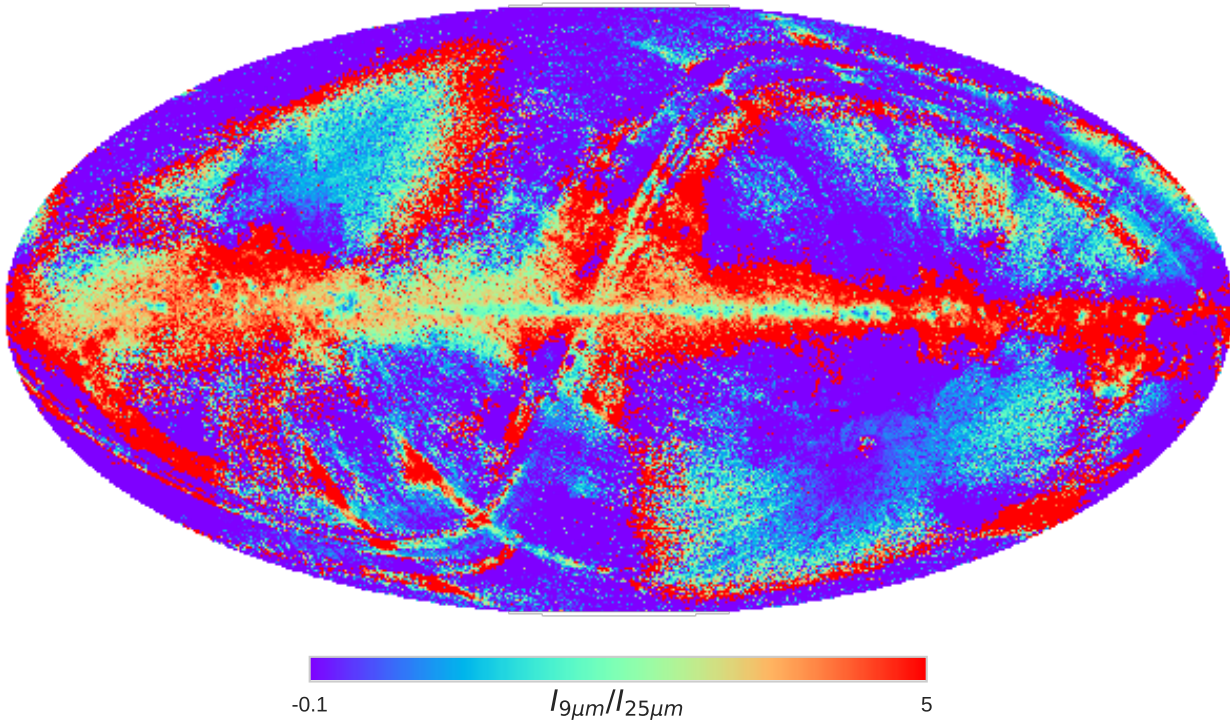


Figure 2.7: AKARI/IRC 9  $\mu\text{m}$  to IRAS 25  $\mu\text{m}$  intensity ratio.

## <sup>649</sup> 2.3 Infrared Astronomical Satellite (IRAS)

<sup>650</sup> Data from the IRAS (Neugebauer et al. 1984) all-sky surveys are used to supplement the  
<sup>651</sup> similarly-centered AKARI photometric bands. The IRAS 12  $\mu\text{m}$  band is similar to the IRC  
<sup>652</sup> 9  $\mu\text{m}$  band in terms of the sky coverage, central wavelength, and especially in that both surveys  
<sup>653</sup> are heavily dominated by zodiacal light. We use the Improved Reprocessing of the IRAS Surveys  
<sup>654</sup> (IRIS) (Miville-Deschénes & Lagache 2005), which have undergone a zodiacal-light removal.  
<sup>655</sup> The zodiacal light model, however differs between the two bands. The IRAS zodi-subtraction  
<sup>656</sup> is primarily based on the Kelsall et al. (1998) model, while IRC employs a modified version of  
<sup>657</sup> this model (Kondo et al. 2016). Although WISE provides higher resolution than IRAS, we do  
<sup>658</sup> not utilize the WISE data because we found the WISE all-sky 12  $\mu\text{m}$  product to essentially  
<sup>659</sup> trace the Planck HFI 857 GHz map, at 1° angular resolution. Hensley et al. (2016) had noted  
<sup>660</sup> that this scaling of the WISE map may artificially suppress actual PAH-related variations at  
<sup>661</sup> low resolution. Moreover, since we are conducting our analysis at 1° resolution in order to  
<sup>662</sup> match the AME data, the higher resolution offered by WISE is not a significant advantage.

---

## 663 2.4 Planck COMMANDER Parameter Maps

664 We utilize the COMMANDER-Ruler astrophysical component separation maps (Planck Col-  
 665 laboration et al. 2014c), from the Planck Collaboration's Public Data Release 2 (hereafter,  
 666 PR2)(Planck Collaboration et al. 2016a). These contain estimates of known microwave fore-  
 667 ground components (free-free, synchrotron, thermal dust emission contributions to the Planck  
 668 photometric bands. Fig. 2.8 demonstrates the correlatedness of these component maps, taken  
 669 as provided in the PR2 archive. Without considering noise levels or variations of scale, we  
 670 see evidence these major components are correlated with one another. In the case of free-free  
 671 emission, von Hausegger & Liu (2015) found that by taking S/N ratios into account, the corre-  
 672 lation between COMMANDER free-free and AME components turns negative. More generally  
 673 they suggest that the intercorrelations between these products varies with scale. We will first  
 674 describe the 'non-AME' components, so as to not give any indication that their estimation is  
 675 trivial.

### 676 2.4.1 Synchrotron

677 While the Planck observations themselves do limit our resolution when assessing the AME - it  
 678 is the primary constraint on synchrotron emission, 408 MHz map by Haslam et al. (1982) that is  
 679 the major resolution limiting factor. While an impressive early effort to reveal the low-frequency  
 680 sky, (Haslam et al. 1982) is limited to an approximately  $1^\circ$  resolution. The map also contains  
 681 many artifacts. For the time being however, it is still the most synchrotron-dominated all-  
 682 sky map available, and for this reason PC15X included it in their COMMANDER component  
 683 separation. Enhanced synchrotron mapping efforts are currently in progress by the 'The final  
 684 synchrotron product produced by COMMANDER (hereafter, PCSync) highly resembles the  
 685 Haslam et al. (1982) map, however it is also demonstrated PCSync does not fully capture the  
 686 synchrotron signal. This can be visualized by inspecting the PCAME:PCdust ratio map (see  
 687 Fig. 2.13), which Hensley et al. (2016) describe as containing synchrotron emission patterns at  
 688 high latitudes.

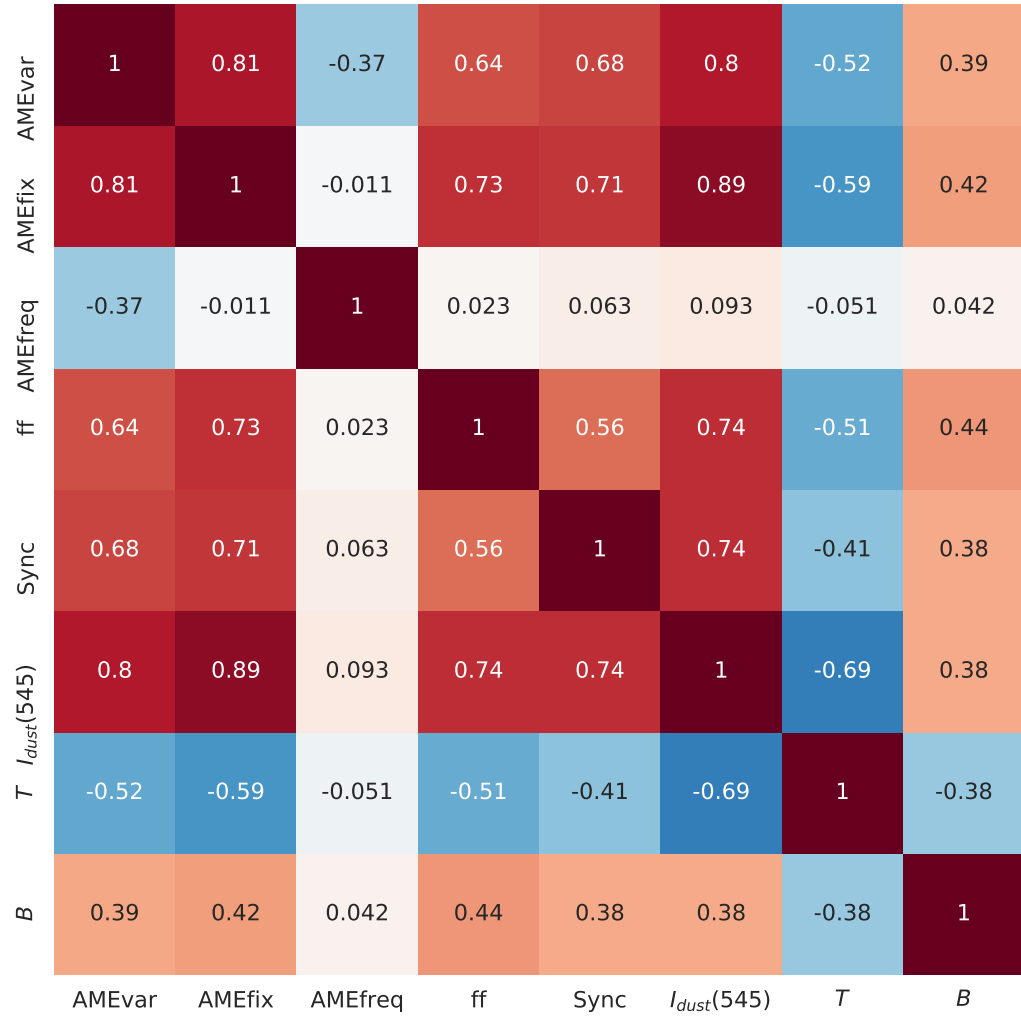


Figure 2.8:  $r_s$  cross correlation matrix of the PCCS maps: temperature  $T$ , emissivity index  $\beta$ , and amplitude at 545 GHz  $I_{dust}(545)$  of thermal dust; intensity of free-free emission  $ff$  at ; intensity of synchrotron emisison at 4 MHz  $Sync$ ; intensity of the AME var. freq. component AME at 22.8 GHz.

---

### 689 2.4.2 Free-free emission

690 Unlike the PCSync component, the fitting of the Planck COMMANDER free-free component  
 691 map (hereafter, PCff) does not employ any free-free dominated emisison map, even though an  
 692 earlier Planck AME paper (Planck Collaboration et al. 2014d) had employed the  $H\alpha$  map by  
 693 Finkbeiner (2003). Uncertainties in this map arise from uncertainties in the gas temperature,  
 694 and the Gaunt factor. This emission source is the dominant source of confusion with AME,  
 695 especially for HII regions (Planck Collaboration et al. 2014d,c; Paladini et al. 2015).

### 696 2.4.3 Thermal dust emission

697 “Thermal dust emission” in the COMMANDER context refers to dust emission in the Rayleigh  
 698 Jeans-regime, as the COMMANDER fitting includes neither photometric constraints on the  
 699 thermal emission peak, nor on Wiens-regime emission from small grains. This component es-  
 700 sentially involves the fitting of a modified blackbody curve (Eq. 1.2.1.) to the Planck Photome-  
 701 try. This approach however results in an apparent anti-correlation between  $\beta$  and  $T$  (Fig. 2.8).  
 702 Whether or not this anti-correltion is genuine is still unsettled in the literature (Galliano et al.  
 703 2011; Juvela & Ysard 2012). In any case, we do not utilize the  $\beta$  and  $T$ , only the dust intensity  
 704 at 545 GHz ( $I_d$ ) parameter map.

### 705 2.4.4 AME data

706 The COMMANDER map release also provides an “AME component map”, which presumes  
 707 that AME originates from spinning dust. While acknowledging that such a decomposition  
 708 lacks a strong physical interpretation, Planck Collaboration et al. (2016b) break the AME  
 709 into two components: a spatially varying peak frequency component,  $AME_{var}$ , and a spatially  
 710 constant peak frequency component,  $AME_{fix}$ . As seen in Fig. 2.9, virtually all of the fitted  
 711 peak frequencies for  $AME_{var}$  are beyond the reach of WMAP and Planck. Only the fitted  
 712 global frequency, 33.5 GHz for the spatially constant component, is covered. However they  
 713 note that the combined components, per pixel, would have an average peak at least within  
 714 the WMAP coverage range. In general,  $AME_{var}$  is the dominant component, accounting for  
 715 approximately 90% of the total fitted AME intensity between 20 and 40 GHz, indicated by  
 716 the full-sky histograms in Fig. 2.10. As they are provided in PR2, the intensities are in fact

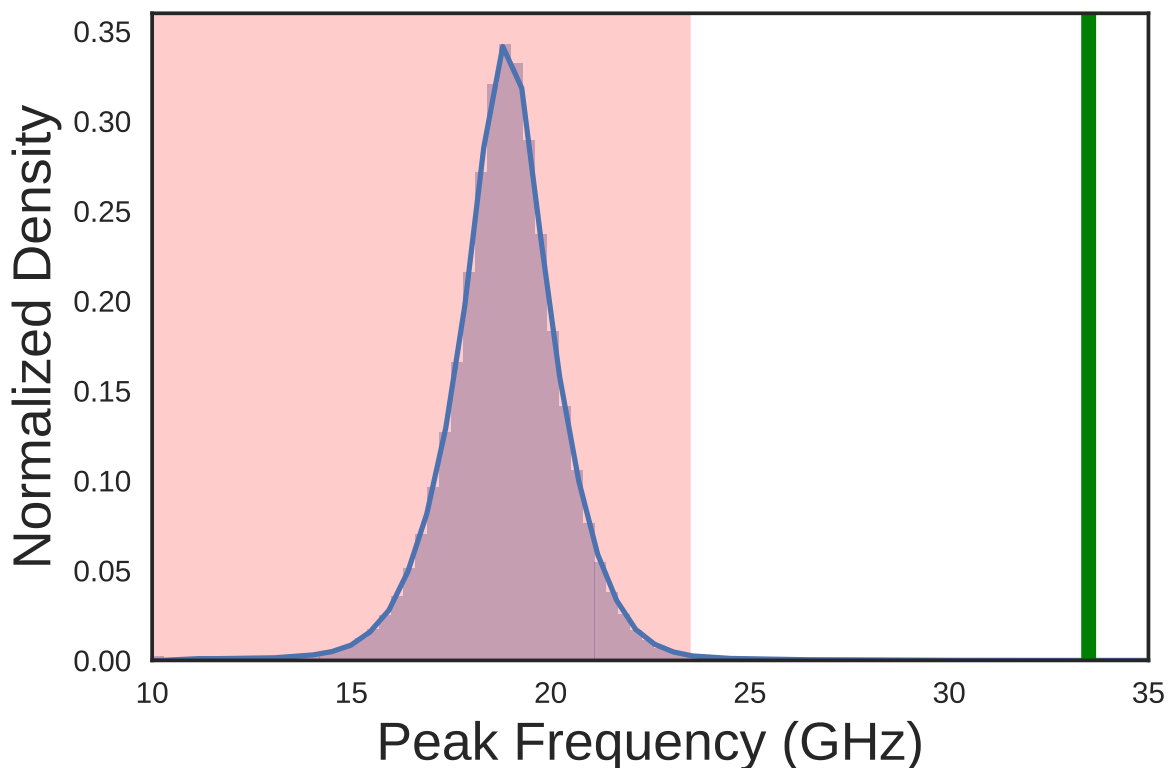


Figure 2.9: The peak frequencies of the varying component  $AME_{var}$ . The pink shaded region indicates frequencies not covered by either WMAP or Planck. The green line at 33.5 GHz indicates the peak frequency of  $AME_{fix}$ .

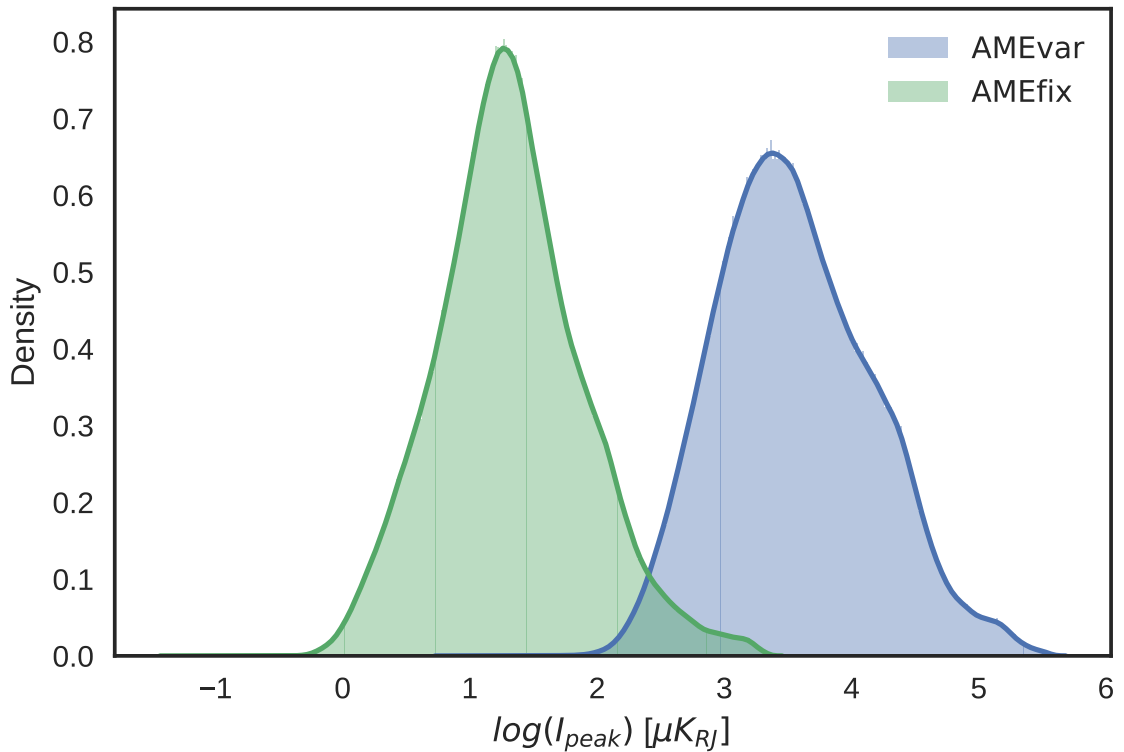


Figure 2.10: Histograms of the peak intensity AME maps calculated from the original COMMANDER-AME reference frequency maps. The dominant component,  $\text{AME}_{\text{var}}$  is indicated in blue, for all pixels in the map, with their spinning dust intensities evaluated their peak frequencies (see Fig. 2.9.)  $\text{AME}_{\text{fix}}$  gives the peak intensity of the spatially-constant frequency component, indicating it is essentially always the weaker component.

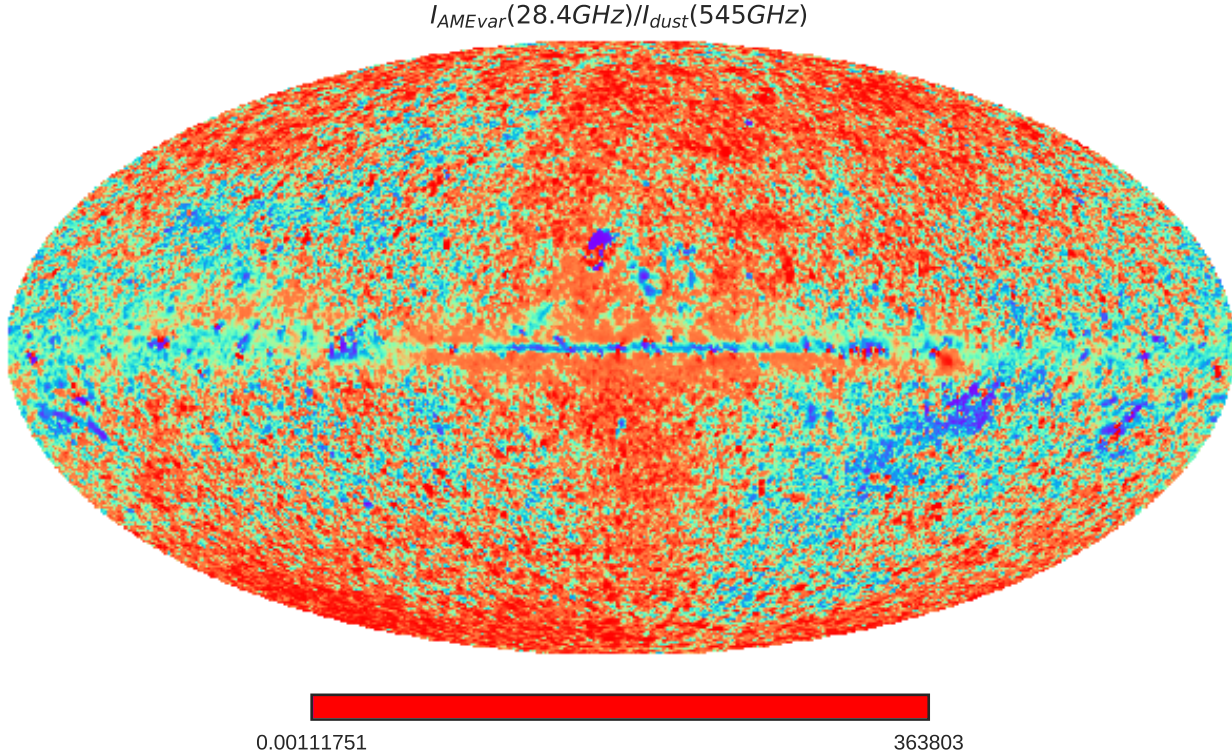


Figure 2.11: All-sky map of the peak frequencies of the varying component  $AME_{var}$ , corresponding to Fig. 2.9. Virtually all of the purple regions of the map correspond to pixels flagged for point sources in the LFI data. There are very few notable structures in the frequency map overall, other than the galactic plane itself,  $\rho$  Ophiuchus, and Perseus.

717 the fitted spinning dust profiles for each pixel, evaluated at reference frequencies: 22.8 GHz for  
 718  $AME_{var}$ , 41 GHz for  $AME_{fix}$  (for convenient comparison to the WMAP total intensity maps at  
 719 those frequencies). Fig. 2.10 in fact indicates our own re-evaluation of the fitted spinning dust  
 720 SEDs at their peak frequencies, as the reference frequencies do not have any special physical  
 721 relevance. This conversion does not have a significant effect on the results in the chapters to  
 722 follow, except in the case of some outlying pixels with very low peak frequencies, easily seen in  
 723 the map of the fitted frequencies in Fig. 2.11. However on comparison to point source masks  
 724 by Planck, we find that these outliers correspond to intensity outliers in the LFI 30 GHz map.  
 725 This is not readily apparent when viewing the  $AME_{var}$ , evaluated at 22.8 GHz, as it is provided  
 726 in Planck Collaboration et al. (2016b).

### 727 Spinning dust fitting

728 The actual spinning dust SED which is fitted to the Planck data by is indicated by Fig. 2.12,  
 729 which we have reproduced from the original template provided in Ali-Haïmoud et al. (2009).  
 730 PC15X fit the AME by applying a frequency shift and intensity shift parameter to this template.

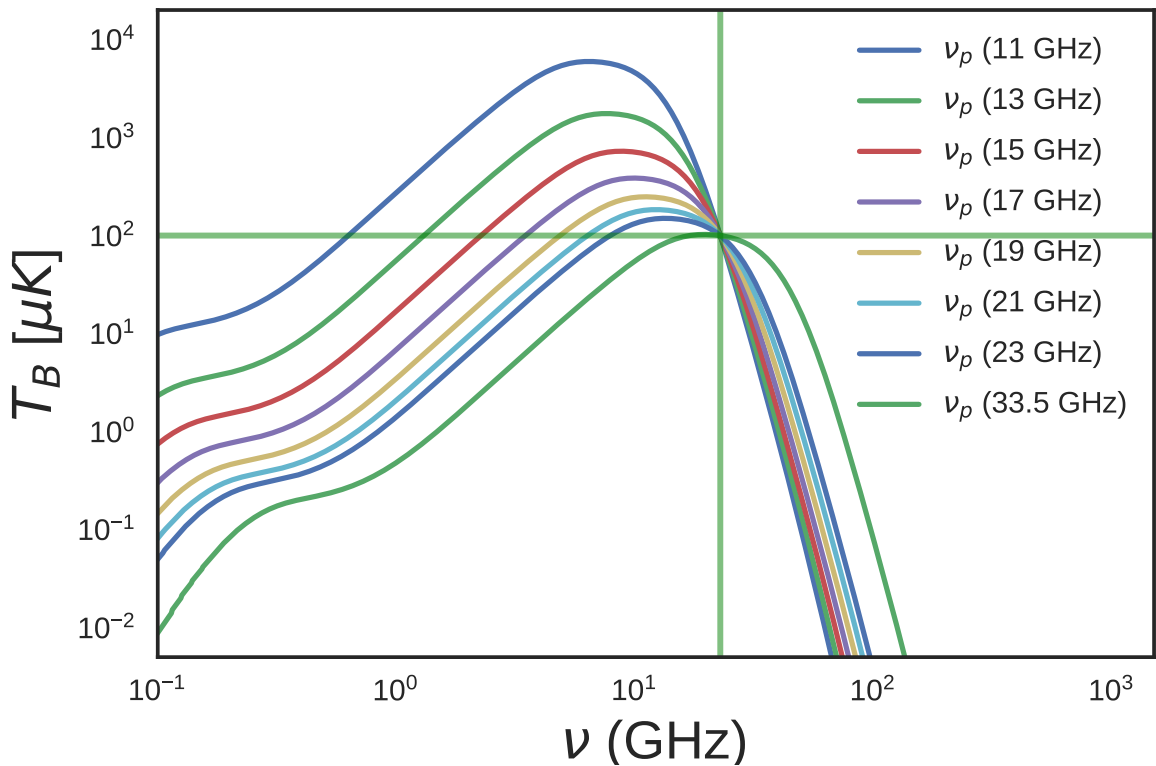


Figure 2.12: Spdust template spinning dust profiles fitted by PC15X when calculating  $AME_{var}$ . The reference frequency, 22.8 GHz is indicated by the vertical green line. Each template has the same  $AME_{var}$  amplitude of  $100 \mu\text{K}$ , indicated by the horizontal green line, plotted to highlight the potential deviation between  $AME_{var}$  and the actual peak intensity.

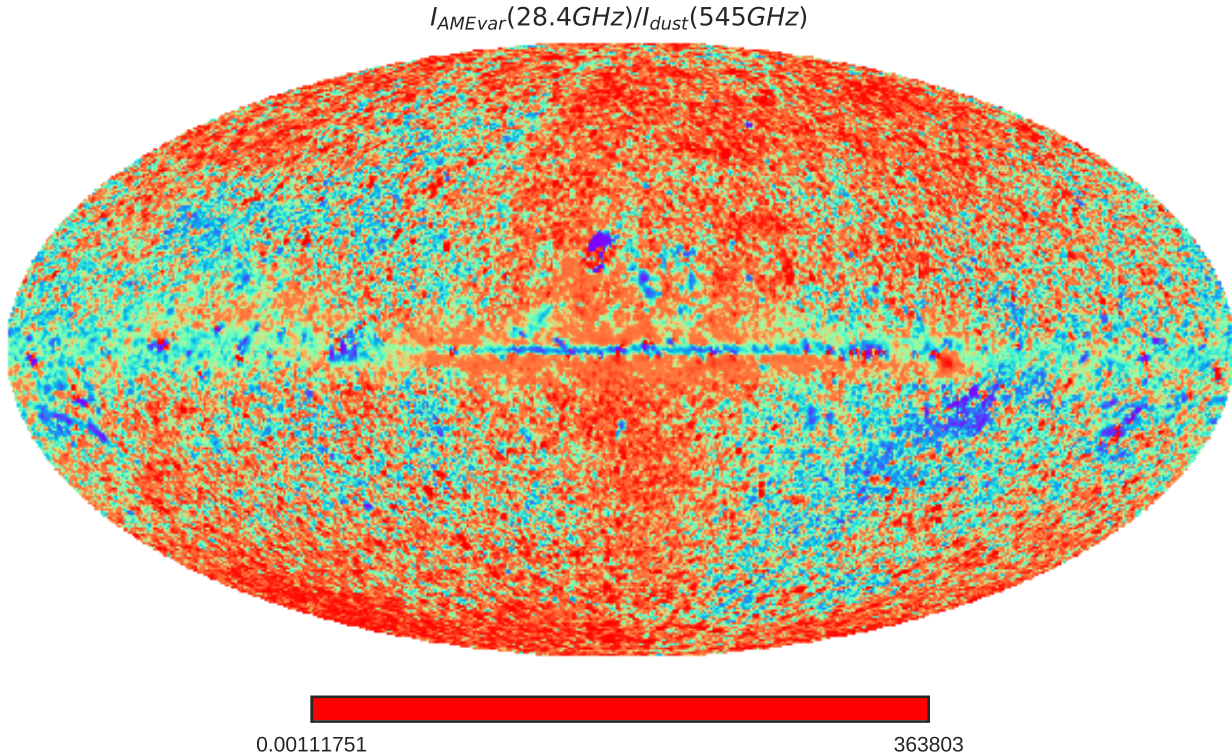


Figure 2.13: All-sky map of the ratio of two COMMANDER components- the frequency-varying AME component divided by the intensity of thermal dust emission at 545 GHz. There are some recognizable AME emission regions, such as  $\lambda$  Orionis. Large-scale patches of AME excess are noted to correspond to synchrotron emission (Hensley et al. 2016)

731 The physical parameters of the 'spdust' model itself are not directly varied in PC15X. In any  
 732 case, the spinning dust model SED shape does not show significant variation from environment  
 733 to environment (Ali-Haïmoud et al. 2009). Because of the phenenological approach of the  
 734 AME fitting method, the PC15X authors themselves suggest caution in deriving conclusions  
 735 from comparisons with the COMMANDER AME map. However it is the most thorough all-sky  
 736 component separation currently available, and has not been well analyzed relative to the full  
 737 wavelength range of available IR all-sky maps. Improving on the COMMANDER AME map will  
 738 likely require lower frequency constraints (in the red-shaded portion of Fig. 2.9) and/or higher  
 739 resolution observations of not only the AME itself but the contribution from synchrotron and  
 740 free-free emisson. This way some of the inherent degeneracies between free-free, synchrotron,  
 741 thermal dust, and AME parameters may be able to be broken.

## 2.5 All-sky Data Processing

The HFI, FIS, and IRIS maps used here are downloaded from their respective online repositories, as all-sky HEALPix<sup>13</sup> maps (Górski et al. 2005). NSIDE 2048 maps. In the case of the IRC maps, we first create HEALPix maps from the 4,857 all-sky survey tiles using the Aladin all-sky data visualization platform (Bonnarel et al. 2000). NSIDE 2048 implies an average pixel spacing of  $1.7'$ . The maps are then degraded to NSIDE 1024 before carrying out a Gaussian-beam smoothing to a  $1^\circ$  FWHM. Map smoothing itself is done in spherical harmonic space, before the maps are transformed back to position space. These steps are handled by the smoothing function contained in the `healpy` python package. Following the smoothing process, the maps are degraded once more to NSIDE 256, or  $15'$  pixel-width<sup>14</sup>. The value of each of the larger NSIDE 256 pixels, comes from the mean of its parent NSIDE 1024 pixels. The purpose of this processing is to ensure that all of the maps have the same resolution as the PR2 AME map.

---

<sup>13</sup>HEALPix core software is described at <http://healpix.sourceforge.net>. The HEALPiX python package `healpy` used in this work is available at: <https://github.com/healpy/healpy>

<sup>14</sup>HEALPix pixel scale rebinning carried out with `healpy.ud_grade`

754 **Chapter 3**

755 **Analysis of an interesting AME region:**  
756  **$\lambda$  Orionis**

757 **3.1 An interesting AME region**

758 The  $\lambda$  Orionis molecular ring, also known as the Meissa Ring is a massive stucture surrounding  
759 the  $\lambda$  Orionis O-type star. The ring contains an HII region, ionized by  $\lambda$ Ori itself and its OB  
760 associates (Murdin & Penston 1977). What had been thought of as a starforming region of  
761 missing molecular gas. At the time Murdin & Penston (1977) even speculated that this could  
762 be evidence of an alternate starformation pathway, writing: “Notably we need to know if  $\lambda$ Ori  
763 is an example of a different mode of star formation or [...] simply a case in which the progenitor  
764 molecular cloud was exhausted within the last one or two million years.”

765 Maddalena (1986); Maddalena & Morris (1987). (and references therein) noted a ring of  
766 material likely being pushed out by the central, historically well-known  $\lambda$  Orionis Association  
767 of B-type stars and surrounding HII reigon.

768 **3.1.1 Where does the ring come from?**

769 Cunha & Smith (1996) argued that the ring may have resulted from a supernova explosion,  
770 further speculating that  $\lambda$ Ori may have been a companion of the progenitor.  $\lambda$  Orionis is a  
771 known binary system, however its current companion is the a B-type star. (Murdin & Penston  
772 1977) . The central region is heated by the  $\lambda$  Orionis star itself, and the Orion OB association  
773 it belongs to (Ochsendorf et al. 2015). The region is known to host several young stellar and  
774 protostellar objects (Koenig et al. 2015).

775 At approx.  $10^\circ$  wide, we can see the outline of the structure even in the low ( $1^\circ$  FWHM)  
 776 resolution PCAME map. The ring shape itself is thought to originate from a supernova, or  
 777 perhaps combined effects of the entire star formation history of the  $\lambda$  Orionis Association,  
 778 including the formation of its surrounding HII region (Aran 2009).

### 779 3.1.2 A well-studied region

780 Although the  $\lambda$  Orionis region has been a popular target for study since approximately the  
 781 1980s. Duerr et al. (1982) wrote of the relative lack of work on the overall region: “Surprisingly,  
 782 this interesting complex has been little studied”. While this seems surprising given the numbe  
 783 of works on the region in the literature now, it is really the advent of all-sky missions that have  
 784 driven more recent interest. The large angular size is such that all-sky surveys were a natural  
 785 boon for study of such extended structures. WISE especially was a huge source of insight  
 786 (Koenig et al. 2015). More recently, Planck Collaboration et al. (2016c) strongly highlighted  
 787 the region as a strong candidate for further AME investigation.

## 788 3.2 Investigative approach

789 We have carried out an initial comparison of the AME of this region with its mid to far-  
 790 IR dust emission. The region is shown in Fig. 3.1 as it appears in  $1^\circ$ -smoothed A9 data.  
 791 The ring structure itself indicates excess microwave emission attributed to AME, from the  
 792 dominant variable frequency component  $AME_{var}$  (see Ch. 2). The central region is dominated  
 793 by free-free emission (Aran 2009; Koenig et al. 2015). Free-free emisison coming from the Hii  
 794 phase surrounding the  $\lambda$  Orionis association dominates the region’s morphology in LFI images.  
 795 (Planck Collaboration et al. 2016c). Taking the hint from Planck Collaboration et al. (2016c)  
 796 that this may be among the more reliably component separated regions, we evaluate if there  
 797 is any preferential relationship between any parameter of dust emission and the AME. Fig. 3.2  
 798 shows the expected distribution of free-free emission in the region, assuming that  $H\alpha$  line  
 799 emission is a tracer of microwave free-free. This indicates that free-free is strong within the  
 800 central region, where radiation fields are more intense, and AME is minimal. The strongest  
 801 AME follows the ring-shaped morphology outside the central bubble of free-free emission.

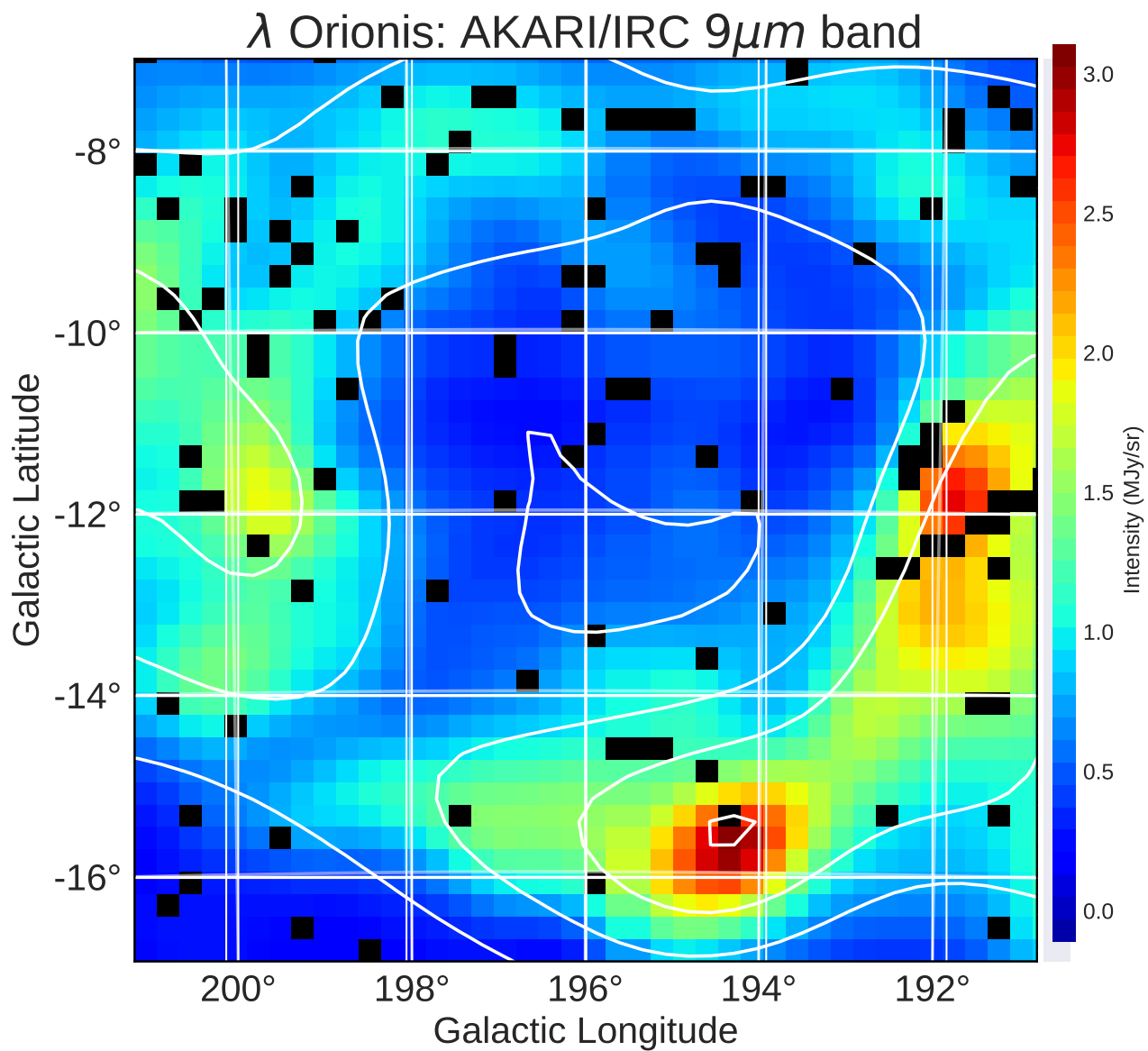


Figure 3.1:  $\lambda$  Orionis as it appears in the AKARI  $9\mu\text{m}$  data. Contours indicate the AME, as given by the Planck PR2 AME map. The image is smoothed to a  $1^\circ$  PSF (much larger than the original 10 arcsec map). The  $\lambda$  Orionis star itself is approximately located at the center of the image.

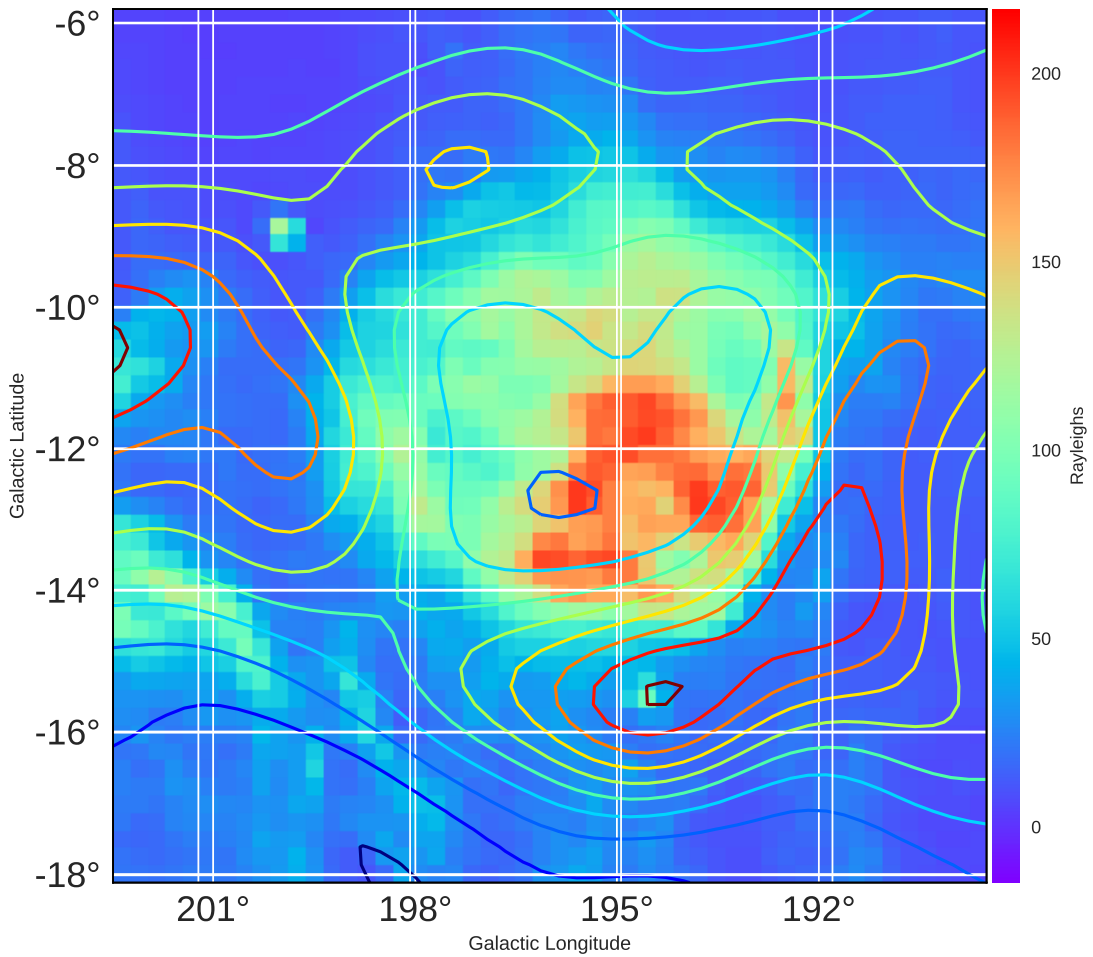


Figure 3.2:  $\lambda$  Orionis as it appears in H-alpha emission by Finkbeiner (2003). Contours indicate AME emission, from the variable frequency component. The colorbar indicates  $H\alpha$  emission in Rayleighs. The field of view is slightly larger than that used for the final processed IR comparison (Fig. 3.6).

802 

### 3.3 Data preparation

803 As indicated in Ch. 2, we use 12 photometric all-sky maps. For the IRC data (A9 and A18), we  
804 produce mosaics of  $\lambda$  Orionis from the individual tiles provided in the internal all-sky archive.

805 <sup>1</sup> For the other sources, HEALPix all-sky maps are available publicly, at sufficient resolution  
806 relative to their native resolutions<sup>2</sup>. <sup>34</sup>

807 

#### 3.3.1 Extraction from HEALPix maps

808 For the data obtained via HEALPix maps, we employ the `healpix2wcs` functionality provided  
809 in the `gnomdrizz` python package<sup>56</sup> A9 and A18 images are produced by regridding the images  
810 with the `Montage` software by NASA/IPAC. Figs. 3.4 and 3.5 show high resolution mosaics of  
811 the A9 and A18 data before processing. All of the images for all of the bands are based on a  
812 common FITS header which has a pixel grid spacing equal to the average pixel width in the  
813 NSIDE 256 HEALPix scheme.

814 

#### 3.3.2 Point-source and artifact masking

815 **Missing stripes** The AKARI all-sky survey suffers from a few missing stripe errors through-  
816 out the IRC and FIS maps (Ishihara et al. 2010; Doi et al. 2015). This is a more serious issue  
817 for FIS. They can generally be characterized as a competition for integration time between the  
818 all-sky observing mode, and pointed observations during AKARI’s cryogenic phase. Unfortu-  
819 nately for the present work, some of these stripes pass directly through the  $\lambda$  Orionis region.  
820 Figs. 3.3, 3.4 and 3.5 display the data at near-native resolution, demonstrating where these  
821 patterns occur. Additionally there are some saturated pixels in both IRC and FIS data.

822 **Point sources** A caveat that comes with added ionized PAH feature coverage of the A9  
823 band, is that the shorter central wavelength placement allows more contamination from point  
824 sources. We identify point sources with a moving-window approach provided in the astropy

---

<sup>1</sup>IRC all-sky data is still in the proprietary phase at the time of this writing, but should be public by April 2018.

<sup>2</sup>Planck data was retrieved from the NASA IPAC online archive at [http://irsa.ipac.caltech.edu/data/Planck/release\\_2/all-sky-maps/](http://irsa.ipac.caltech.edu/data/Planck/release_2/all-sky-maps/)

<sup>3</sup>AKARI/FIS data

<sup>4</sup>IRAS/IRIS data

<sup>5</sup>Available at <http://cade.irap.omp.eu/dokuwiki/doku.php?id=software>

<sup>6</sup>“drizzlib” 1.2.2 and earlier were not able to correctly access HEALPix files with multiple fields/columns.  
See appendix for our recommended workaround.

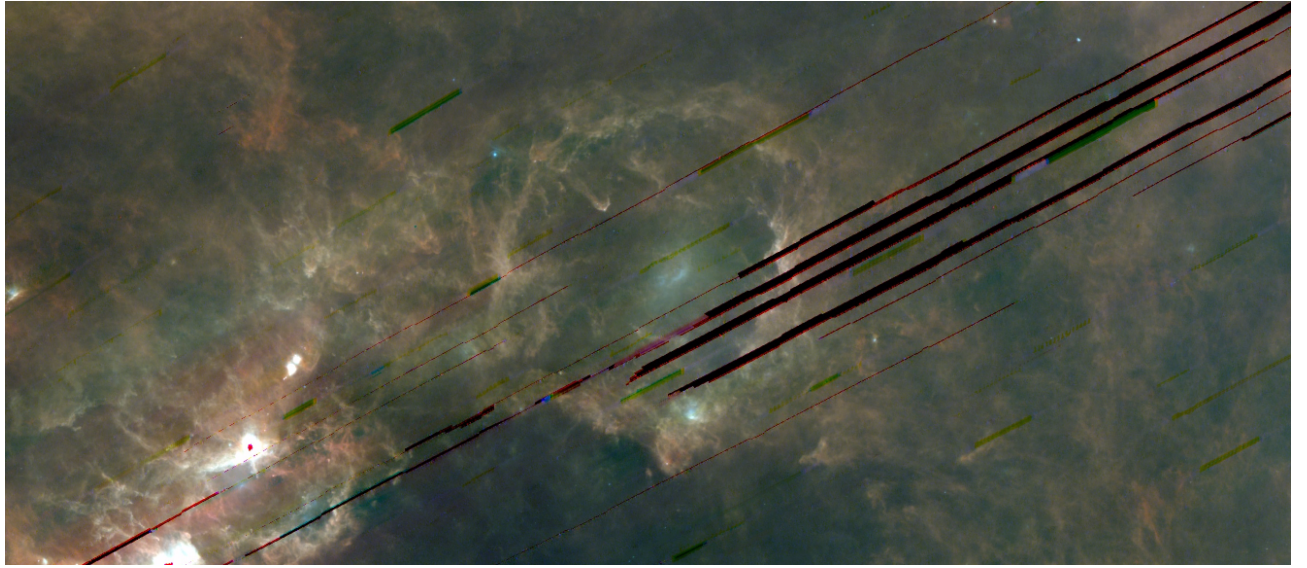


Figure 3.3: The  $\lambda$  Orionis region and its surroundings in AKARI FIS data, where A65 is blue, A90 is green, and A140 is red. The missing stripe patterns are visible, and affect all 3 bands shown here as well as the A160 data.

825 Python package, flagging pixels which have higher than  $5\sigma$  intensity among the surrounding  
 826 100 pixel window. We then place a mask at the center of the flagged point-sources. The masks  
 827 are propagated through the regridding step, such that the low-resolution pixels having more  
 828 than 50% of their area masked in the high resolution tiles, also become masked. Such pixels  
 829 appear black in Fig. 3.1. The same process is applied to the A18 data. For other maps, which  
 830 we extract from HEALPix data, we first regrid from HEALPix to rectangular grids, and then  
 831 apply the point-source search and masking as above. For the I12 and I25 images, the rejected  
 832 pixels were fewer than with A9, but positions overlapped with those already masked in A9.  
 833 For bands longer than I25, this process did not result in rejected pixels. For the D12 and  
 834 D25 bands, which are natively at a much lower resolution than AKARI or IRAS, point-sources  
 835 present more of a challenge. For these images, we visually inspect and mask 3 regions with  
 836 bright point source contamination consistent with the DIRBE beamsize and with point-sources  
 837 identified in IRAS and IRC images. Pixel positions masked in any single image, are masked in  
 838 all of the images before the final analysis.

### 839 3.3.3 PSF Smoothing

840 We smooth the pixels in the spatial domain, to have a  $1^\circ$  FWHM PSF, in order to have a  
 841 resolution approximating that of the PC AME data. The smoothing process relies on the  
 842 convolution module provided in the `astropy` package. We assume simple circular gaussian

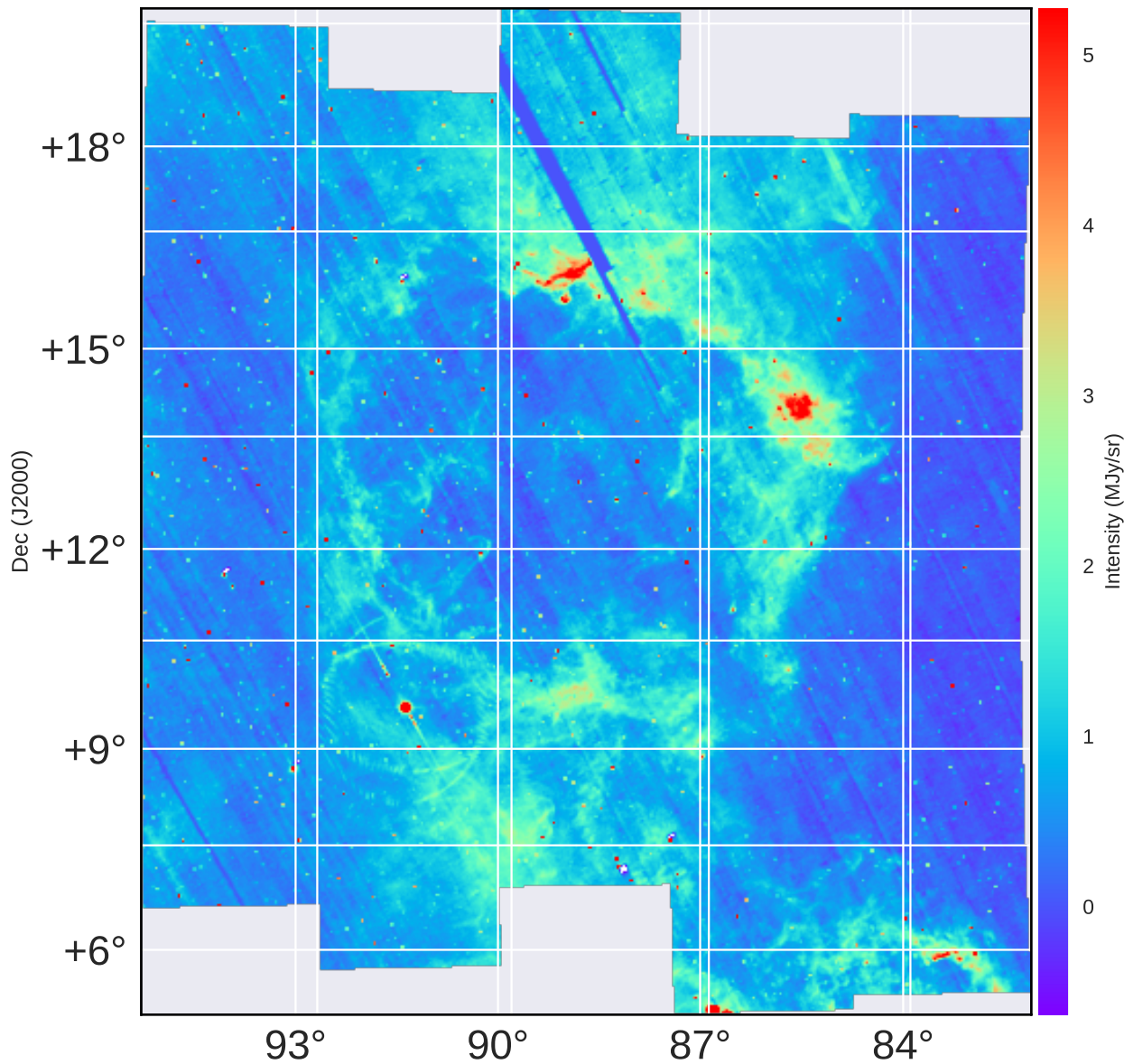


Figure 3.4: The  $\lambda$  Orionis region in the A9 band at near-native resolution. This is a mosaic created from the 3x3 degree all-sky survey tiles by Ishirara et al. (in prep.) Missing stripes are less of a problem than with the A18 band (Fig. 3.5), but point sources are more pronounced. Betelgeuse, in the lower left of the image, is bright enough in this band to produce a ring-shaped artifact.

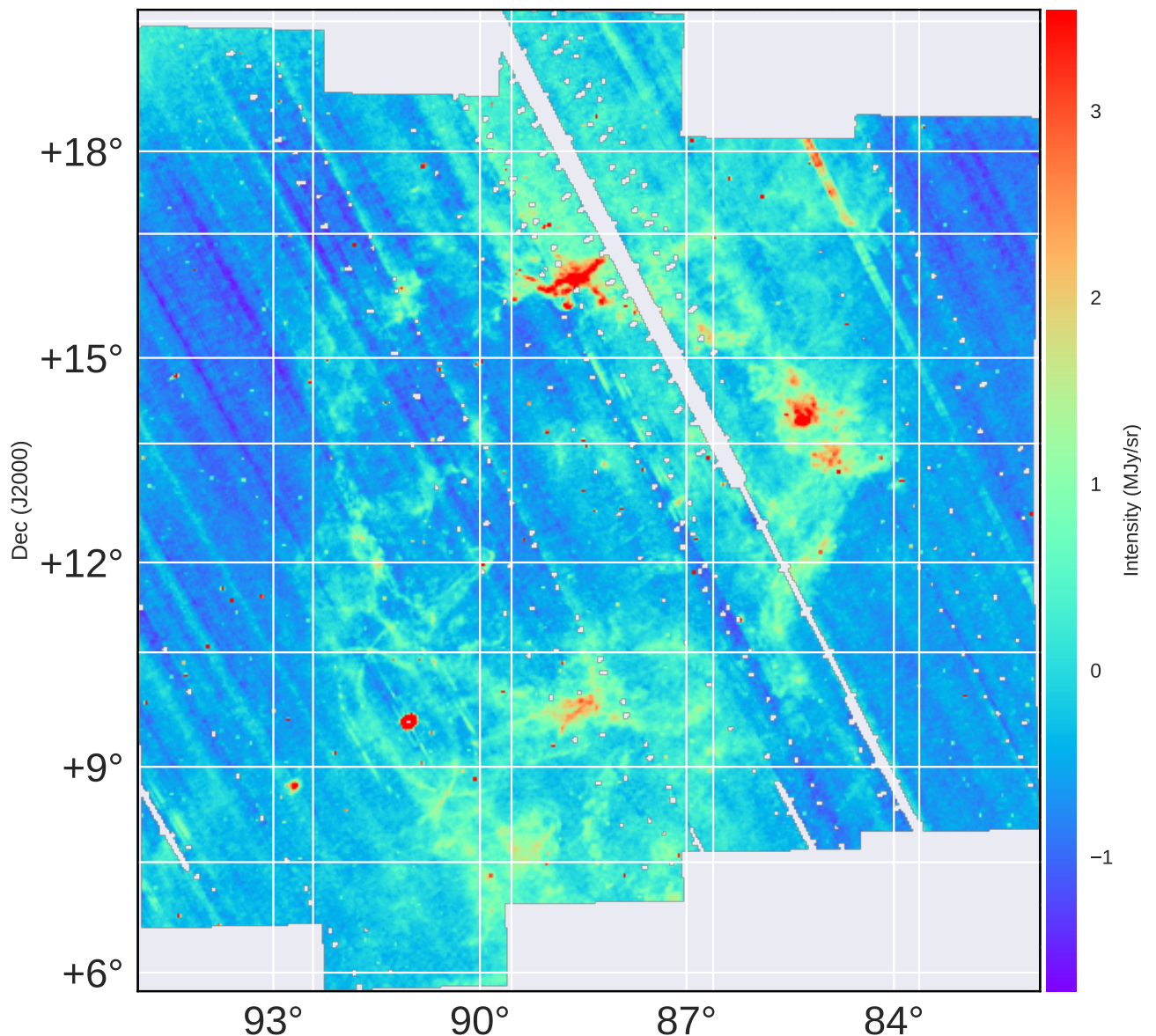


Figure 3.5: The  $\lambda$  Orionis region in the A18 band at near-native resolution, demonstrating the regions affected by missing stripe errors, but less affected by point-sources than A9 (Fig. 3.4).

843 kernel for the smoothing process. While they may be asymmetries in the effective beam shapes  
844 of the IR bands used, the target resolution of the AME data is large enough relative to the  
845 native resolution of the input IR data (especially A9 and A18, see Fig. 2.1) as to render the  
846 beam shapes and positional variations negligible. Finally, we mask pixels along the edge of the  
847 FOV where the convolution process produces artifacts.

### 848 3.3.4 Background subtraction

849 We estimate an average, flat background level for this region. The background level is deter-  
850 mined the mean of pixels in an ‘OFF’ zone. The final images are shown in Fig. 3.6, with the  
851 full mask applied (masked pixels are indicated in white), and with the OFF zone indicated by  
852 the red rectangle on each frame. We do not expect simple band-by-band intensity correlation  
853 tests with the AME to be sensitive to background and foreground emission along the line of  
854 sight towards the  $\lambda$  Orionis region. However analyses such as dust SED fitting, to determine  
855 the relative abundances of different dust components, may be effected by the background level.  
856 The general morphology as seen in the high resolution AKARI data (Figs. 3.3, 3.4 and 3.5)  
857 remains well pronounced in the final, low resolution images.

## 858 3.4 Multi-wavelength characterization

859 The correlation matrix results corresponding to data shown in Fig. 3.6, are shown in Fig. 3.7.  
860 This immediately confirms a correlation between the IR and AME, however this was readily vis-  
861 ibly from the spatial morphology of the region. Interestingly though, the correlation strengths  
862 with  $AME_{var}$  show a pattern from short to long wavelengths: A9, P857, and P545 show the  
863 strongest correlations, with the correlation weakening from A18 to A90, and again strengthening  
864 at longer wavelengths. The fixed peak frequency  $AME_{fix}$ , which is the much fainter component,  
865 shows the strongest correlation with A90- though all of the IR correlations relative to  $AME_{fix}$   
866 are weaker than those for  $AME_{var}$ . The overall pattern is for bands dominated by PAH emis-  
867 sion (as discussed in Ch. 2), and those which trace Rayleigh-Jeans thermal dust emission are  
868 equally good predictors of the AME. Bands dominated by a mixture of VSGs, and warm dust  
869 emission, show a weaker correlation. For the next stages of analysis, we will consider only the  
870 dominant component  $AME_{sum}$ , however the results are not sensitive the choice of  $AME_{sum}$  or

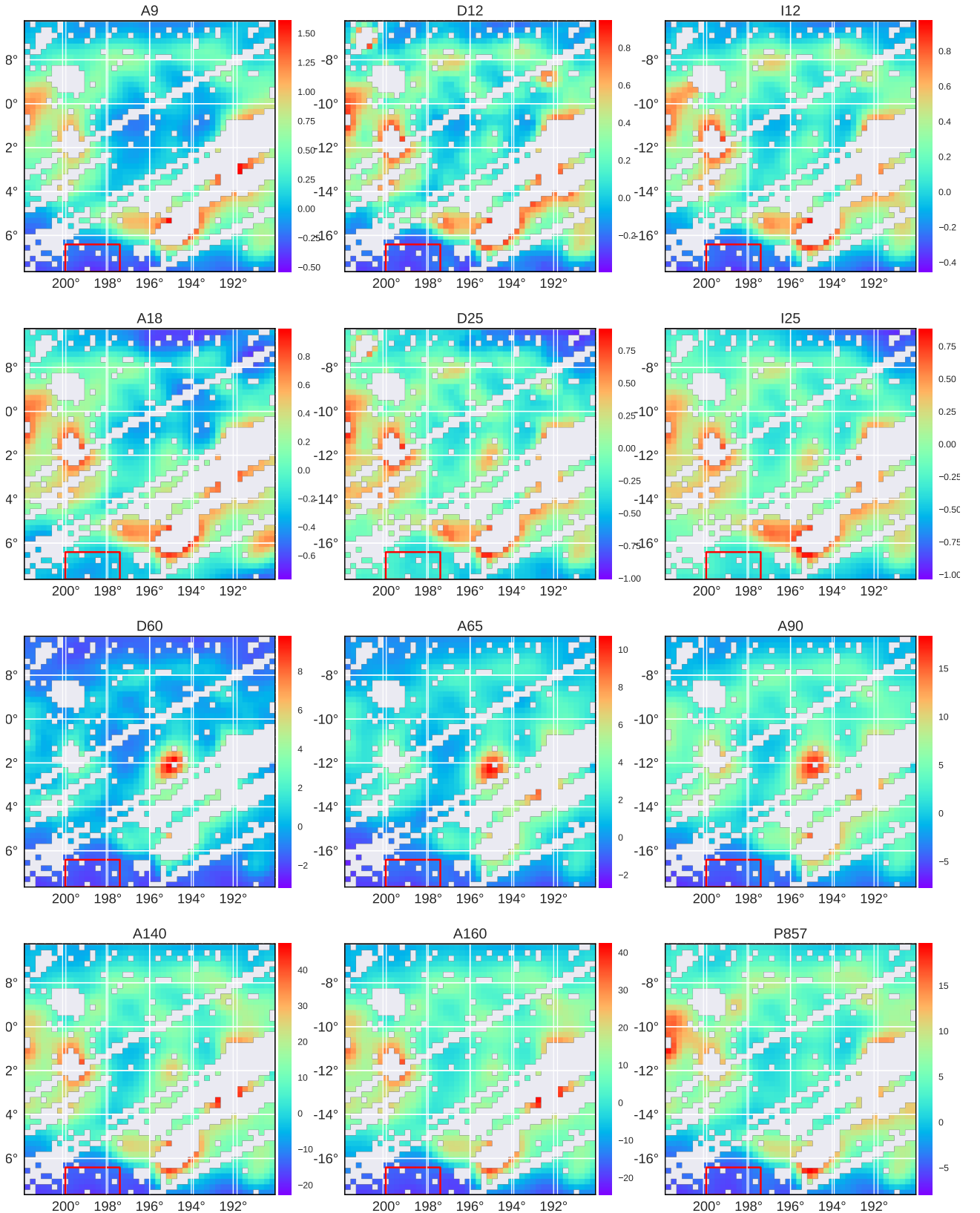


Figure 3.6: Processed data at each wavelength for  $\lambda$  Orionis. A flat background has been subtracted from each frame based on the mean of pixels within the red rectangle. The pixel width is  $0.25^\circ$ , with the data PSF smoothed to  $1^\circ$  spatial resolution. Masked pixels (point sources, stripe errors, convolution artifacts) are shown as white. The frames share the same FOV and GAL-TAN projection. Colorbars indicate the intensity in MJy/sr.

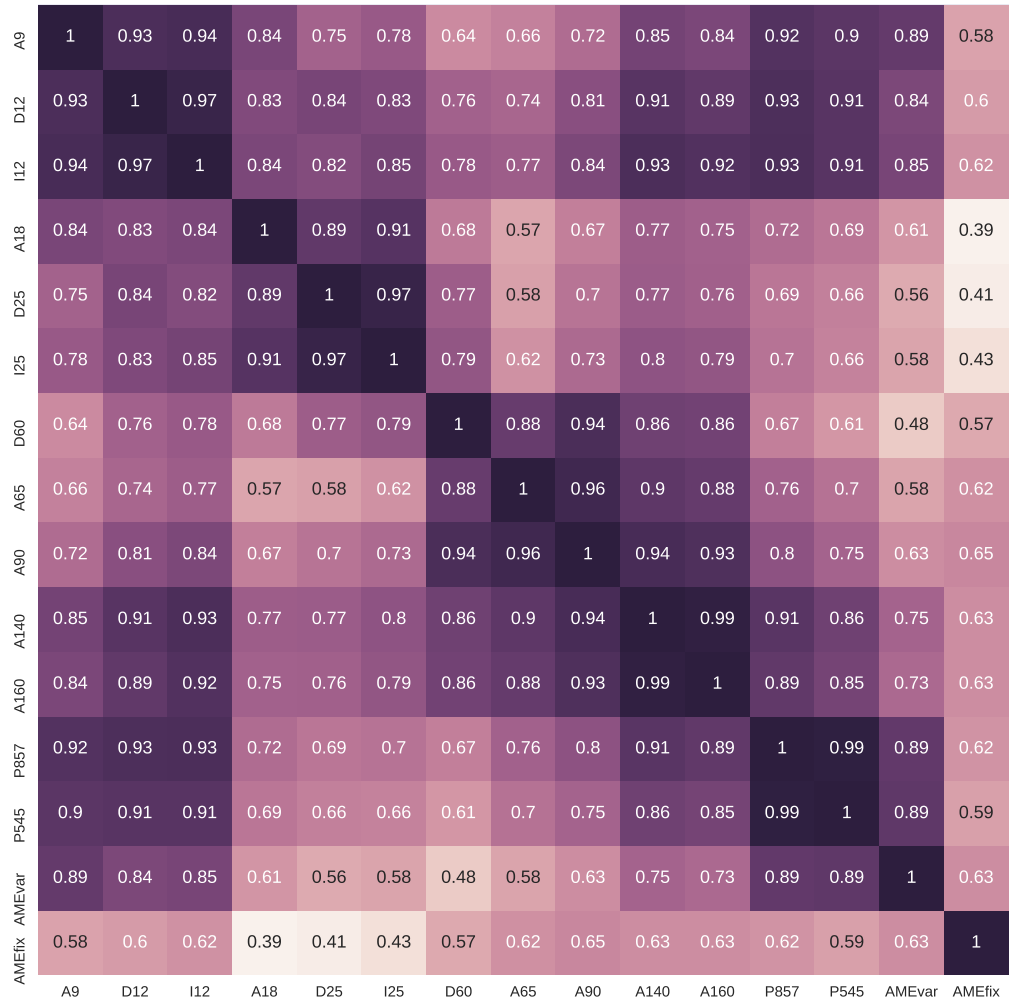


Figure 3.7:  $r_s$  correlation matrix for all of the data used in the  $\lambda$  Orionis analysis, similar to that presented for the Planck Commander component maps in Fig. 2.8. The shade and annotation for each cell indicates the  $r_s$  score, where  $r_s$  of 1 indicates a monotonically increasing relationship for a given pair of images. The two AME components, as described in Ch. 2, are listed separately:  $AME_{var}$  for the frequency-varying component, and  $AME_{fix}$  for the constant frequency component.

---

871  $AME_{var}$ .

872 Comparing the images in Fig. 3.6, most of the variation in the correlation scores appears  
 873 to come from the central region of  $\lambda$  Orionis. Because of the known heating present within the  
 874 ring, from the  $\lambda$  Orionis association, and given the brightening of bands between A18 and A90,  
 875 this variation appears to be due to a temperature increase.

876 **3.4.1 Bootstrap analysis**

877 To assess the robustness of the correlation scores, we employ the Bootstrap re-sampling ap-  
 878 proach, first introduced by Efron (1979) (see Feigelson & Babu (2013) for an updated description  
 879 within an astronomical context). This involves creating random re-sampled sets of the data.  
 880 We use the 'with replacement' approach, meaning that a data point may be selected multiple  
 881 times in a single re-sampling iteration. The size of the re-sampled set is the same as the input  
 882 set size. For each random set we run a correlation test, resulting in a distribution of correlation  
 883 coefficients. This allows us to estimate error bars for the correlation scores, and effectively  
 884 de-weight outliers within each sample. We carry out bootstrap correlation tests for each IR  
 885 band's intensity vs. the  $AME_{sum}$  integrated intensity. The data are resampled 10,000 times for  
 886 each correlation test, a sufficient resampling given the unmasked pixel count of  $\sim$ 1400 pixels,  
 887 and considering that the effective beams are somewhat undersampled. This is repeated for  
 888 both  $r_s$  and  $r_p$  based tests, in order to assess variations in degree of linearity among the various  
 889 IR:AME trends. The distributions of the bootstrap resamplings are shown in Fig. 3.8. For  
 890 both test cases, the best correlations are the longest and shortest wavelength bands, consistent  
 891 with the straight-forward  $r_s$  scores shown in Fig. 3.7. In the  $r_p$  case, the strongest correlation  
 892 is the A9 band vs the AME.

893 **3.5 Comparison with SED Fitting**

894 We performed a full dust SED fitting on the  $\lambda$  Orionis photometry, according to the dust  
 895 model by Galliano et al. (2011) (to be thoroughly introduced in Galliano, et al., in prep.) We  
 896 used a mixture of silicate and carbonaceous dust, silicate dust, the two dominant categories  
 897 of interstellar dust as described in Ch. 1. However, instead of the graphite-based carbon dust  
 898 invoked by the canonical Draine & Li (2007b) model (DL07), we assume amorphous carbon.

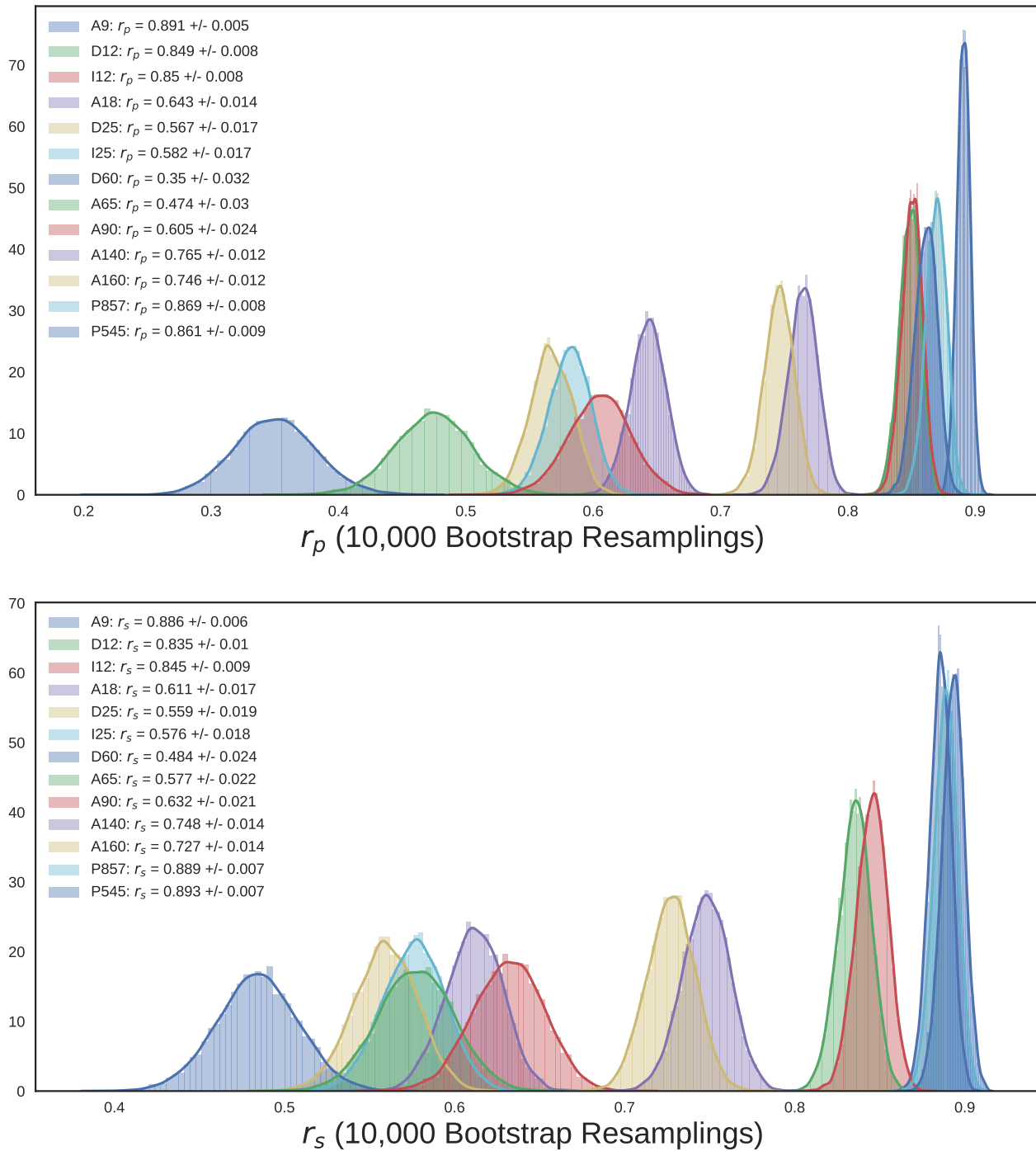


Figure 3.8: Re-sampled (Bootstrap) correlation tests for IR emission in  $\lambda$  Orionis vs. AME, for both  $r_p$  (upper) and  $r_s$  (lower) cases. Each band's  $r$  distribution is shown in a different color (the same color scheme for both plots). The width of the distribution indicates the error for the given data in the correlation coefficient. The mean and standard deviation of the scores are given in the legend of each plot. The plot ranges only show positive values, since no negative scores were produced.

This choice is an attempt to account for the “sub-mm excess” of dust emission, reported by Israel et al. (2010); Bot et al. (2010), in the Large Megallanic Cloud (LMC). The increased emissivity of amorphous carbon (a factor of 2-3 more than DL07) allows a better fit to Herschel observations of the LMC (Galliano et al. 2011), and Planck observations of the Milky Way (Planck Collaboration et al. 2016d). We assume that the radiation field heating this dust mixture is the Galactic ISRF (Mathis et al. 1983), scaled by a factor  $U$ . We utilize both the Bayesian dust SED fitting approach by Galliano (in prep.), and a least-squares analysis. The SED fitting accounts for estimates of the respective calibration uncertainties, and the spectral response curves (Fig. 2.1). As outputs, metrics of the total dust mass  $M_{dust}$ , PAH mass  $M_{PAH}$ , ionized PAH mass  $M_{PAH+}$ , and ISRF intensity  $U$  are produced. We only carry out the fitting for unmasked pixels. We are primarily interested in which of the correlations  $M_{dust}$  vs.  $I_{AME}$  or  $M_{PAH}$  vs.  $I_{AME}$  is stronger. Two sample fitting results are shown in Figs. 3.9, and 3.10. Performing such fits for all of the pixels, we are able to see how  $I_{AME}$  varies with the bulk dust physical characteristics of the region. Fig. 3.11 shows the fitted dust mass per pixel, relative to the AME intensity. AME intensity is scaled by the ISRF intensity  $U$ . Although spinning dust emission is not predicted to vary directly with  $U$ , we consider that the ISRF may serve as a diagnostic of environmental conditions in the ISM. In any case, we find that performing such a scaling improves the correlations with dust mass. Figs. 3.12 and 3.13 describe the variation with  $M_{PAH}$  and  $M_{PAH+}$ . Based on the dust properties derived from these SED fits, we investigate whether any fitted parameter shows a preferential relation with the AME. Figs. 3.11-3.13 reveal a very similar trend between the AME and the parameters  $M_{PAH}$ ,  $M_{PAH+}$ , and  $M_{dust}$ . There is a slightly improved correlation between  $M_{dust}$  and  $M_{PAH}$  (0.857 vs 0.867). This is consistent with the intensity cross correlations in Fig. 3.7. These correlations are discussed further in Sec. 3.6 and Fig. 3.16.

### 3.5.1 Comparison with unmasked results

To assess the effect of applying the mask and background subtraction from Sec. 3.3, Figs. 3.14 and 3.15 show a very simplistic version of the image processing. No point-source masking, background adjustment, or missing strip masking are applied. Data are simply smoothed with a 1-degree Gaussian beam, and missing data are interpolated. Contours indicate the region’s shape in the PCAME map. Figure 3.15 shows IR to AME cross correlation plots, for all pixels

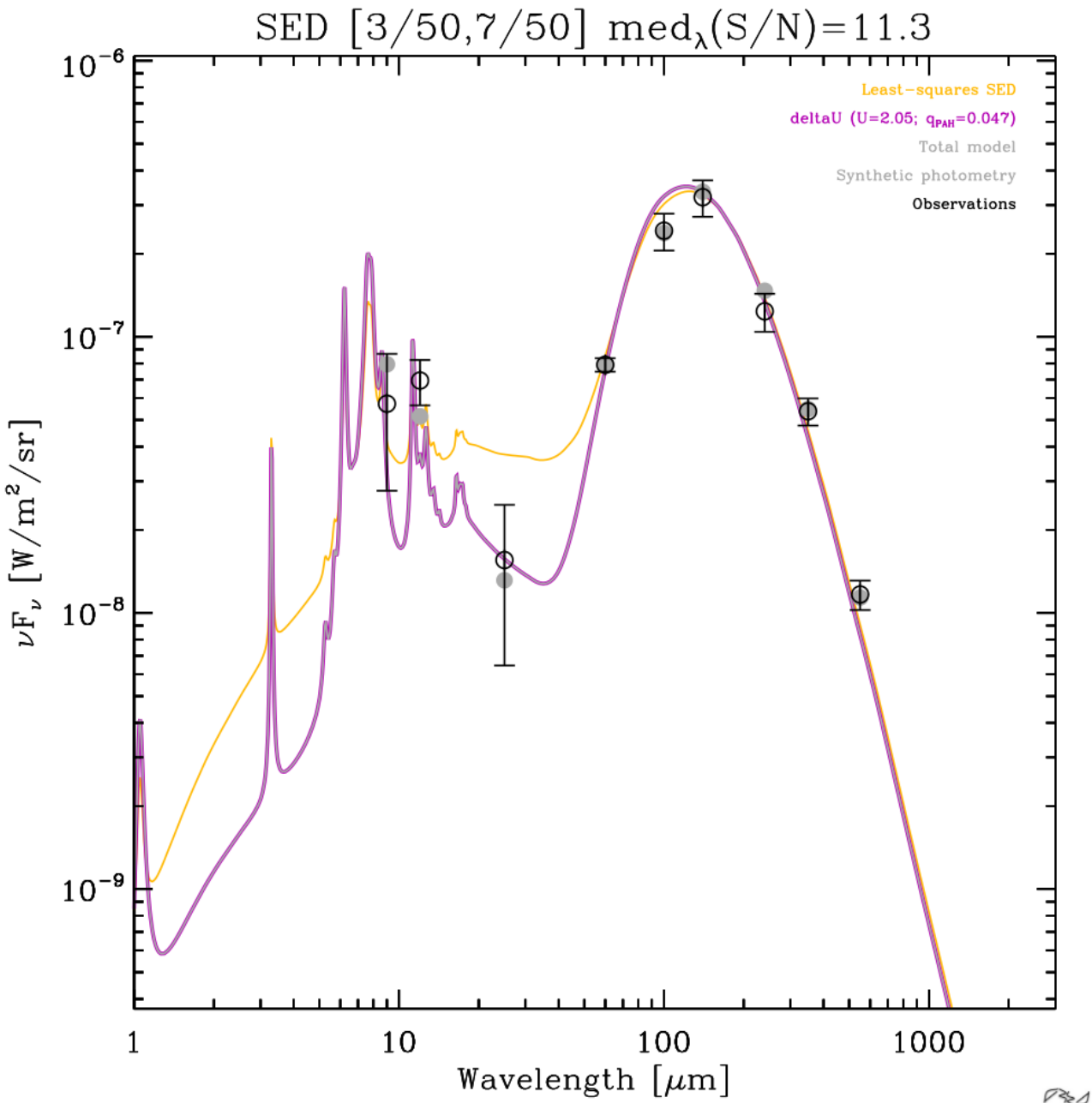


Figure 3.9: Observed (black circles and errors) and synthetic photometry (gray dots) SED of a pixel within  $\lambda$  Orionis, along with the dust SED model fit results. Two SED fits are shown: one for the Bayesian fitting (magenta), and another showing the standard least-squares result for comparison (yellow). The fitted ISRF strength  $U$ , and fraction of mass in PAHs,  $q_{\text{PAH}}$  are also given.

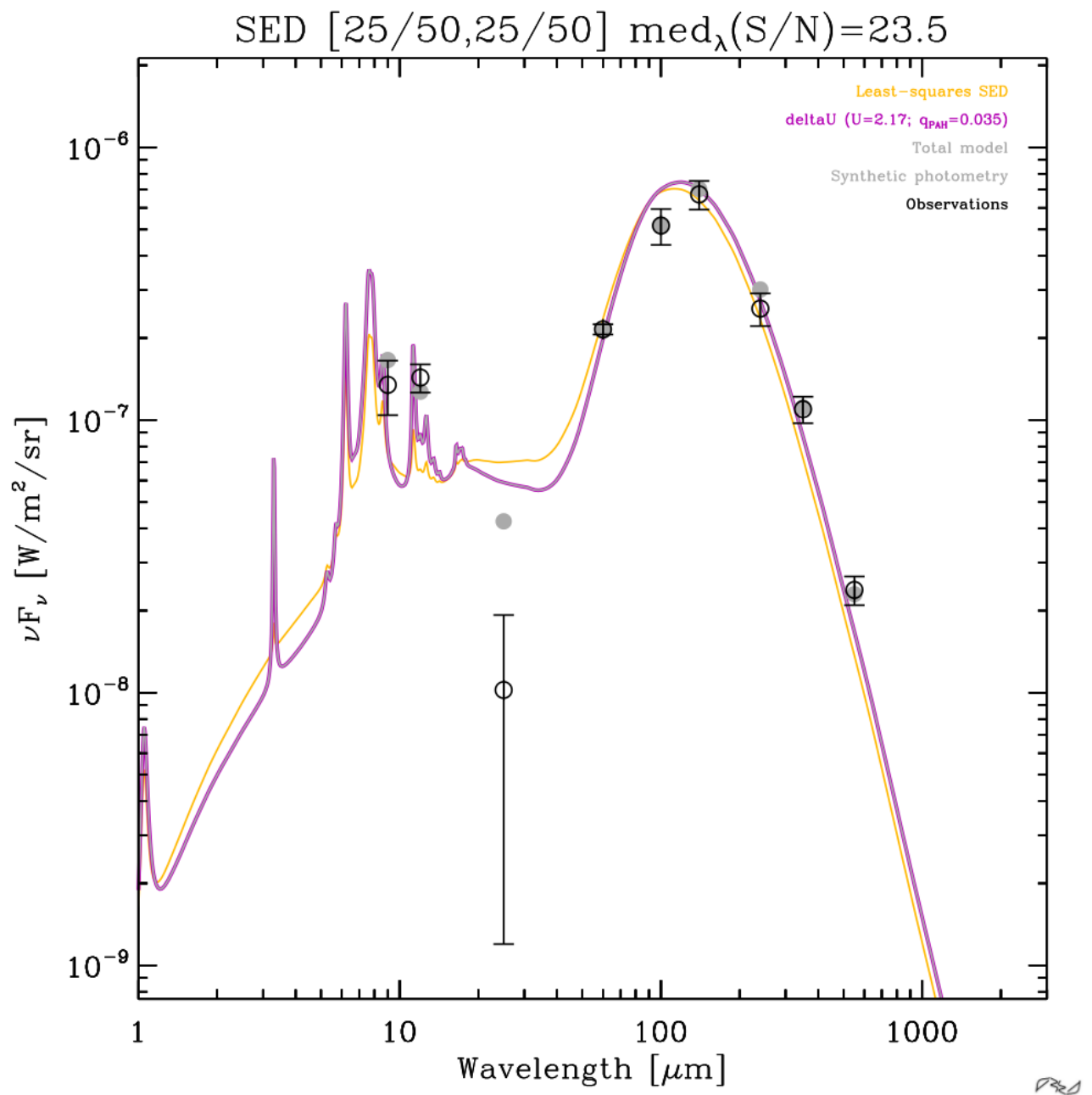


Figure 3.10: The same as Fig. 3.9, but for a different pixel position. Corresponds to galactic coordinates...

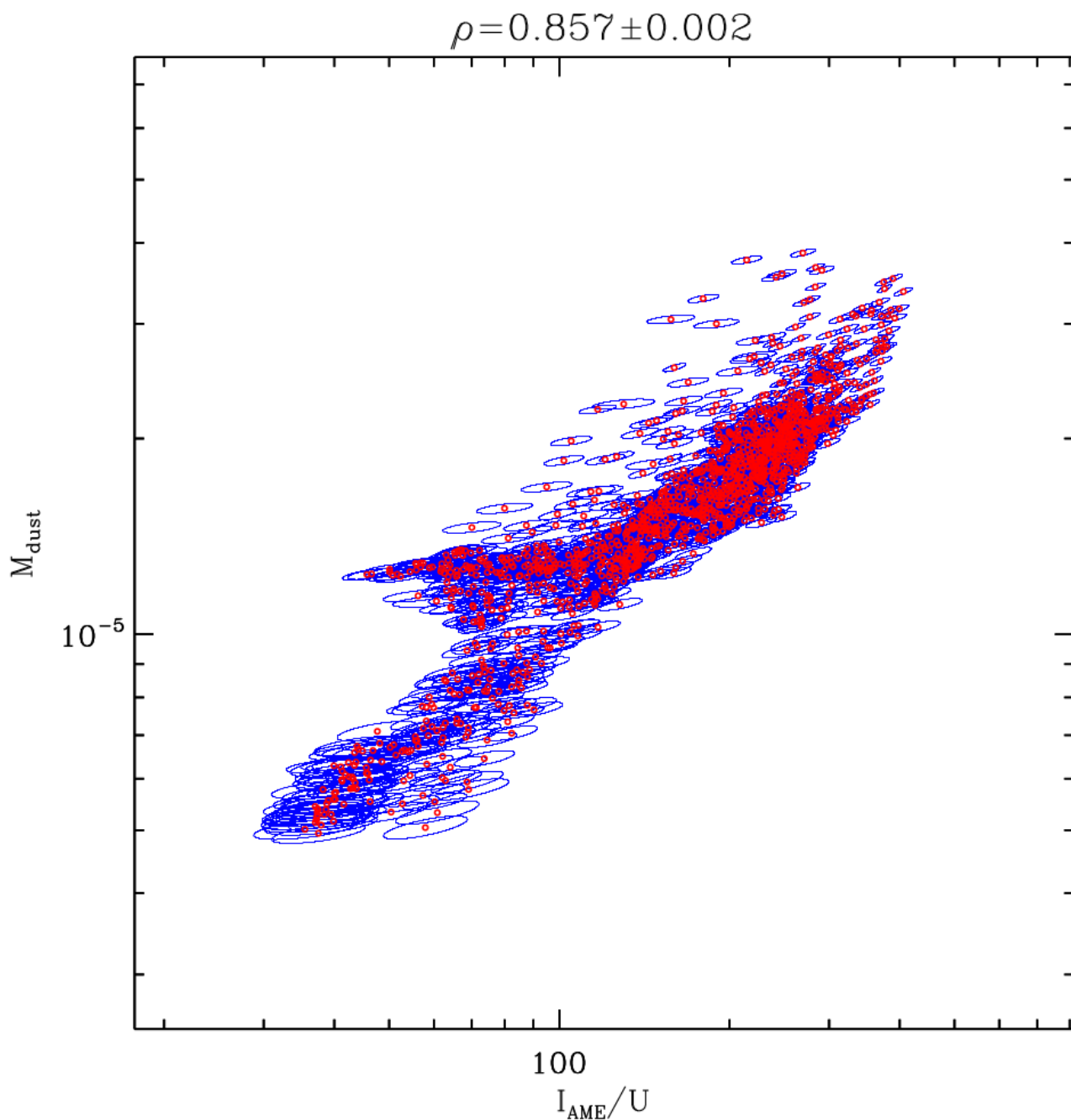


Figure 3.11: Scatter plot with error ellipses generated through the Bayesian SED fitting, of total dust mass  $M_{dust}$  vs.  $I_{AME}$  scaled by  $U$ .

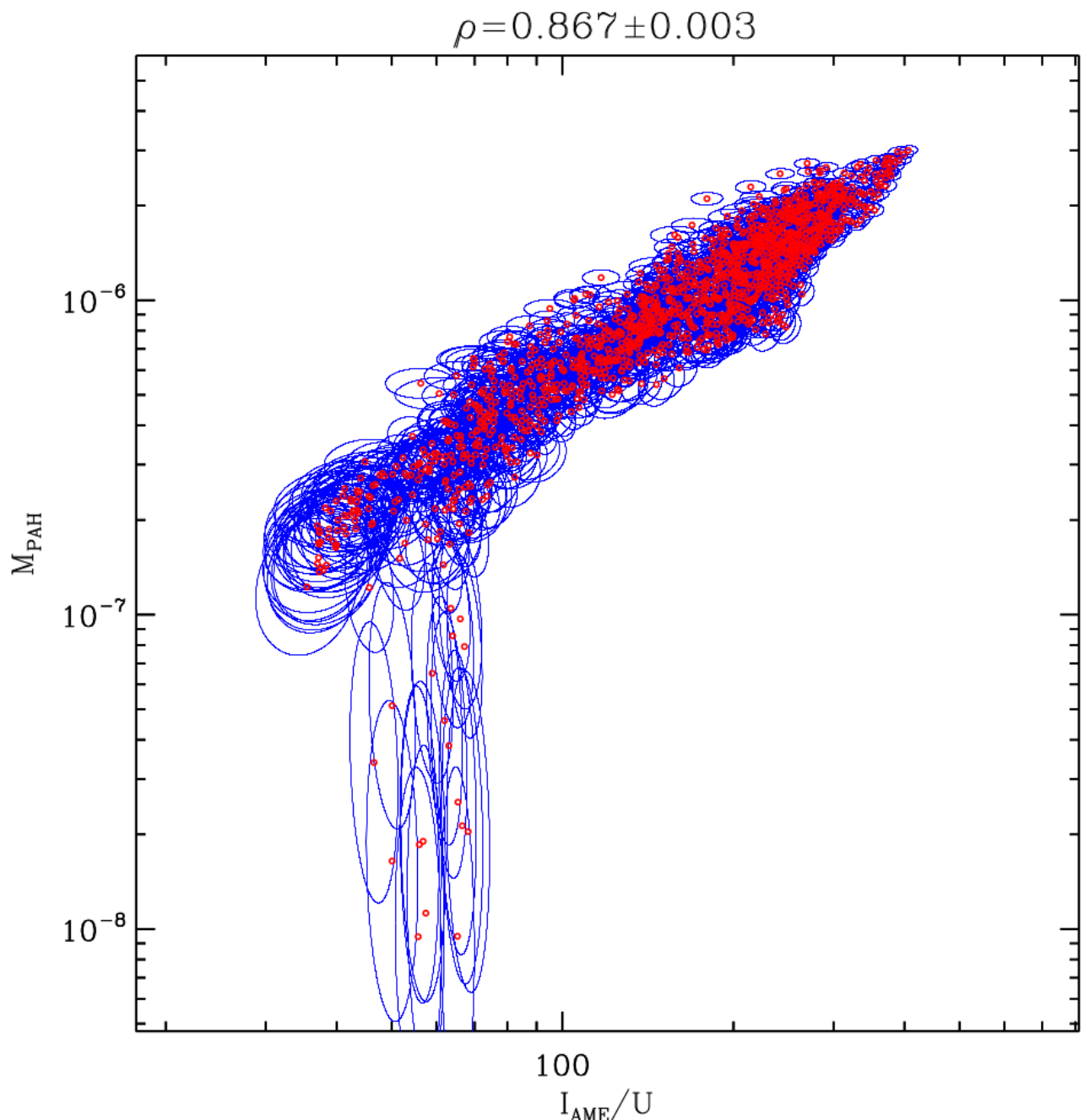


Figure 3.12: The same comparison is given by 3.11, but showing total mass of PAHs ( $M_{PAH}$ ) rather than total dust mass on the y-axis.

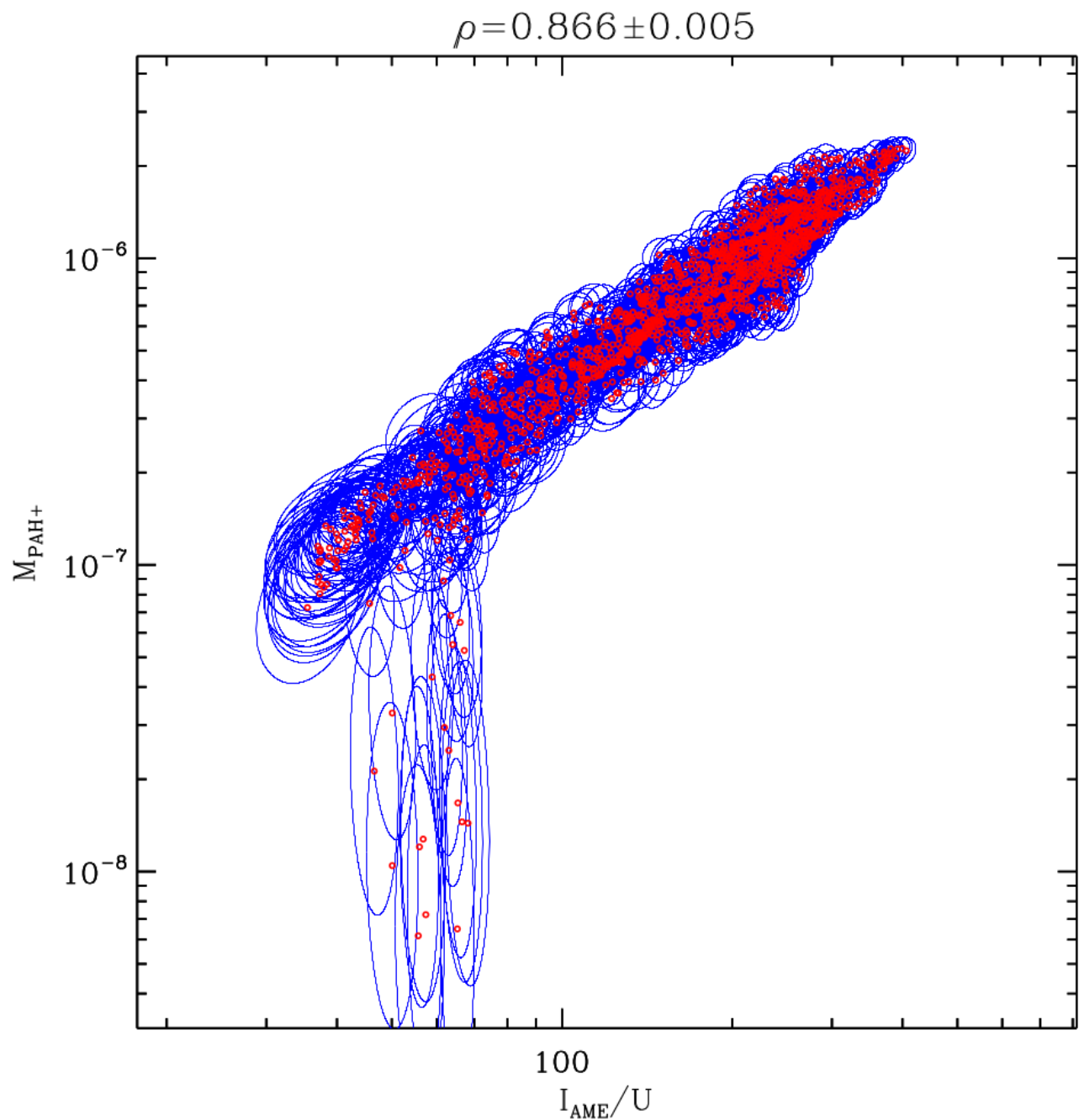


Figure 3.13: The same as in Figs. 3.11 and 3.12 , but specifically comparing an estimate of the charged component of PAH mass  $M_{PAH+}$ . This includes anions and cations, since we cannot distinguish between these two spectroscopically.

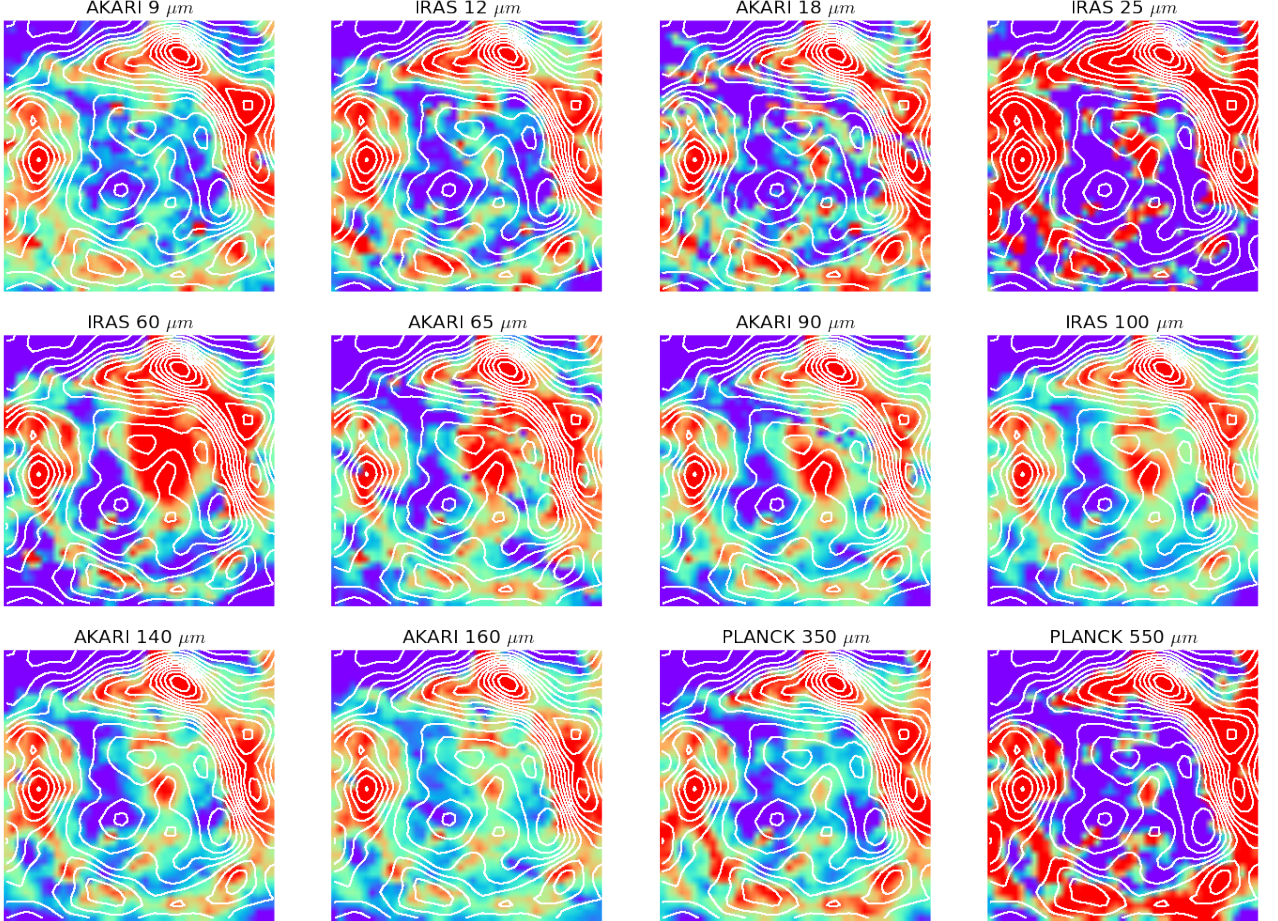


Figure 3.14: A grid of thumbnails showing the  $\lambda$  Orionis region's structure, at 12 wavelengths, along with AME contours (shown in white counts). Spatial correlation seems to be the best at the shortest and longest wavelengths (AKARI/IRC 9  $\mu m$  and Planck/HFI 550  $\mu m$ ). The images are only smoothed and interpolated, for demonstration of the effects without other image processing steps (i.e. background subtraction, point source masking). Figure 3.1 demonstrates the actual pixel grid used for the SED fitting and intensity correlation tests.

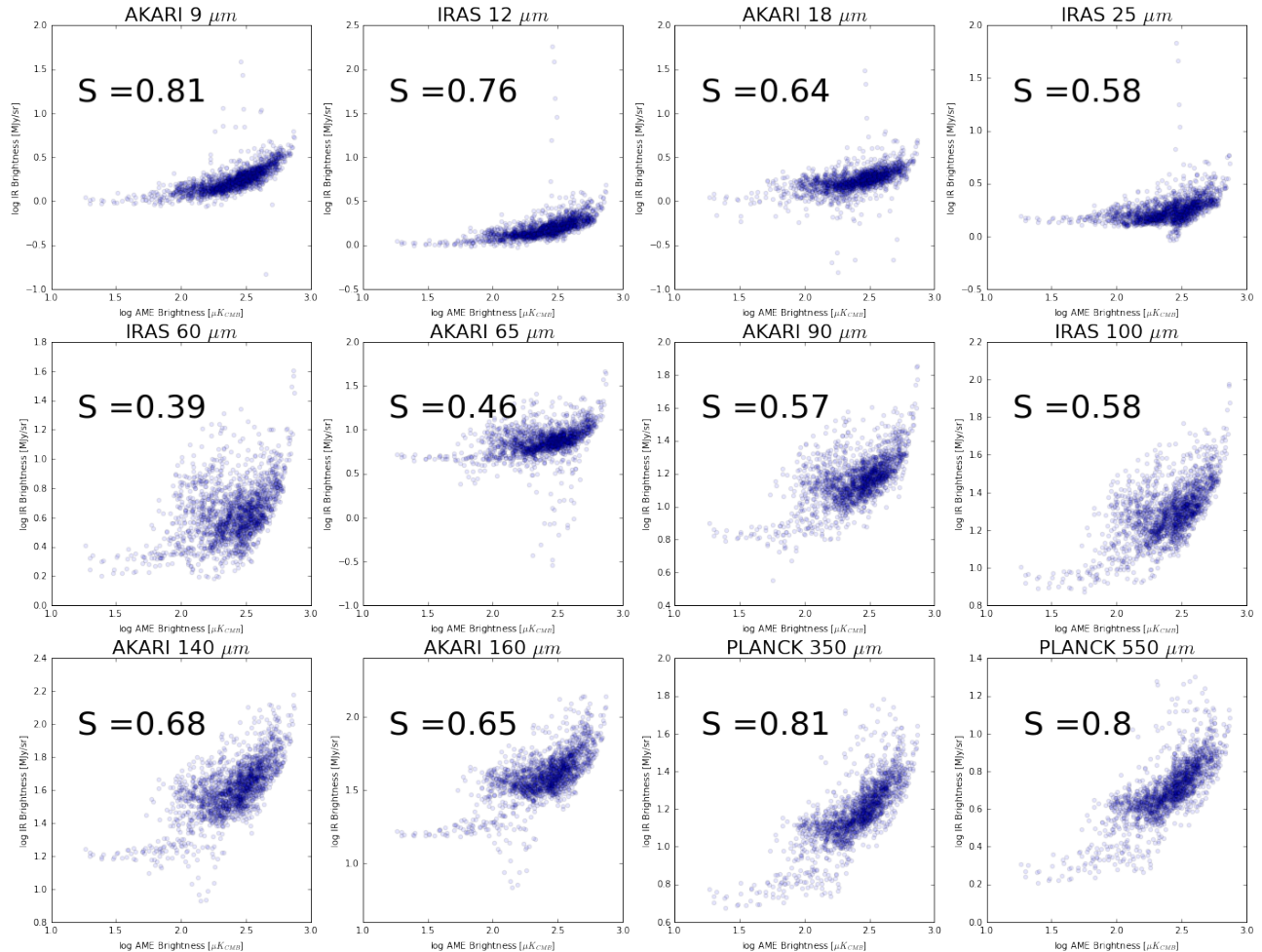


Figure 3.15: Intensity cross-correlation for all pixels in the  $\lambda$  Orionis cut-out region.  $r_s$  indicates the Spearman rank correlation coefficient for each plot.

within the  $10^\circ$  by  $10^\circ$   $\lambda$  Orionis region. Using this more crude processing, we see in Fig. find the same general pattern— A9 and P545 show the tightest correlation. Thus the overall result, in terms of a ranking of correlation strengths, does not seem to depend heavily on the image processing steps applied.

## 3.6 Discussion

In  $\lambda$  Orionis we found that across the whole region, A9 emission and P545 emission were the most strongly correlated with AME. This is apparent both in the photometric band analysis, and in the dust SED fitting. The fact that the correlation strengths of PAH-tracing mission and sub-mm emission are similar is in-line with what we have seen in Ysard et al. (2010) and Hensley et al. (2016). In those works, the two relationships (MIR vs. AME and FIR vs. AME) are very close, although these two papers are odds as to which relationship is stronger, and thus in their final interpretation. With the present data and analysis of  $\lambda$  Orionis, we fail to rule out PAHs as carriers of the AME. Fig. 3.16 indicates that although total dust mass and PAH mass are both correlated with AME, there is a strong ( $\sim 100\%$ ) probability that PAH mass is the stronger predictor of AME intensity. The results are consistent with a scenario in which PAH mass, cold dust, and the AME are all tightly correlated. A correlation between cold dust and PAHs is observed in extragalactic targets (Haas et al. 2002), and may be inferred from the correlation between UIR and FIR emission reported in diffuse galactic ISM (Onaka et al. 1996). In the case that AME emanates from spinning PAHs, it is not surprising that cold dust would also correlate with the AME. Weaker correlation from 25 to  $70 \mu\text{m}$  may indicate that AME is weaker in regions of warmer dust and stronger radiation fields. Such an anti-correlation with harsher radiation are consistent with the carriers of AME being destroyed in the central region of  $\lambda$  Orionis, thus leading to substantially decreased spinning dust emission.

### 3.6.1 PAH Ionization fraction

As described in Ch.2 it is expected that relative variations between the A9 and I12 intensities could be explained by the fraction of PAHs that are charged,  $f_{PAH+}$ . Spectroscopically, we cannot distinguish between PAH anions or cations. However if spinning dust emission arises from anions, a better correlation with the mass of charged PAHs  $M_{PAH+}$  is expected. However

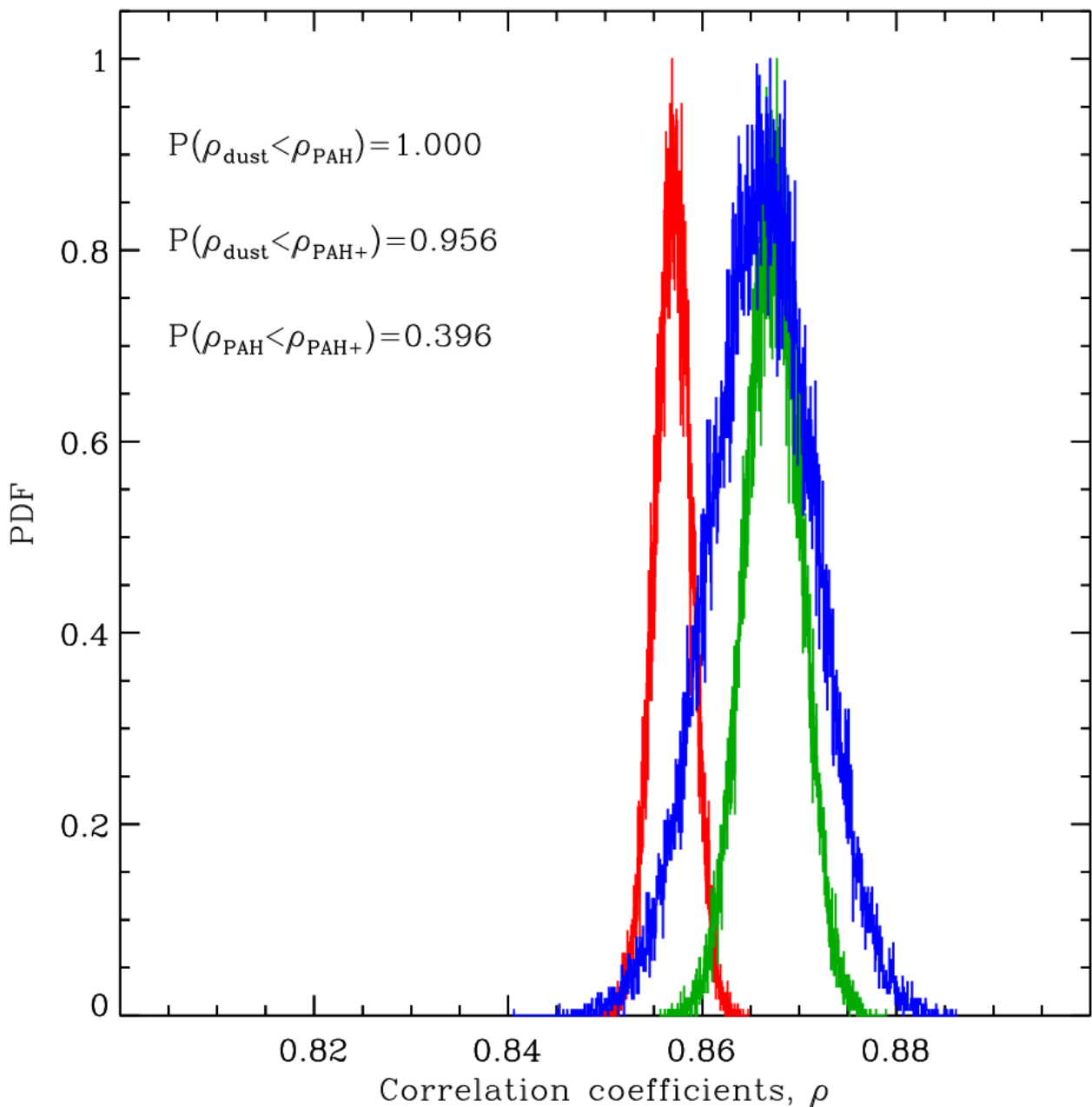


Figure 3.16: The Bayesian correlation probability distributions of Pearson's  $\rho$ ) for the three physical parameters vs. the AME intensity: total dust mass,  $\rho_{\text{dust}}$  (red); total PAH mass  $\rho_{\text{PAH}}$  (green); and only the ionized PAH mass  $\rho_{\text{PAH}+}$  (blue). Also given are the probabilities of either PAH component being better correlated with AME than dust mass, as well as the probability that ionized PAH mass correlates better than total PAH.

if the PAHs are positively charged, a stronger correlation with  $M_{PAH+}$  is not expected. This is due to the rotational excitability of the PAHs: anions are more susceptible to rotational excitation by  $H^+$  and  $C^+$  collisions(Ali-Haimoud 2010).

Examining  $\lambda$  Orionis in intensity, we find that the A9 intensity correlates more strongly with AME than I12 or D12. In the  $r_p$  case, A9 correlates more strongly with AME than any other band. This is consistent with the spinning PAH hypothesis, and taken alone may indicate that the 6.2  $\mu\text{m}$  feature emission from charged PAHs, may be a better predictor of AME intensity.

As shown by the dust SED fitting however, the probability distributions (Fig. 3.16) of  $r_p(M_{PAH+} : I_{AME})$  do not indicate that ionized PAH mass correlates better with the total PAH mass. Attempts to estimate the  $M_{PAH+}$  based on the available data appear to only add noise relative to  $r_p(M_{PAH} : I_{AME})$ . The means of the two distributions  $r_p(M_{PAH+} : I_{AME})$  and  $r_p(M_{PAH} : I_{AME})$  are similar and  $r_p(M_{PAH+} : I_{AME})$  shows a wider distribution. Thus the question of whether or not AME comes predominantly from charged PAHs remains open.

The fact that A9 correlates more strongly than the 12  $\mu\text{m}$  bands, at least suggests that this topic is worth further investigation. What is clear from the MIR and AME morphology however, is that there is a transition from a relatively PAH depleted, warmer, stronger ISRF in the center and warm dust in the center to a PAH-supporting region in the ring. Along this transition, there must be a decreasing radiation field with distance from dimnant heating sources, in  $\lambda$  Orionis association. Andrews et al. (2016) predict a transition of PAH species along such a radiation field gradient, from complete PAH destruction in harsh environments, to survival of (sufficiently large) PAH anions near the surface of molecular clouds. Thus if our stronger correlation with A9 indicates charged PAHs, this could be consistent with PAH anions surviving in the portions of  $\lambda$  Orionis which are emitting the strongest AME. Future wide-area spectral mapping of the  $\lambda$  Orionis region may be able to conclusively test for increased  $fPAH+$  in regions with stronger AME. Such studies would eb strongly aided by higher resolution probing of spatial variations the AME spectral profile.

983 **Chapter 4**

984 **All-sky Analysis**

985 What we present here is a test of the generalizability of results from Ch.3, which focused on a  
986 particular structure on the sky,  $\lambda$  Orionis. We first would like to note that “all-sky analysis” can  
987 be a bit misleading. The term tends to lead readers to the idea of a definitive study, answering  
988 a particular question for any given position on the sky. While a truly all-sky analysis would  
989 be ideal, signal-to-noise constraints (mainly at high galactic latitudes), as well as confusion  
990 along the line of sight (mainly in the galactic plane), make a uniformly powerful study of the  
991 whole sky very challenging. Here we will indeed show results for the entire sky as a benchmark  
992 analysis, but for the core analysis we must mask certain regions dominated by systematic effects  
993 in order to minimize biases for particular wavelenghts.

994 **4.1 Resolution matching**

995 **Smoothing**

996 As in Ch. 3, this approach applies to a spatial resolution of approximately  $\sim 1^\circ$ . The resolution  
997 limittation is imposed by the PC microwave component maps, which list an ‘effective resolu-  
998 tion’ of  $60'$  (Planck Collaboration et al. 2016b). Thus we must apply a smoothing to most of our  
999 input datasets, which have native resolutions of a much finer scale (see Tab. 2.1 and Fig. 1.2).  
1000 The data also come in a wide range of beam shapes with their own degrees of uncertainty,  
1001 thus we conservatively smooth all of the data in the same way, using a circular Gaussian beam,  
1002 to have  $\sim 1^\circ$  FWHM resolution. We start with an all-sky AME to IR comparison, looking for  
1003 global patterns among all pixels.

---

1004 **Offset correction**

1005 The most recent version of the pre-release full-sky IRC data contained an apparent all-sky  
1006 positive offset of  $\sim 2$  MJy/sr for A9 and  $\sim 4$  MJy/sr for A18. We assess this offset first by  
1007 finding the mode of each of the  $\sim 4,700$   $3^\circ \times 3^\circ$  tiles of the IRC survey, and then taking the  
1008 mode of that distribution. We then compare this result with a monopole offset fit to the all-sky  
1009 HEALPix map of the IRC surveys, built from these tiles. Monopole fitting is handled by the  
1010 `healpy.fit_monopole` function. We find the values produced by these two methods to be  
1011 consistent. We found offsets also in the IRAS, FIS, and HFI bands, thus we apply the same  
1012 monopole fitting and subtraction to all of the all-sky maps. We do not find the correlation  
1013 analysis presented in later sections to be sensitive to this offset correction.

1014 

## 4.2 All-sky cross correlations

1015 In order to look more closely at how the AME to IR relationship varies with wavelength, we first  
1016 do a comparison without applying any pixel mask, as a benchmark. Fig. 4.1 shows the pixel-  
1017 density plots of AME vs. the IR bands' intensities. Darker regions show higher pixel densities,  
1018 unshaded or more lightly shaded regions show low or zero pixel densities. An intial analysis,  
1019 considering only the interreations of the PC parameter maps, was presented in Sec. 2.4, wherein  
1020 correlations between the major microwave component maps (synchrotron, free-free, AME, and  
1021 dust emisison) are demonstrated (Fig. 2.8). This section extends that analysis, considering the  
1022 full range of IR maps described in Tab. 2.1.

1023 We see immediately that each band shows evidence of a positive trend with AME intensity.  
1024 For the MIR bands, at lower IR intensities we see the effects of detector noise become dominant,  
1025 turning into a more defined positive trend with increasing IR intensity. This effect is less  
1026 pronounced in the FIR. The trend is similar to that found in Ch. 3, and Fig. 3.7. We consider  
1027 that the IR maps used must not only be compared to the AME, but to each other, to assess  
1028 multi-wavelength patterns. We also compare the AME and IR maps to ancilliary maps, as  
1029 decribed in Ch. 2 and Tab. 2.2. Fig. 4.2 confirms the weaker trend in the MIR vs. AME, via  
1030 a cross-correlation matrix, similar to that used in Ch. 3 and Fig. 3.7. This is reflected in the  
1031 comparison between high and low latitude plots: for pixels  $|\beta| > 15^\circ$ , we see a dramatic effect.  
1032 In the most extreme case  $r_s$  of A18 to  $AME_{var}$  drops from 0.72 at lower latitudes, to 0.02 at

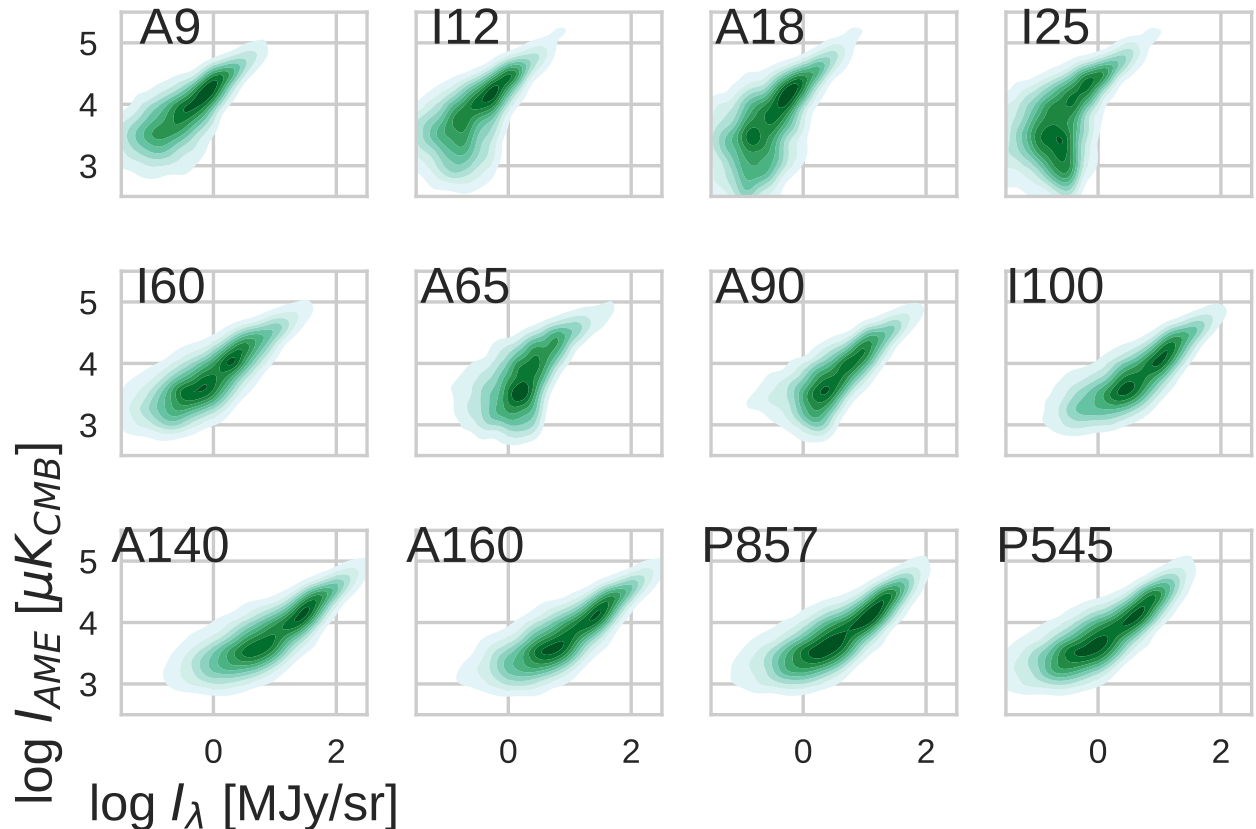


Figure 4.1: Point-density distributions of the  $\log AME_{var}$  intensity (Y-axis) vs.  $\log$  IR bands' intensities. In this case no pixel mask is applied, in order to show overall trend of the full data-set. However a random sampling is used due to computational constraints. The plots show a random set of 20% of the full-sky data. Darker shaded regions indicate a higher density of pixels.

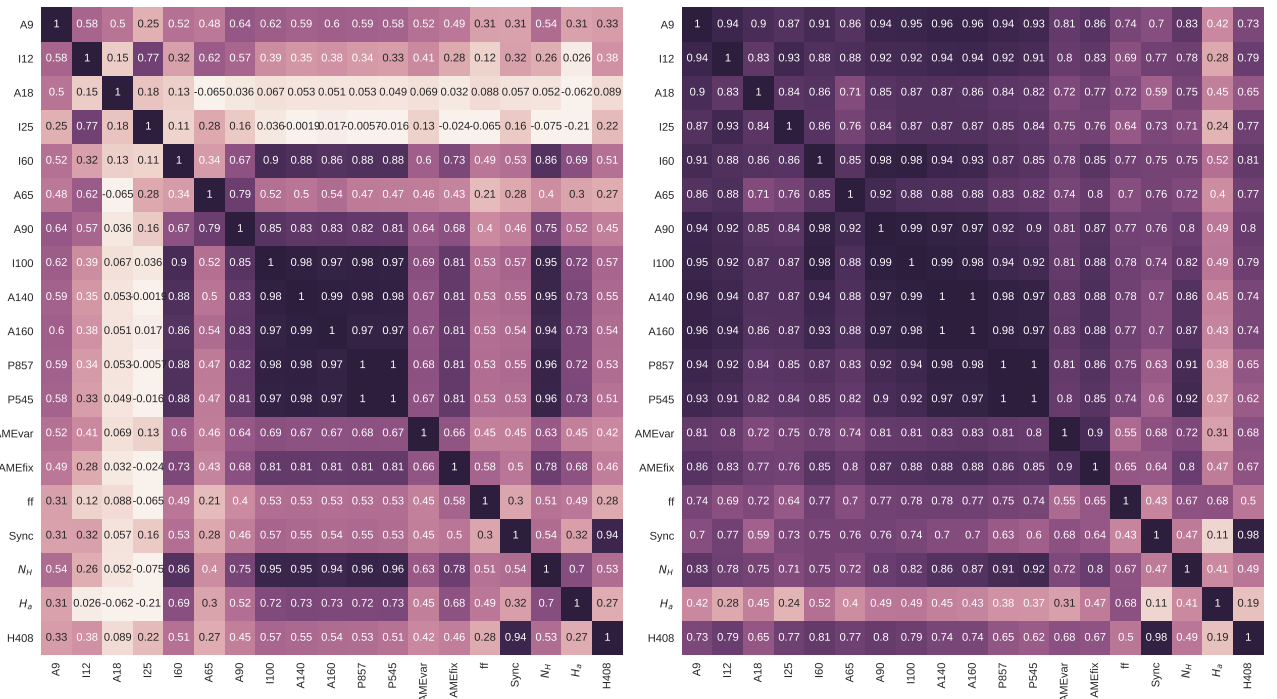


Figure 4.2: ALL-SKY cross-correlation matrix for the 12 infrared bands sampled, as well as the PC component maps described in Ch. 2: the two AME components evaluated at their peak frequencies  $AME_{var}$ ,  $AME_{fix}$ ; Syncrotron, and free-free), and ancillary maps of  $N_H$ ,  $H\alpha$  emission, and 408 MHz emission Haslam et al. (1982). The color-scale indicates ( $r_s$ ). Results are based on the unmasked sky, but are split by Galactic latitude: pixels with  $|\beta| < 15^\circ$  (left) and  $|\beta| > 15^\circ$  (right). The color and annotations indicate  $r_s$  as in Fig. 3.7.

higher latitudes.  $r_s(A9 : AME_{var})$  drops from 0.79 to 0.42. Correlations between the MIR bands and FIR bands also weaken. Only the the interrelations between the FIR bands from I60 to P545 remain essentially latitude independent (with the exception of A65, which has an especially high noise level.)

In the lower latitudes, with  $|\beta| < 15^\circ$ , bright emission in and around the galactic plane seems to homogenize the bands. We see little change from band to band both in terms of the relationship with AME or with other IR bands. Thus the increase of S/N with decreasing brightness at higher latitudes has a strong effect on such intensity correlation tests. Bands tracing bright thermal dust emission at higher latitudes are more robust against this effect. The only case where the trend is reversed, is with the maps of  $N(H)$  and  $H\alpha$ . Both of these maps show higher  $r_s$  when compared to high latitude FIR emission, possibly due to optical effects. The next section describes a pixel-masking strategy designed to mitigate both  $r_s$  suppressing effects from band-to-band S/N variations, and  $r_s$  enhancing effects from confusion near the galactic plane.

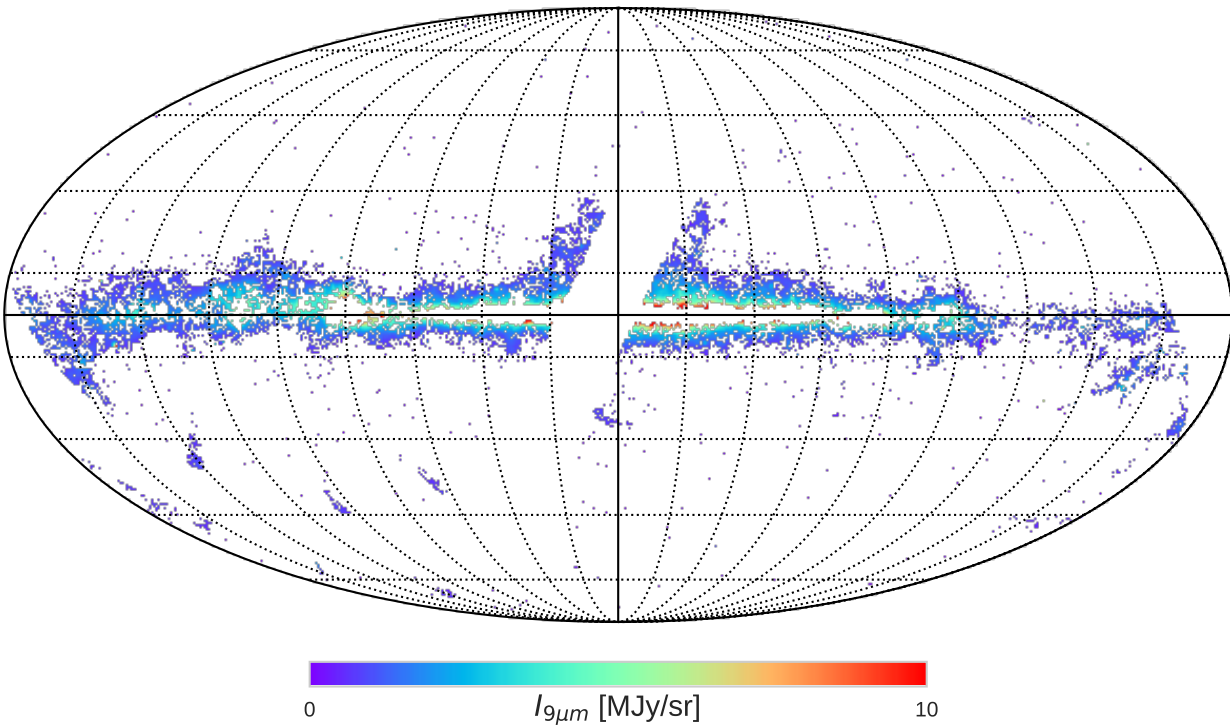


Figure 4.3: All-sky map in A9 emission after applying the combined masks: ecliptic plane, galactic plane, point sources, and pixels with  $S/N < 3$ . This mask essentially outlines the galaxy, except for the most confused regions. Diffuse galactic emission is essentially removed by the mask due to low S/N in the MIR bands. In the full sky map of  $\sim 700,000$  pixels, there are  $\sim 50,000$  unmasked pixels remaining.

## <sup>1047</sup> 4.3 Masked Comparison

<sup>1048</sup> For the reasons described in the previous section, we consider that an exhaustive comparsion of  
<sup>1049</sup> the AME with IR requires the use of a pixel mask. In this section we describe the various masks  
<sup>1050</sup> applied to the full dataset. We then repeat both the comparisons above (as in Figs. 4.1 and 4.2)  
<sup>1051</sup> for the masked dataset, and present additional analyses. The full mask, superimposed on A9  
<sup>1052</sup> map, is shown in Fig. 4.3, with the details of the mask layers described in the next subsection.  
<sup>1053</sup> The mask most heavily affects high galactic latitudes, and the galactic plane. The same mask  
<sup>1054</sup> is applied to all of the maps.

### <sup>1055</sup> 4.3.1 Pixel mask

<sup>1056</sup> **Galactic plane** The galactic plane tends to be a challenge in any comparison, but especially  
<sup>1057</sup> with low resolutions studies such as the present work. Complicated structures along the line  
<sup>1058</sup> of sight, smoothed to  $1^\circ$  resolution, means that emisison within any given pixel is an average

of many different environments (evidenced by the homogenizing of the correlations between bands at low latitudes in Fig. 4.2.) Thus we exclude the brightest emission of the galactic plane, according to the mask prepared by the Planck Collaboration.

**Zodiacal light** To minimize the effects of residual zodiacal light, we exclude pixels within  $10^\circ$  of the ecliptic plane. Even though we use the Zodi-subtracted maps (Kelsall et al. 1998; Kondo et al. 2016; Ootsubo et al. 2016), the Zodi residuals are still problematic (especially in the MIR.) This corresponds to regions with the heaviest contamination from Zodiacal light, where Zodi residuals are apparent even with visual inspection for all of the MIR bands used in this study. In Ch. 2, Figs. 2.6, and 2.6 clearly display these residual patterns.

**Signal to noise** Some of the bands used lack sufficient sensitivity to trace fainter emisison, especially at higher galactic latitudes. This is mainly an issue for the mid-infrared bands. As such, we enforce a  $3\sigma$  threshold for all of the maps— adding to the mask any pixel that has lower than  $3\sigma$  detection in any of the maps. This removes nearly all pixels beyond approximately  $15^\circ$  from the galactic plane, with the pronounced exception of regions affected by stray moonlight. The extent of this particular mask is primarily defined by the IRC A9 and A18 maps, which have the highest noise levels.

**Point Sources** The Planck Collaboration provides masks of the pixels they find to include point sources. We mask pixels which are flagged as being point-source contaminated, in the most heavily affected maps: Planck/HFI 857 GHz and Planck/LFI 30 GHz.

**PC Component Separation Errors** As noted in Planck Collaboration et al. (2016b); Hensley et al. (2016), there are fluctuations in the PC maps wherein AME emission appears to correspond to fluctuations in the synchrotron map. While a mask of all but the most reliably component separated pixels would be ideal, the construction of such a mask with the current data would require us to use a rather artificial threshold. While PC does provide error maps for each of the components, these are not necessarily an indication of how confident the component separation process itself is at a given pixel. We prefer not to apply any additional masks tailored to the PC maps, and instead present and discuss the results with the possibility of component separation artifacts in mind. However we do note that applying the LFI point source mask and galactic plane masks serves also to mask most pixels with AME peak frequency outliers.

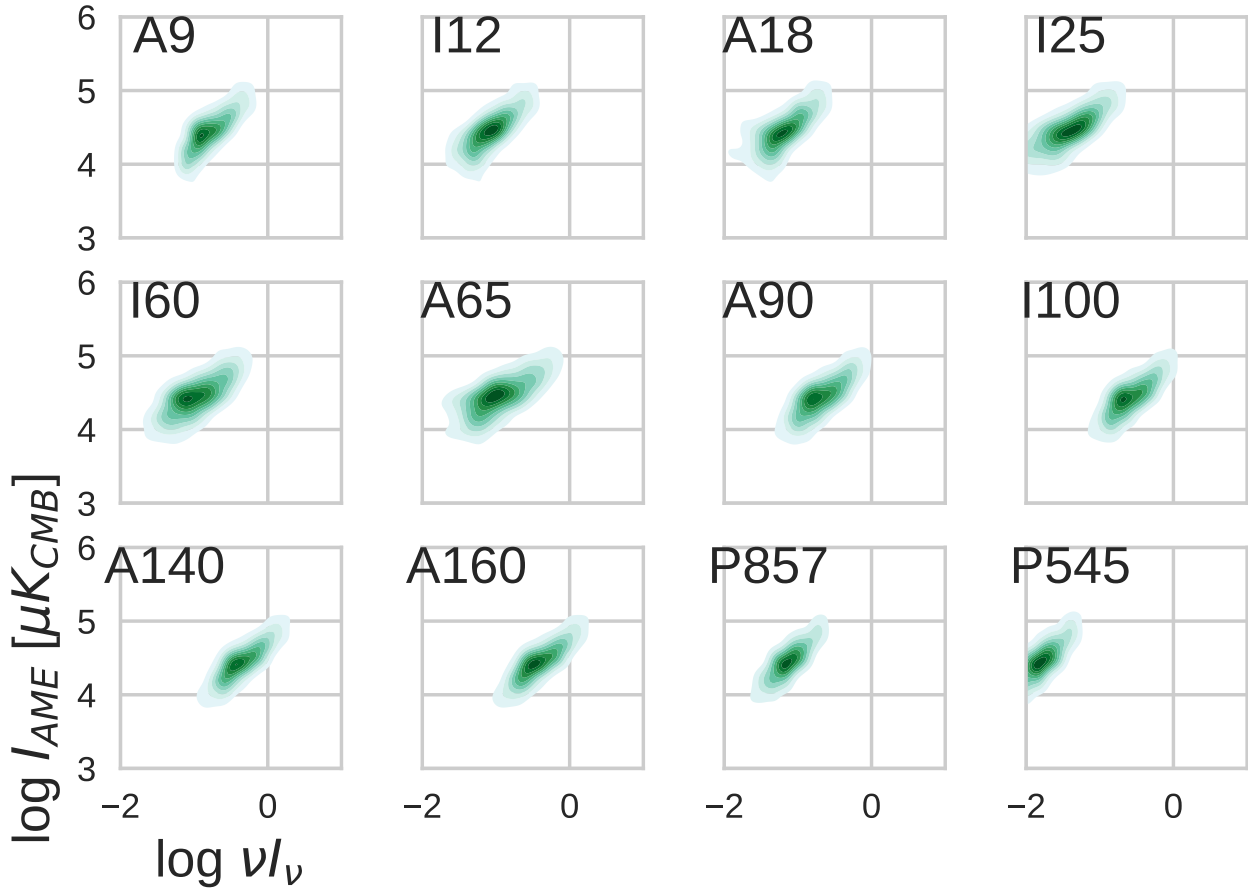


Figure 4.4: The same comparison as shown for Fig. 4.1, but with the mask applied as in Fig. 4.3.

### <sup>1088</sup> 4.3.2 Effect of mask application

<sup>1089</sup> Fig. 4.4 shows point-density plots for  $AME_{var}$  vs. each of the IR bands, after applying the  
<sup>1090</sup> mask described above. This reduces the number of pixels from  $\sim 780,000$  to  $\sim 50,000$ , with  
<sup>1091</sup> about 7% of the sky remaining. As expected with such a drastic reduction of the number of  
<sup>1092</sup> noise-dominated points, the scatter, especially for the MIR bands, is reduced. This can be  
<sup>1093</sup> seen by comparing Fig. 4.4 to the unmasked distributions vs. AME in Fig. 4.1. Otherwise the  
<sup>1094</sup> applicaiton of the mask does not bring about any special distinction among the bands when  
<sup>1095</sup> compared to the AME. What is notable however is that the persistent weakening of trend of  
<sup>1096</sup> I25 vs. AME, relative to A9 and the FIR bands. This is seen also when looking at the full set  
<sup>1097</sup> of interrelations via the cross-correlation matrix in Fig. 4.5.

<sup>1098</sup> **Normalizing by radiation field  $U$**  Following the logic that the PAH-tracing bands inten-  
<sup>1099</sup> sity is essentially a product  $U$  and the column density of PAHs  $\sigma_{PAH}$  (as explained in Ch. 2),  
<sup>1100</sup> we redraw the comparison after scaling the MIR bands by  $U$ . We determine  $U$  by taking the  
<sup>1101</sup>  $1^\circ$ -smoothed, degraded PR1 dust radiance map (also used in (Hensley et al. 2016)), and its

	1	0.91	0.92	0.89	0.86	0.85	0.89	0.91	0.93	0.93	0.87	0.84	0.77	0.83	0.67	0.62	0.71	0.41	0.64
A9	1	0.91	0.92	0.89	0.86	0.85	0.89	0.91	0.93	0.93	0.87	0.84	0.77	0.83	0.67	0.62	0.71	0.41	0.64
I12	0.91	1	0.81	0.95	0.81	0.86	0.85	0.86	0.89	0.9	0.86	0.83	0.76	0.8	0.62	0.69	0.63	0.26	0.71
A18	0.92	0.81	1	0.85	0.82	0.74	0.84	0.85	0.86	0.86	0.8	0.77	0.69	0.76	0.63	0.55	0.69	0.41	0.58
I25	0.89	0.95	0.85	1	0.83	0.81	0.85	0.88	0.9	0.91	0.88	0.85	0.75	0.79	0.61	0.67	0.66	0.25	0.69
I60	0.86	0.81	0.82	0.83	1	0.92	0.99	0.99	0.93	0.92	0.78	0.73	0.73	0.83	0.7	0.75	0.63	0.56	0.79
A65	0.85	0.86	0.74	0.81	0.92	1	0.94	0.92	0.9	0.89	0.77	0.73	0.72	0.81	0.69	0.75	0.58	0.47	0.78
A90	0.89	0.85	0.84	0.85	0.99	0.94	1	1	0.96	0.95	0.83	0.79	0.77	0.86	0.71	0.74	0.66	0.53	0.78
I100	0.91	0.86	0.85	0.88	0.99	0.92	1	1	0.97	0.96	0.85	0.81	0.78	0.87	0.71	0.74	0.68	0.51	0.78
A140	0.93	0.89	0.86	0.9	0.93	0.9	0.96	0.97	1	1	0.93	0.9	0.81	0.89	0.71	0.68	0.76	0.46	0.7
A160	0.93	0.9	0.86	0.91	0.92	0.89	0.95	0.96	1	1	0.94	0.91	0.81	0.88	0.71	0.68	0.76	0.43	0.7
P857	0.87	0.86	0.8	0.88	0.78	0.77	0.83	0.85	0.93	0.94	1	1	0.79	0.84	0.68	0.53	0.85	0.32	0.55
P545	0.84	0.83	0.77	0.85	0.73	0.73	0.79	0.81	0.9	0.91	1	1	0.76	0.82	0.67	0.49	0.87	0.31	0.5
AMEvar	0.77	0.76	0.69	0.75	0.73	0.72	0.77	0.78	0.81	0.81	0.79	0.76	1	0.9	0.45	0.61	0.65	0.3	0.62
AMEfix	0.83	0.8	0.76	0.79	0.83	0.81	0.86	0.87	0.89	0.88	0.84	0.82	0.9	1	0.6	0.59	0.73	0.48	0.62
ff	0.67	0.62	0.63	0.61	0.7	0.69	0.71	0.71	0.71	0.71	0.68	0.67	0.45	0.6	1	0.34	0.58	0.7	0.4
Sync	0.62	0.69	0.55	0.67	0.75	0.75	0.74	0.74	0.68	0.68	0.53	0.49	0.61	0.59	0.34	1	0.33	0.13	0.99
$N_H$	0.71	0.63	0.69	0.66	0.63	0.58	0.66	0.68	0.76	0.76	0.85	0.87	0.65	0.73	0.58	0.33	1	0.4	0.33
$H_a$	0.41	0.26	0.41	0.25	0.56	0.47	0.53	0.51	0.46	0.43	0.32	0.31	0.3	0.48	0.7	0.13	0.4	1	0.2
H408	0.64	0.71	0.58	0.69	0.79	0.78	0.78	0.78	0.7	0.7	0.55	0.5	0.62	0.62	0.4	0.99	0.33	0.2	1
	A9	I12	A18	I25	I60	A65	A90	I100	A140	A160	P857	P545	AMEvar	AMEfix	ff	Sync	$N_H$	$H_a$	H408

Figure 4.5: Cross-correlation ( $r_s$  matrix for the IR intensities (unscaled) vs. each other, essentially the same comparison as in Fig. 4.2, except that the pixel mask is applied, and we do not perform a split by Galactic latitude— after the mask is applied, over 90% of pixels are within  $10^\circ$  of the galactic plane.

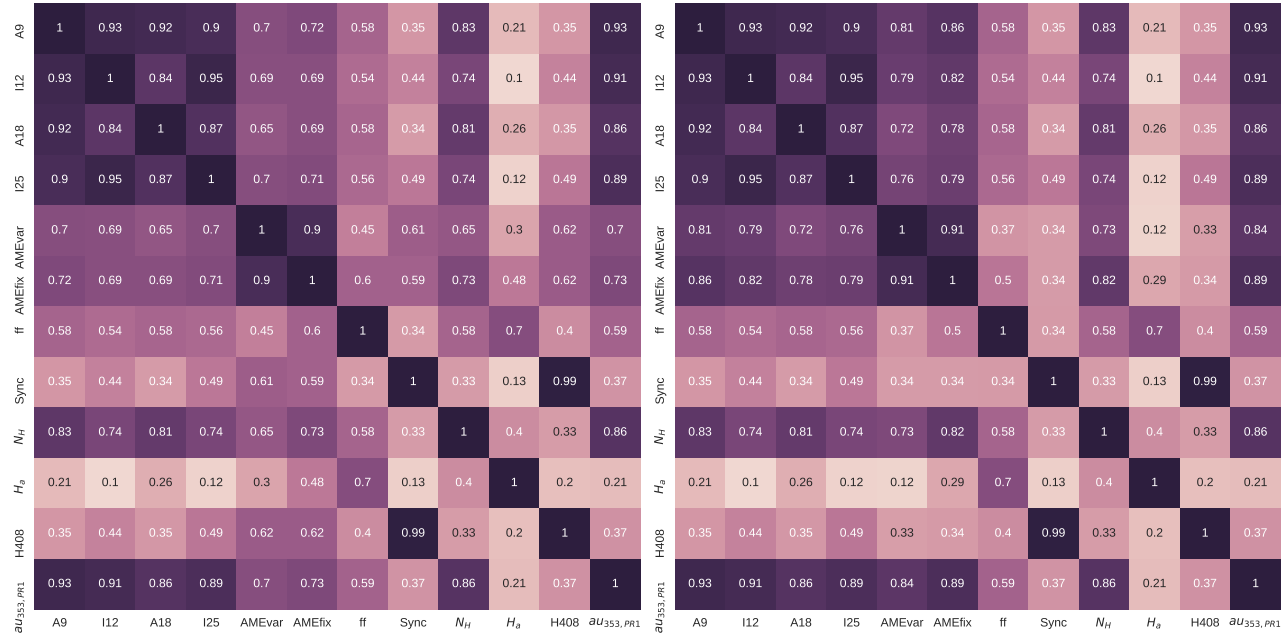


Figure 4.6: Cross-correlation ( $r_s$  matrix for the  $U$ -normalized IR intensities vs. each other, and also against the AME components, other PC products, and ancilliary data. In the left panel, only the IR maps are divided by  $U$ —other data is unchanged from. In the panel at right, both the the AME and IR intensities are divided by  $U$ . Fig. 4.5)

corresponding  $\tau_{353}$  map. We approximate  $U \propto R/\tau_{353}$ . In the case of  $U$ -normalized intensities correlation plots, we only include the MIR bands. While  $I_{MIR}/U$  is thought to trace column density of the band carriers (PAHs, or VSGs), there is a less definite interpretation of  $I_{FIR}/U$  (since the profile of FIR dust emission depends on the dust temperature.) Thus for this particular comparison, we represent the FIR with  $\tau_{353}$ . The  $U$ -normalized correlation matrix is given by Fig 4.6. In this comparison, we see that all of the correlations of the MIR bands vs. AME weaken slightly when we scale the MIR bands by  $U$ . However if we consider that  $U$  may also affect the AME intensity, it may make sense to show a comparison where the MIR bands and AME intensities are all scaled by  $U$ . The result of this is shown on the right panel of Fig. 4.6. Indeed the correlations improve slightly, between  $MIR/U$  and  $AME/U$ . However we cannot rule out a spurious improvement of the correlations, induced by the common division by noise in the parameter  $U$ .

**R-normalized comparison** For completeness we perform a comparison similar to that provided in Hensley et al. (2016), wherein they compared the ratio  $I_{AME}/R$  (a sum of  $AME_{var}$  and  $AME_{fix}$ ) to the fraction of dust in PAHs,  $fPAH$ . In our analysis, the ratios of  $A9/R$  and  $I12/R$ , considering that A9 and I12 are dominated by PAH emission, would be comparable to the Hensley et al. (2016) parameter of  $fPAH$ . As with the result in Hensley et al. (2016),

A9	1	0.58	0.68	0.41	0.16	0.21	0.097	-0.0044
I12	0.58	1	0.37	0.71	0.14	0.08	0.053	0.089
A18	0.68	0.37	1	0.44	0.072	0.13	0.13	-0.13
I25	0.41	0.71	0.44	1	0.057	0.012	0.074	-0.14
AMEvar	0.16	0.14	0.072	0.057	1	0.66	-0.32	0.15
AMEfix	0.21	0.08	0.13	0.012	0.66	1	-0.1	0.02
ff	0.097	0.053	0.13	0.074	-0.32	-0.1	1	-0.4
Sync	-0.0044	0.089	-0.13	-0.14	0.15	0.02	-0.4	1
	A9	I12	A18	I25	AMEvar	AMEfix	ff	Sync

Figure 4.7: Cross-correlation ( $r_s$ ) matrix for the residual correlations between IR intensities, AME, and other microwave components. All of the maps in this case are normalized by  $R$ . )

these data do not reveal any correlation between PAH fraction and  $I_{AME}/R$ , or with any of the MIR/R ratios and  $I_{AME}/R$ . Interestingly, there is evidence of a marginal positive trend with synchrotron, and a negative trend with free-free emission.

**Bootstrap test** In addition, for the masked comparison, we carry out a bootstrap analysis, using the same method explained in Ch. 3. The Spearman rank correlation coefficients  $r_S$  of all of the bands, in intensity, vs. the  $AME_{var}$  component are shown. This is done only for the masked case, due to the computational challenges presented by a well-sampled bootstrap of all  $\sim 780,000$  pixels in the full sky. Because the mask applied here leaves us with approximately 7% of the sky, a bootstrap with  $N_{iterations} > N_{pix}$  becomes tractable. We show the comparison only for the  $AME_{var}$  component also due to computational constraints. The  $r_s$  distributions for each IR band vs. AME are shown in Fig. 4.8. The calculations are performed in the same way as with Fig. 3.8 for  $\lambda$  Orionis. Consistent with the other correlation analyses already shown in this chapter, there is a stronger correlation in the FIR, especially A160. Considering the MIR range, and as with  $\lambda$  Orionis, A9 emission correlates better than I12. The worst correlation is seen with the A18 and I25 bands.

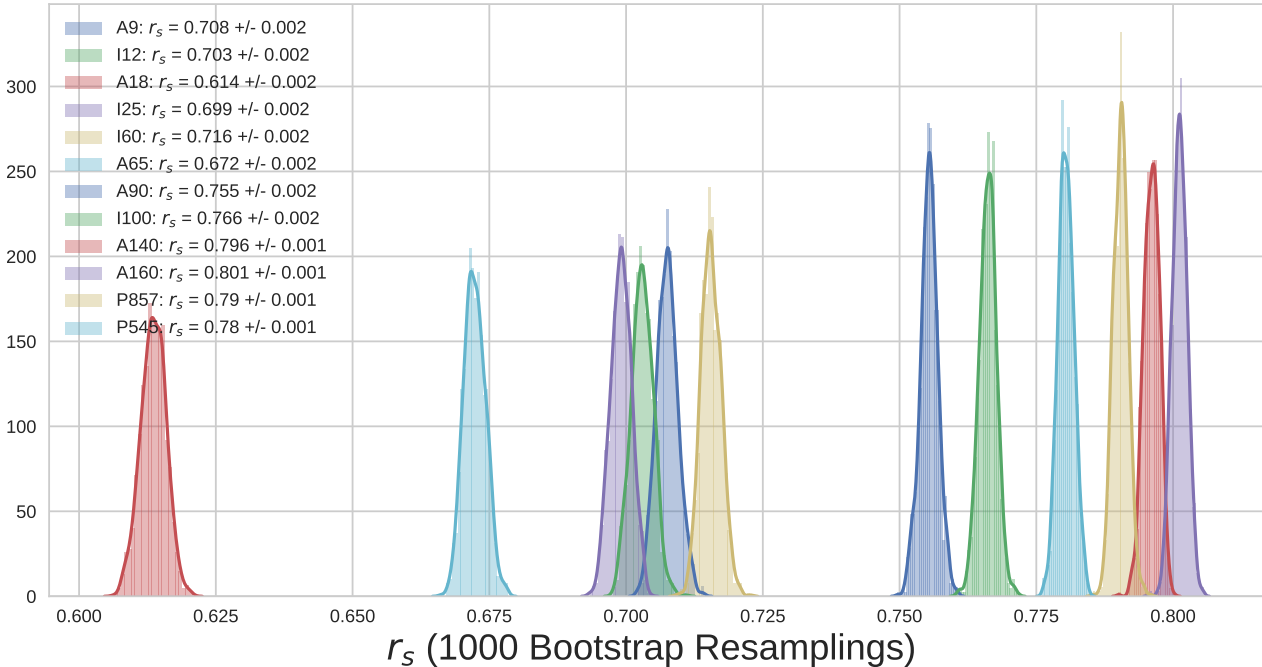


Figure 4.8: Re-sampled (Bootstrap) correlation tests for IR emission vs. AME, performed on the masked all-sky maps. Each band's  $r_s$  distribution is shown in a different color. The width of the distribution indicates the error for the given data in the correlation coefficient. The mean and standard deviation of the scores are given in the legend of each plot. The plot ranges only show positive values, since no negative scores were produced.

## <sup>1134</sup> 4.4 Spatial variation of correlations

<sup>1135</sup> To understand how these trends may vary across the sky, independent from the choice of pixel  
<sup>1136</sup> masl, we produce an all-sky maps of  $r_s$  for AME vs. IR emission. From the NSIDE 256 input  
<sup>1137</sup> maps of AME and 4 IR wavelength maps, we produce NSIDE 8 maps of  $r_s$ . These maps are  
<sup>1138</sup> shown in Figs. 4.9-4.12. The most important feature of these maps is that they look very similar,  
<sup>1139</sup> confirming in a spatial context that there is very little difference overall, when comparing AME  
<sup>1140</sup> to IR in intensity, accross multiple wavelengths. The correlations weaken for the MIR bands  
<sup>1141</sup> at higher latitudes, as expected. Thus the question of which band correlates better depends on  
<sup>1142</sup> exactly where we look. Considering that we need also to look at secondary correlations, not  
<sup>1143</sup> only in intensity, we repeat the above process for ratios of the MIR to AME, scaling both by  $U$ ,  
<sup>1144</sup> as in Fig. 4.6. Figs. 4.13-4.16 show such correlation maps. Scaling by  $U$  does not change the  
<sup>1145</sup> overall structure of these correlation maps, relative to the unscaled versions. This may indicate  
<sup>1146</sup> that at the scale of these correlation maps, the strength of  $U$  does not show much variation.

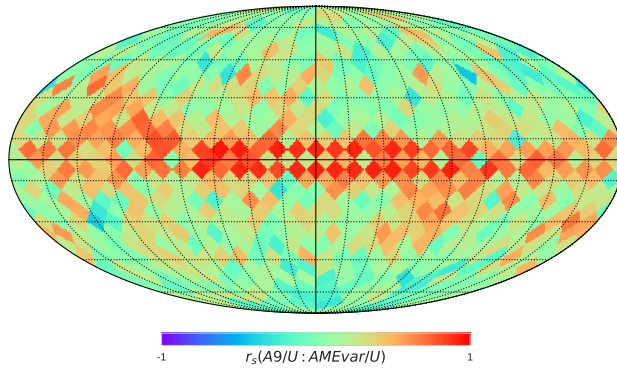


Figure 4.9: Spatial map of  $r_s$  between the AME and IR intensity for A9.  $r_s$  is calculated for all NSIDE 256 pixels within each NSIDE 8 pixel-sized bin. The correlation score is calculated with the unmasked maps. The colorbar indicates  $r_s$ , ranging from -1 (negative monotonic relationship) to +1 (positive monotonic relationship).

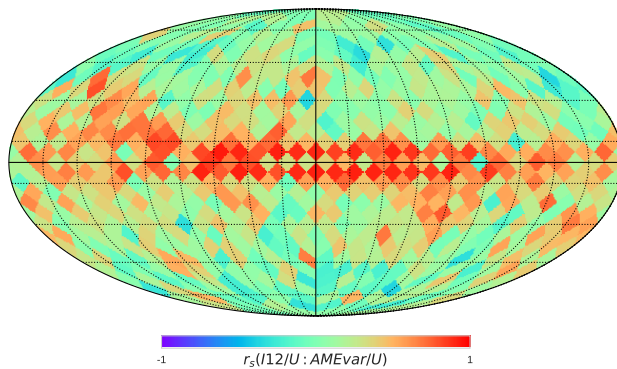


Figure 4.10: Spatial map of  $r_s$  between the AME and IR intensity for I12, calculated as in Fig. 4.9.

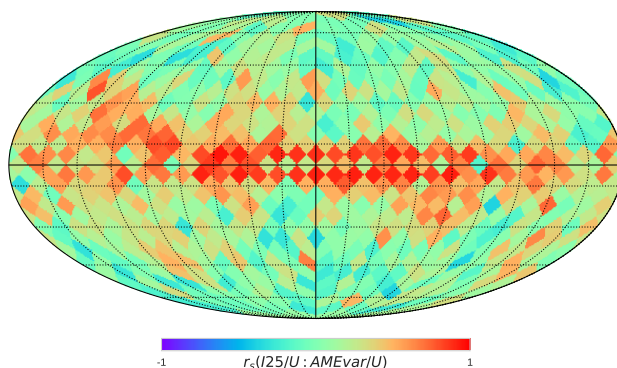


Figure 4.11: Spatial map of  $r_s$  between the AME and IR intensity for I25, calculated as in Fig. 4.9.

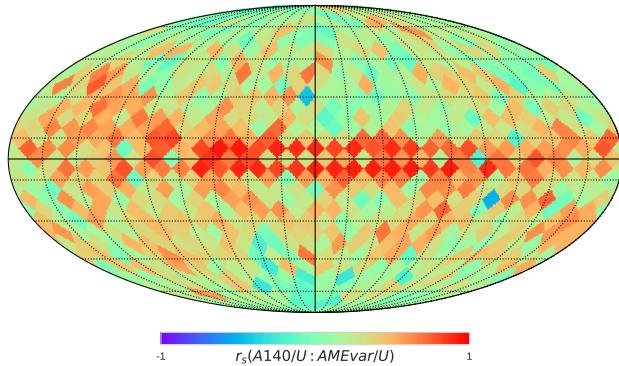


Figure 4.12: Spatial map of  $r_s$  between the AME and IR intensity for A140, calculated as in Fig. 4.9.

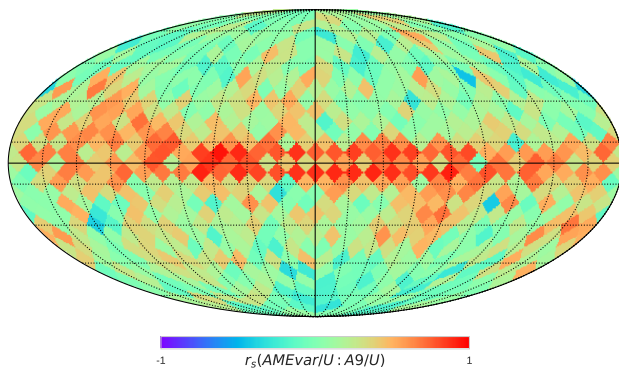


Figure 4.13: Spatial map of  $r_s$  between the AME:U and A9:U, a tracer of the column density of PAHs emitting within the A9 filter. The correlations are calculated as in Fig. 4.9.

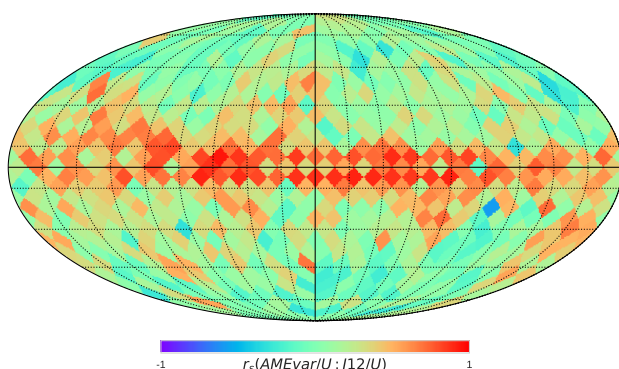


Figure 4.14: Spatial map of  $r_s$  between the AME:U and I12:U

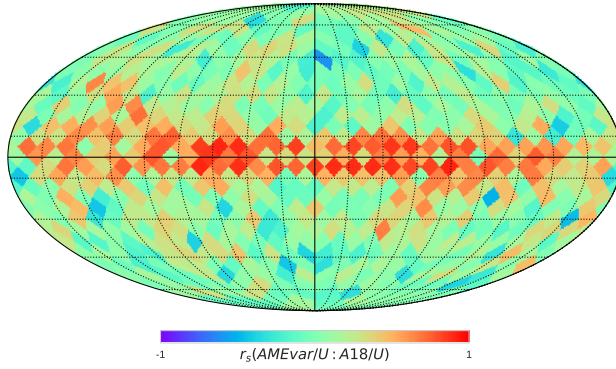


Figure 4.15: Spatial map of  $r_s$  between the AME:U and A18:U

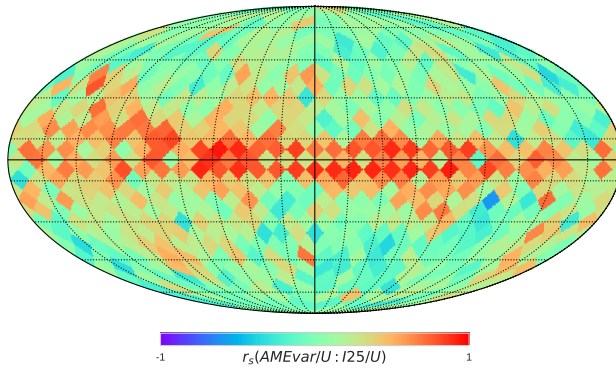


Figure 4.16: Spatial map of  $r_s$  between the AME:U and I25:U

## <sup>1147</sup> 4.5 Discussion

<sup>1148</sup> As noted in Ch. 1, previous studies found that the AME generally correlates at dust-related  
<sup>1149</sup> IR wavelengths (Ysard et al. 2010; Planck Collaboration et al. 2014d; Hensley et al. 2016).  
<sup>1150</sup> We see the same overall pattern in the present study. We also corroborate that the FIR  
<sup>1151</sup> emission shows the tightest correlation with the AME intensity, for large portion of the sky  
<sup>1152</sup> in a de-localized fashion (Figs. 4.2 and 4.5). In testing for a second-order correlation, we  
<sup>1153</sup> divided the IR intensities and AME intensity by  $U$ , and again performed the band-by-band  
<sup>1154</sup> all-sky comparison. There is evidence of a residual correlation between  $I_{MIR}/U$  and  $I_{AME}/U$   
<sup>1155</sup> (Figs. 4.6, and 4.13-4.16).

<sup>1156</sup> The closeness of the correlation coefficients found here is consistent with the results of the  
<sup>1157</sup> IRAS vs. AME correlation test result from Planck Collaboration et al. (2014d). They found  
<sup>1158</sup> that the correlation coefficient among the four IRAS bands (12, 25, 60, and 100  $\mu\text{m}$ ) differ from  
<sup>1159</sup> one another only by about 5%, across their whole set of 98 regions. They had also indicated  
<sup>1160</sup> that many of the regions sampled were HII regions, and that free-free emission may not have

been completely separated from the AME. We consider that a similar phenomenon may be happening in the PCAME map we explore here. The trend of AKARI MIR and FIR data vs. the AME does not disagree with their IRAS comparison. This work adds that individual band intensities longer than IRAS 100  $\mu$ m also correlate strongly with AME, especially the two Planck/HFI bands used.

#### 4.5.1 AME and interstellar radiation fields

In our masked analysis, we were unable to replicate with the PC data a result by Ysard et al. (2010) wherein scaling the MIR bands by  $U$  improves the correlation of MIR vs. AME. Instead we found that the best correlation between the MIR bands and AME is found after scaling both by  $U$ . There is a chance that this improvement is induced by the common division of noise-terms in  $U$ , but if this correlation increase is real it may indicate that the AME intensity is somewhat dependent on  $U$ . While it is expected that AME intensity depends both on the abundance of carriers, and various excitation terms, it is not predicted that  $U$  directly influences spinning dust excitation. However it may be an indirect tracer of galactic environments and various other spinning dust excitation factors. The slight improvement with division by  $U$  was also seen with our investigation of  $\lambda$  Orionis in Ch. 3.

According to spinning dust theory outlined in Draine & Lazarian (1998a) and in subsequent works by Ysard & Verstraete (2010), the AME profile and intensity will depend in part on the ISRF- but as is well-stated in Hensley & Draine (2017), exactly how the ISRF will affect the AME SED is a more complicated question. Absorbed starlight photons may be able to rotationally excite the carriers, but if an enhanced ISRF leads to increased dust heating, then the increased IR emission can rotationally de-excite the carriers. Moreover the ISRF affects not only the dust temperature but ionization of the carriers.

#### 4.5.2 Microwave foreground component separation

There are known degeneracies between the foreground parameters of the COMMANDER maps (spinning-dust, and free-free, synchrotron components as described in Planck Collaboration et al. (2016b).) This can be demonstrated by examining the ratio map of the AME intensity to  $R$ , in comparison with the PC free-free and synchrotron maps. Figs. 4.17 and 4.18 show the  $AME_{var}/R$  and  $AME_{fix}/R$  ratio maps, with contours from the free-free and synchrotron maps.

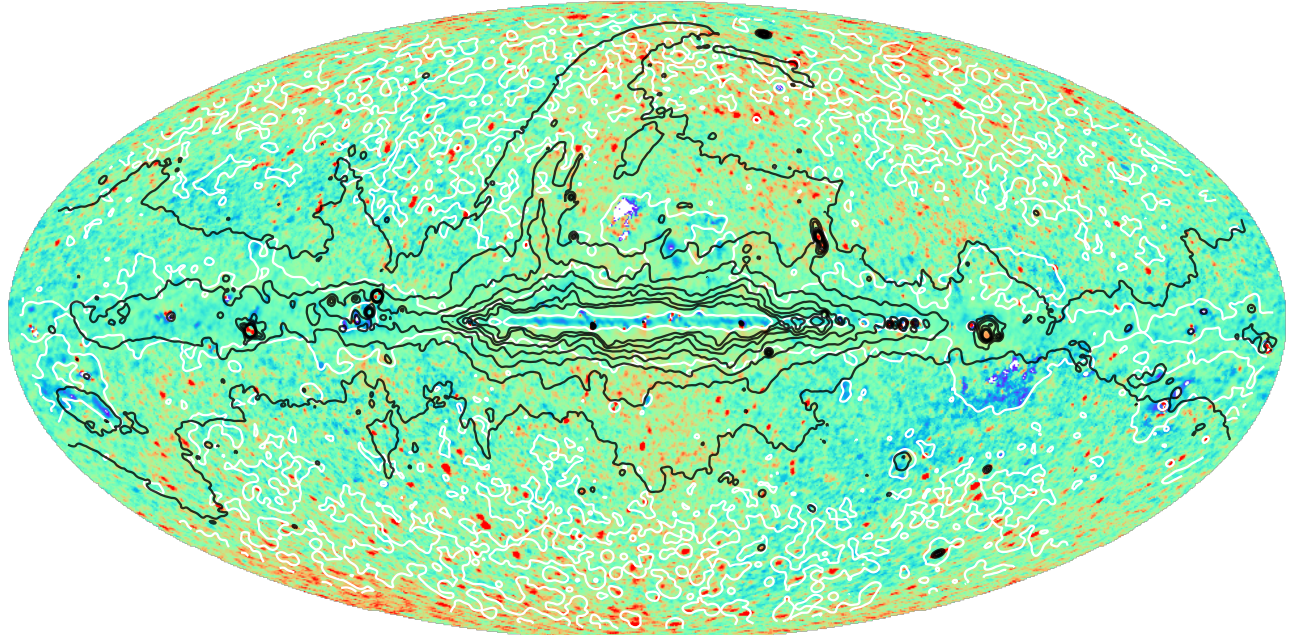


Figure 4.17: The ratio of  $AME_{var}$  and PC dust radiance  $R$ , tracing fluctuations in AME per thermal dust emission. The contours trace the PC synchrotron (black) and free-free (white) components, to highlight various correlations between these components and PC AME fluctuations. Both free-free and synchrotron can be seen to correlate and anti-correlate with the AME to dust ratio.

1190 There are clearly regions where synchrotron emission correlates with AME excesses. Some of  
 1191 these appear as more large scale fluctuations, mainly at higher galactic latitude. Interestingly,  
 1192 free-free shows agreement with both positive and negative fluctuations in both ratio maps.  
 1193 At high galactic latitude, free-free tends to be associated with positive fluctuations. This is  
 1194 supported by the fact that  $AME_{fix}$  shows an improved correlation with both the  $H\alpha$  map  
 1195 and the PC free-free map, perhaps suggesting confusion between spinning dust and free-free  
 1196 components. Interestingly, the ring-structure of the  $\lambda$  Orionis region analyzed in Ch. 3, does  
 1197 not have any apparent counterpart in the  $AME/R$  ratio maps in Figs. 4.18 and 4.17.

1198 The results of the  $R$  normalized cross-correlation test show that free-free/R shows a negative  
 1199 correlation with  $AME/R$ . This may be further indication that the AME map, even with the  
 1200 mask applied from Sec.4.3.1, may suffer from significant MW component confusion in some  
 1201 regions. It is difficult to quantify potential effects from component separation uncertainties  
 1202 relative to genuine correlations between microwave emission components, with the present  
 1203 data. However there remains the potential for such confusion to suppress evidence of any trend  
 1204 between AME and the actual value of  $fPAH$ . The anti-correlation here between free-free/R  
 1205 and AME/R may be consistent with findings in von Hausegger & Liu (2015) that free-free

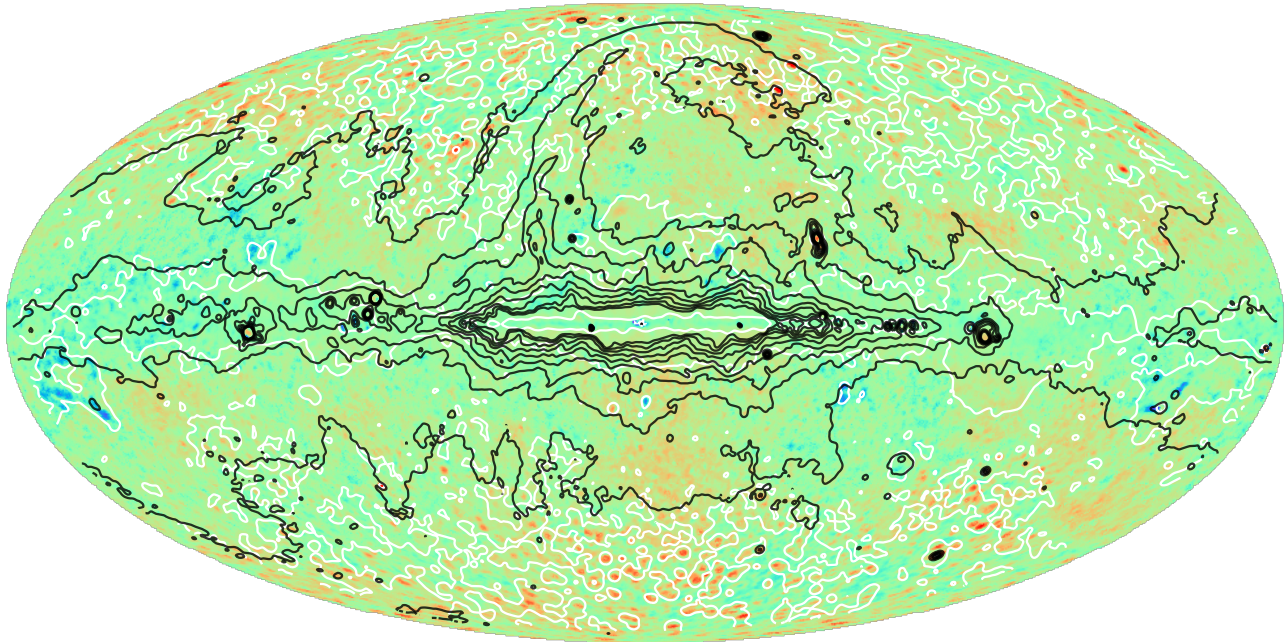


Figure 4.18: The same as Fig. 4.17, but with  $AME_{fix}/R$  as the all-sky image.

1206 emission anti-correlates with AME, if pixels are weighted by S/N.

1207 Even though A9/R and I12/R do not correlate with AME/R in our masked comparison, we  
1208 do find some limited regions where these values correlate in our full spatial correlation mapping.

### 1209 4.5.3 Optical depth

1210 In the interpretation of results here, we have essentially operated under the assumption that  
1211 MIR/PAH emisison, FIR emission, and the AME are all in the optically thin domain. This  
1212 is supported by the strong agreement in  $r_s$ , accross all IR bands and the AME, as presented  
1213 in the correlation matrices here. (With the exception of the high-latitude, unmasked case in  
1214 Fig 4.2.) Conversely, the  $H\alpha$  data — emission known to be absorbed by interstellar dust —  
1215 is the only map lacking a correlation with the others at  $|\beta| < 5^\circ$ .  $N(H)$  also shows a weaker  
1216 correlation nearer to the galactic plane, likely influenced by saturation and/or self-absorption  
1217 effects.

1218 However it has been demonstrated by Sakon et al. (2004) that the optically-thin assumption  
1219 for PAH/UIR emission could lead to errors in the esimate of PAH abundance based on these  
1220 emision features. Self-absorption for PAHs is another possibility.

1221 We do not expect the analysis presented here to suffer from such effects significantly, as we  
1222 have masked the most confused lines of sight towards the galactic plane. However we cannot

rule out the possibility that such optical depth effects, not only in PAH emisison but in the FIR or even AME, may weaken any potential relationship between the IR and microwave emisison from spinning grains.

#### 4.5.4 Comparison of $\lambda$ Orionis vs. All-sky results

Results presented here do not necessarily conflict with results from Ch. 3, except in that the findings from Fig. 3.8, wherein  $r_p$  of A9 emission correlates better with AME than P545 emission, do not generalize to the results of this chapter (either the masked or unmasked cases.) However, in the masked all-sky comparison as well as in  $\lambda$  Orionis, we find a better correlation between A9 and AME than between I12 and AME when we subject the correlations to bootstrap resampling.

The different results between Ch. 3 and Ch. 4 may be explained by variations in the component separation reliability. It is apparent that with the presently available data, there are a very limited number of regions on the sky which do not show strong free-free or synchrotron emission (relative to AME), while also having enough S/N in the MIR to reliably probe a relationship between PAH abundance fluctuations and AME fluctuations.  $\lambda$  Orionis may be one of the exceptions, where the S/N is high enough, and we are in fact able to see an improved correlation between PAHs and AME, relative to the overall dust emission to AME connection.

We also disucssed in Ch. 4 the possibility that the PAH emission may not necessarily be optically thin. If this were true, it may explain discrepancies for our  $\lambda$  Orionis result and the results in this chapter.  $\lambda$  Orionis provides us a relatively clean line of sight compared to delocalized all-sky analysis.

The fact that we do not see a clear preferential relationship between AME and PAHs in the all-sky analysis, does not rule out a contribution by spinning PAHs to the AME. Likewise the fact that we do see a better correlation in  $\lambda$  Orionis does not rule out contributions from other proposals, such as that form non-PAH small grains, or nanosilicates.

#### 4.5.5 Implications of an absent PAH-AME correlation

In the case that we are able to rule PAHs out as the AME carrier with confidence, this may imply some constraints on the PAH size distribution and dipole moment. As discussed in the theoretical work by Draine & Lazarian (1998a); Ali-Haimoud (2010) and others, as well as the

observational work by Hensley et al. (2016), if PAHs exist in the ISM, they are very likely to be spinning rapidly. Thus if we are able to confirm that they do not produce AME, this could tell us the morphology of ISM PAHs are not in an appropriate range to produce the observed AME. Spinning PAHs may be a reality even in the case that the AME comes from something else, if the PAHs are too large or lack appropriate electric dipoles.

## 4.6 Future Works

Because of the issues highlighted in previous sections (S/N, component separation, etc.), it is extremely difficult to draw a conclusion about the carrier of AME based on a general all-sky analysis such as that shown here. However there may be promise in studies of individual regions, where an attempt can be made at controlling for local environmental factors, or background/-foreground contamination. While it is true that previous studies of specific objects have also not been conclusive, such as the investigation of Perseus by Tibbs et al. (2011), there are still many other AME prominent regions which have not been probed in-depth, through a combination of microwave and PAH-range observations. Even the study of  $\lambda$  Orionis in Ch. 3 is not exhaustive, and this interesting region deserves further attention from targeted observations.

New tests of AME hypotheses should: push limitations in the available data and, focus on regions well-documented to show a spinning-dust-like AME spectrum. While a simple excess of microwave emission may be able to be fit by a spinning dust model SED, the spinning dust explanation is not testable unless the observed SED shows evidence of a low-frequency downturn.

There are two major boundaries that, based on results presented here, must be pushed. Spatial resolution and spectral coverage. Spatial resolution constraints are a critical issue in multiwavelength astornomy, especially in dust-related works. To explain why, simply consider the description of dust research from Ch. 1, and Tab. 2.1. The spatial resolution of available data has a wide discrepancy from the MIR to microwave: 10 arcseconds for AKARI 9 micron to at least a degree FWHM for the “effective resolution” of parameter maps. Likewise, if there are environmental diffrences only visible at sub-degree angular scales, we will have a hard time controlling for the excitation factors of spinning dust emission. Without separating excitation factors from column density of the carriers. Pairing opportunities for resolution maximizing

1281 ground-based observations of very limited regions of the sky, utilizing facilities such as the  
1282 Atacama Large Milimeter Array (ALMA) Band 1 (30-35 GHz, still in production, Huang et al.  
1283 (2016).), with detailed assesment of tracers of small dust grains, will be helpful.

1284 Future breakthroughs in the AME may be seen if we are able to increase the number of  
1285 regions with a reliable AME estimation. This can be obtained through improved synchrotron  
1286 emission constraints, at higher resolutions. C-Band All Sky Survey (CBASS) at 5 GHz will  
1287 be helpful in this regard (Irfan et al. 2015). C-BASS is expected to provide higher resolution  
1288 low frequency constraints for the whole sky ( $48'$  compared to  $56'$  for  $H408$ ), with improved  
1289 sensitivity ( $0.1 \mu\text{K}$ ). In terms of localized studies, it may be fruitful to consider the physical  
1290 environment of each region (i.e. ionization state, gas temperature and density, other conditions  
1291 indicated in Draine & Lazarian (1998a); Ali-Haimoud (2010) to affect the SED shape) rather  
1292 than relying of frequency-shifts to a template spectrum. More detailed exploration of PAH  
1293 ionization, and other fluctuations between individual PAH features relative to variations in the  
1294 AME spectral profile may also help us understand potential roles of PAHs in producing AME.  
1295 However, even if we have excellent constraints on PAH emission features, synchrotron emission,  
1296 free-free emission, and a powerful spinning dust SED model, the key data will be spectral  
1297 coverage of the full AME profile. As noted in Ch. 2, the all-sky maps currently available, do  
1298 not give constraints in the 10-20 GHz range. This means that lower frequency spinning dust  
1299 peaks and emissivities are not well known. Improved understanding of AME and spinning dust  
1300 therefore will require observations such as those being undertaken by the Q-U-I JOint Tenerife  
1301 Experiment (QUIJOTE) project, which offers coverage between 10 and 20 GHz (Génova-Santos  
1302 et al. 2015).

# <sup>1303</sup> Chapter 5

## <sup>1304</sup> Summary

<sup>1305</sup> In Ch. 1 we demonstrated both the mysteries and potential for answers revealed by all-sky  
<sup>1306</sup> observation and analysis. A particular mystery, that of the Anomalous Microwave Emission  
<sup>1307</sup> (AME), and the popular but yet unproven hypothesis that this AME comes from rapidly  
<sup>1308</sup> spinning tiny dust grains, perhaps PAHs, was introduced. We explained the merit of testing  
<sup>1309</sup> a spinning PAH hypothesis, while noting that spinning nanosilicates, or even magnetic dipole  
<sup>1310</sup> emission from dust have also been put forth in the literature.

<sup>1311</sup> In Ch. 2, we overviewed a collection of infrared all-sky surveys that help us probe the dust  
<sup>1312</sup> SED from the UIR band range to the FIR, and discussed how these could help explore the  
<sup>1313</sup> AME question. We described also complimentary data and parameter maps from the Planck  
<sup>1314</sup> Collaboration that can be compared with the IR maps. Particular advantages of the PAH  
<sup>1315</sup> tracing bands, especially the A9 band, for covering not only neutral but potentially charged  
<sup>1316</sup> PAHs, were discussed in the context of AME investigation. Limitations were given for all of  
<sup>1317</sup> these data sets— most of these boiling-down to component separation either of the Zodical  
<sup>1318</sup> light from thermal dust emission, or to the latter from other microwave foregrounds and the  
<sup>1319</sup> CMB.

<sup>1320</sup> In Ch. 3 we combined and processed the data presented in Ch 2 to investigate a particular  
<sup>1321</sup> region of the sky with relatively high S/N in all of the data, and demonstrating strong AME. We  
<sup>1322</sup> evaluated the background, noise, and contamination from systematic errors and point sources  
<sup>1323</sup> in these data, and compared them on a common resolution and grid. All of the analyses from  
<sup>1324</sup> simple correlation plots, to bootstrap analysis, to dust SED fitting suggest that A9 emisison  
<sup>1325</sup> correlates with AME better than I12 or D12 — supporting PAH emisison as the source of  
<sup>1326</sup> AME, and suggesting the role of charged PAHs should be further explored. In addition we

---

1327 find that the bands near the thermal dust emisison peak show a weaker correlation, perhaps  
1328 suggesting that harsh radiation fields may be destroying PAHs, leading to weaker AME. We  
1329 also cautioned that although PAH mass correlates better than dust mass, we still see a good  
1330 correlation between FIR emisison and AME (P545, P857). This highlights the fact that AME,  
1331 PAHs, and cold dust are all correlated.

1332 In Ch. 4 we attempted to find evidence that the result from Ch. 2 applies even when looking  
1333 at a less region-specific scale, using an all-sky analysis. However neither the full-sky unmasked  
1334 case, or the case employing a mask of low S/N regions (mainly high galactic latitudes), point  
1335 sources, and the galactic plane, showed a stronger correlation between PAH related emission  
1336 and AME than that seen between FIR emission and the AME. We did however find that as  
1337 in Ch. 3, A9 tends to correlate with AME better than I12 or D12. We discussed apparent  
1338 systemic issues with the AME data, such as the possibility for under or over subtraction of  
1339 free-free or synchrotron emission, and how these could serve to weaken evidence of any PAH  
1340 or small grain correlation wiht the AME. Scaling the infrared intensities by  $U$  does not change  
1341 this result. We reproduce the result from Hensley et al. (2016) that there is not an overall  
1342 correlation between PAH fraction and AME-per-dust-emisison, but expand this calculation  
1343 showing that for a few limited regions on the sky there may be evidence of a correlation. We  
1344 discuss how a potential variation on the optical thickness between UIR bands, FIR emisison,  
1345 among other factors, could lead to a different result between  $\lambda$  Orionis and the all-sky analysis.  
1346 We also discuss potential observational advances that could help explore the issue further, such as  
1347 improved low frequency constraints,or detailed analysis of the spatial variation of PAH features  
1348 paired with high resolution AME observation.

1349 Overall, using the presently available data, it is difficult to isolate the PAH-dust relationship,  
1350 from the dust-AME relationship. We find throughout this work that a PAH-emission to AME  
1351 correlation is readily demonstable, in intensity. A test of whether a second-order relationship  
1352 exists, such that PAH emission is a better predictor of the AME than thermal dust emission,  
1353 was shown to be inconclusive. One exception is that of  $\lambda$  Orionis, where our results suggest  
1354 that PAH mass correlates better with AME than does the total dust mass. Nevertheless we  
1355 emphasize this point cautiously. We were not able to generalize it to a larger scale (all-sky data  
1356 with, effectively, a mask on the galactic plane and high latitude emission.) We are not able to  
1357 confirm or reject a “spinning PAH” hypothesis for the source of AME. However in  $\lambda$  Orionis,

<sub>1358</sub> and perhaps other regions yet to be examined in with dust SED fitting, we suggest that there  
<sub>1359</sub> is still ample reason to continue testing this hypothesis.

# 1360 A Note on Data Dimensionality

1361 While we aim to demonstrate the application of high dimensionality in these studies, we do not  
1362 wish to mislead readers that we have assembled a 12-dimensional photometric dataset, simply  
1363 because we have 12 wavebands. This statement may seem nonsensical at first, but makes sense  
1364 when we consider the covariance of the data. Just from the outside, and our faithful belief  
1365 that FIR dust emission looks something like a blackbody, or modified blackbody, or at the very  
1366 least we can agree that emission from dust in thermal equilibrium would produce some sort of  
1367 peaked continuum emission spanning multiple photometric bands' width. If we agree on this  
1368 point, then it follows naturally that said bands would be highly correlated with one another.  
1369 This means that the number of truly independent data dimensions is not only lower than the  
1370 number of bands used here, it is much lower.

1371 Fig. 1 shows the % of variance in the data retained by the first  $n$  principal components.  
1372 Principal components are found essentially by first finding the covariance matrix of the input  
1373 data, and then diagonalizing this matrix- the eigenvectors will be the basis vectors of each prin-  
1374 cipal component. The eigenvalues will give the explained covariance per component. Applied in  
1375 this manner, the components may not necessarily have a clear physical interpretation, but from  
1376 a data analytics perspective we can at least assess the redundancies in our data. Thus from  
1377 Fig. 1, and choosing an arbitrary covariance "acceptable loss" of 99%, our photometric data  
1378 set steeply reduces to 3 dimensions. The first component contains 98% of the total variance.

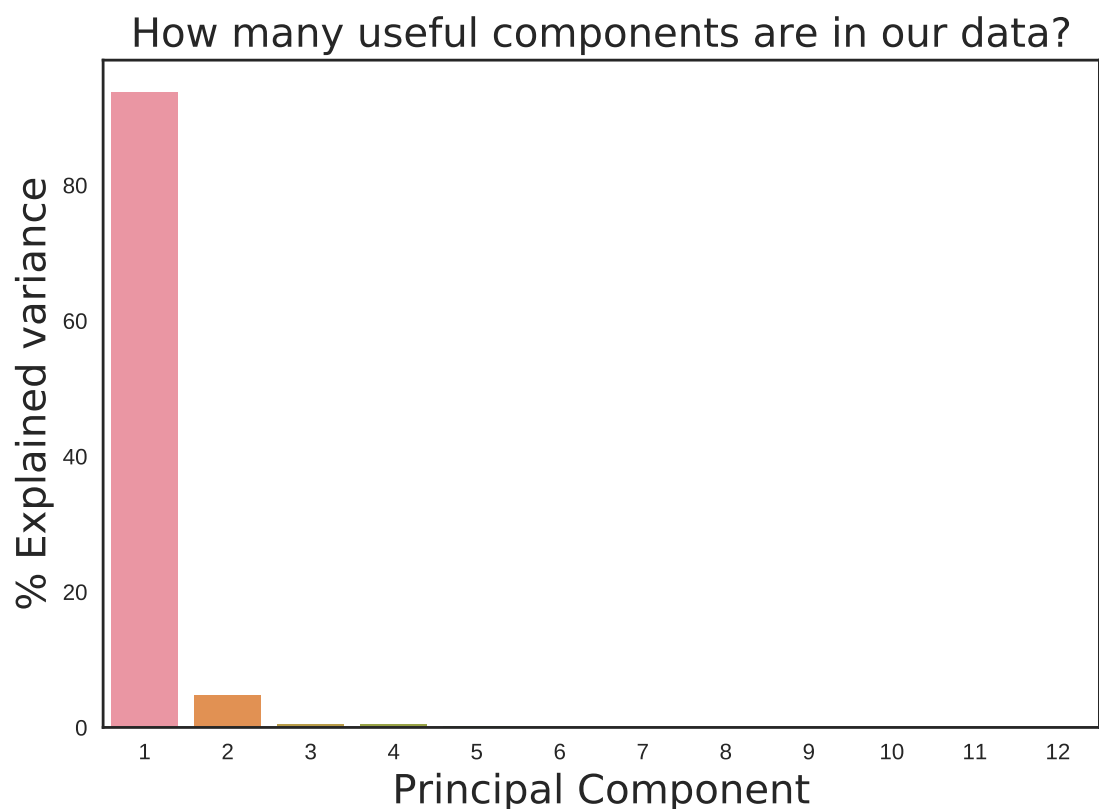


Figure 1: Explained variance decline for principal component analysis performed on a set of 12 all-sky infrared maps. The first three components account for over 99% of the total variance. The PCA fit is performed on the whole sky, after whitening the data, using the “scikitlearn

---

1379 This research made use of Montage. It is funded by the National Science Foundation under  
1380 Grant Number ACI-1440620, and was previously funded by the National Aeronautics and Space  
1381 Administration's Earth Science Technology Office, Computation Technologies Project, under  
1382 Cooperative Agreement Number NCC5-626 between NASA and the California Institute of  
1383 Technology

# 1384 References

- 1385 Ali-Haimoud, Y. 2010, SpDust/SpDust.2: Code to Calculate Spinning Dust Spectra, Astrophysics  
1386 Source Code Library
- 1387 Ali-Haïmoud, Y. 2014, MNRAS, 437, 2728
- 1388 Ali-Haïmoud, Y., Hirata, C. M., & Dickinson, C. 2009, MNRAS, 395, 1055
- 1389 Allain, T., Leach, S., & Sedlmayr, E. 1996a, A&A, 305, 602
- 1390 —. 1996b, A&A, 305, 616
- 1391 Allamandola, L. J., Tielens, A. G. G. M., & Barker, J. R. 1985, ApJ, 290, L25
- 1392 AMI Consortium et al. 2012, MNRAS, 423, 1463
- 1393 Andrews, H., Boersma, C., Werner, M. W., Livingston, J., Allamandola, L. J., & Tielens, A. G. G. M.  
1394 2015, ApJ, 807, 99
- 1395 Andrews, H., Candian, A., & Tielens, A. G. G. M. 2016, A&A, 595, A23
- 1396 Aran, A. B. 2009, PhD thesis, UNIVERSIDAD AUTONOMA DE MADRID
- 1397 Atwood, W. B., et al. 2009, ApJ, 697, 1071
- 1398 Bennett, C. L., et al. 2003a, ApJS, 148, 97
- 1399 —. 2003b, ApJS, 148, 1
- 1400 BICEP2 Collaboration et al. 2014, Physical Review Letters, 112, 241101
- 1401 Bocchio, M., Micelotta, E. R., Gautier, A.-L., & Jones, A. P. 2012, A&A, 545, A124
- 1402 Boggess, N. W., et al. 1992, ApJ, 397, 420
- 1403 Bonnarel, F., et al. 2000, A&AS, 143, 33
- 1404 Bot, C., Ysard, N., Paradis, D., Bernard, J. P., Lagache, G., Israel, F. P., & Wall, W. F. 2010, A&A,  
1405 523, A20
- 1406 Boulanger, F., Baud, B., & van Albada, G. D. 1985, A&A, 144, L9
- 1407 Compiègne, M., et al. 2011, A&A, 525, A103
- 1408 Cunha, K., & Smith, V. V. 1996, A&A, 309, 892
- 1409 de Oliveira-Costa, A., Kogut, A., Devlin, M. J., Netterfield, C. B., Page, L. A., & Wollack, E. J. 1997,  
1410 ApJ, 482, L17
- 1411 de Oliveira-Costa, A., et al. 2002, ApJ, 567, 363
- 1412 Dickinson, C., Paladini, R., & Verstraete, L. 2013, Advances in Astronomy, 2013, 1

- 
- <sup>1413</sup> Doi, Y., et al. 2015, PASJ, 67, 50
- <sup>1414</sup> Draine, B. T. 2011, Physics of the Interstellar and Intergalactic Medium
- <sup>1415</sup> Draine, B. T., & Hensley, B. 2013, ApJ, 765, 159
- <sup>1416</sup> Draine, B. T., & Lazarian, A. 1998a, ApJ, 494, L19
- <sup>1417</sup> —. 1998b, ApJ, 508, 157
- <sup>1418</sup> —. 1999, ApJ, 512, 740
- <sup>1419</sup> Draine, B. T., & Li, A. 2001a, ApJ, 551, 807
- <sup>1420</sup> —. 2001b, ApJ, 551, 807
- <sup>1421</sup> —. 2007a, ApJ, 657, 810
- <sup>1422</sup> —. 2007b, ApJ, 657, 810
- <sup>1423</sup> Duerr, R., Imhoff, C. L., & Lada, C. J. 1982, ApJ, 261, 135
- <sup>1424</sup> Dwek, E. 1986, ApJ, 302, 363
- <sup>1425</sup> Dwek, E., et al. 1997, ApJ, 475, 565
- <sup>1426</sup> Efron, B. 1979, Ann. Statist., 7, 1
- <sup>1427</sup> Erickson, W. C. 1957, ApJ, 126, 480
- <sup>1428</sup> Feigelson, E. D., & Babu, G. J. 2013, Statistical Methods for Astronomy, ed. T. D. Oswalt & H. E. Bond, 445
- <sup>1430</sup> Ferrara, A., & Dettmar, R.-J. 1994, ApJ, 427, 155
- <sup>1431</sup> Finkbeiner, D. P. 2003, ApJS, 146, 407
- <sup>1432</sup> Finkbeiner, D. P., Schlegel, D. J., Frank, C., & Heiles, C. 2002, ApJ, 566, 898
- <sup>1433</sup> Flauger, R., Hill, J. C., & Spergel, D. N. 2014, J. Cosmology Astropart. Phys., 8, 039
- <sup>1434</sup> Galliano, F., et al. 2011, A&A, 536, A88
- <sup>1435</sup> Génova-Santos, R., et al. 2015, MNRAS, 452, 4169
- <sup>1436</sup> Giard, M., Lamarre, J. M., Pajot, F., & Serra, G. 1994, A&A, 286
- <sup>1437</sup> Gillett, F. C., Forrest, W. J., & Merrill, K. M. 1973, ApJ, 183, 87
- <sup>1438</sup> Gillett, F. C., Forrest, W. J., Merrill, K. M., Soifer, B. T., & Capps, R. W. 1975, ApJ, 200, 609
- <sup>1439</sup> Górski, K. M., Hivon, E., Banday, A. J., Wandelt, B. D., Hansen, F. K., Reinecke, M., & Bartelmann, M. 2005, ApJ, 622, 759
- <sup>1441</sup> Haas, M., Klaas, U., & Bianchi, S. 2002, A&A, 385, L23
- <sup>1442</sup> Hanson, D., et al. 2013, Physical Review Letters, 111, 141301
- <sup>1443</sup> Haslam, C. G. T., Salter, C. J., Stoffel, H., & Wilson, W. E. 1982, A&AS, 47, 1
- <sup>1444</sup> Hensley, B. S., & Draine, B. T. 2017, ApJ, 836, 179
- <sup>1445</sup> Hensley, B. S., Draine, B. T., & Meisner, A. M. 2016, The Astrophysical Journal, 827, 45

- 1446 Hoang, T., Vinh, N.-A., & Quynh Lan, N. 2016, ApJ, 824, 18
- 1447 Hony, S., Van Kerckhoven, C., Peeters, E., Tielens, A. G. G. M., Hudgins, D. M., & Allamandola, L. J. 2001, A&A, 370, 1030
- 1449 Hoyle, F., & Wickramasinghe, N. C. 1970, Nature, 227, 473
- 1450 Huang, Y. D. ., et al. 2016, in Proc. SPIE, Vol. 9911, Modeling, Systems Engineering, and Project  
1451 Management for Astronomy VI, 99111V
- 1452 Irfan, M. O., et al. 2015, Monthly Notices of the Royal Astronomical Society, 448, 3572
- 1453 Ishihara, D., et al. 2007, PASJ, 59, S443
- 1454 —. 2010, A&A, 514, A1
- 1455 Israel, F. P., Wall, W. F., Raban, D., Reach, W. T., Bot, C., Oonk, J. B. R., Ysard, N., & Bernard, J. P. 2010, A&A, 519, A67
- 1457 Johnson, H. L. 1966, ARA&A, 4, 193
- 1458 Jones, A. P. 2009, A&A, 506, 797
- 1459 Jones, A. P., Fanciullo, L., Köhler, M., Verstraete, L., Guillet, V., Bocchio, M., & Ysard, N. 2013,  
1460 A&A, 558, A62
- 1461 Jones, A. P., Köhler, M., Ysard, N., Bocchio, M., & Verstraete, L. 2017, A&A, 602, A46
- 1462 Juvela, M., & Ysard, N. 2012, A&A, 539, A71
- 1463 Kalberla, P. M. W., Burton, W. B., Hartmann, Dap, Arnal, E. M., Bajaja, E., Morras, R., & PÃ¶ppel,  
1464 W. G. L. 2005, A&A, 440, 775
- 1465 Kawada, M., et al. 2007a, PASJ, 59, S389
- 1466 —. 2007b, PASJ, 59, 389
- 1467 Kelsall, T., et al. 1998, ApJ, 508, 44
- 1468 Kessler, M. F., et al. 1996, A&A, 315, L27
- 1469 Koenig, X., Hillenbrand, L. A., Padgett, D. L., & DeFelippis, D. 2015, AJ, 150, 100
- 1470 Kogut, A., Banday, A. J., Bennett, C. L., Gorski, K. M., Hinshaw, G., & Reach, W. T. 1996, ApJ,  
1471 460, 1
- 1472 Kondo, T., et al. 2016, AJ, 151, 71
- 1473 Lau, R. M., Herter, T. L., Morris, M. R., Li, Z., & Adams, J. D. 2015, Science, 348, 413
- 1474 Leach, S. M., et al. 2008, A&A, 491, 597
- 1475 Leitch, E. M., Readhead, A. C. S., Pearson, T. J., & Myers, S. T. 1997, ApJ, 486, L23
- 1476 Li, A., & Draine, B. T. 2001, ApJ, 554, 778
- 1477 Lovas, F. J., McMahon, R. J., Grabow, J.-U., Schnell, M., Mack, J., Scott, L. T., & Kuczkowski, R. L.  
1478 2005, Journal of the American Chemical Society, 127, 4345, pMID: 15783216
- 1479 Maddalena, R. J. 1986, PhD thesis, National Aeronautics and Space Administration. Goddard Inst. for  
1480 Space Studies, New York, NY.
- 1481 Maddalena, R. J., & Morris, M. 1987, ApJ, 323, 179

- 1482 Martin, D. C., et al. 2005, ApJ, 619, L1
- 1483 Mathis, J. S., Mezger, P. G., & Panagia, N. 1983, A&A, 128, 212
- 1484 Mathis, J. S., Rumpl, W., & Nordsieck, K. H. 1977, ApJ, 217, 425
- 1485 Mattila, K., Lemke, D., Haikala, L. K., Laureijs, R. J., Leger, A., Lehtinen, K., Leinert, C., & Mezger,  
1486 P. G. 1996, A&A, 315, L353
- 1487 Merrill, K. M., Soifer, B. T., & Russell, R. W. 1975, ApJ, 200, L37
- 1488 Miville-Deschénes, M.-A., & Lagache, G. 2005, ApJS, 157, 302
- 1489 Murakami, H., et al. 1996, PASJ, 48, L41
- 1490 —. 2007, PASJ, 59, 369
- 1491 Murdin, P., & Penston, M. V. 1977, MNRAS, 181, 657
- 1492 Neugebauer, G., et al. 1984, ApJ, 278, L1
- 1493 Ochsendorf, B. B., Brown, A. G. A., Bally, J., & Tielens, A. G. G. M. 2015, ApJ, 808, 111
- 1494 Onaka, T. 2000, Advances in Space Research, 25, 2167
- 1495 Onaka, T., Mizutani, M., Tomono, D., Shibai, H., Nakagawa, T., & Doi, Y. 1999, in ESA Special  
1496 Publication, Vol. 427, The Universe as Seen by ISO, ed. P. Cox & M. Kessler, 731
- 1497 Onaka, T., Yamamura, I., Tanabe, T., Roellig, T. L., & Yuen, L. 1996, PASJ, 48, L59
- 1498 Onaka, T., et al. 2007, PASJ, 59, 401
- 1499 Ootsubo, T., et al. 2016, PASJ, 68, 35
- 1500 Paladini, R., Ingallinera, A., Aglizzo, C., Tibbs, C. T., Noriega-Crespo, A., Umana, G., Dickinson,  
1501 C., & Trigilio, C. 2015, ApJ, 813, 24
- 1502 Pavlyuchenkov, Y. N., Kiranova, M. S., & Wiebe, D. S. 2013, Astronomy Reports, 57, 573
- 1503 Perrott, Y. C., et al. 2018, MNRAS, 473, 1157
- 1504 Pettit, E., & Nicholson, S. B. 1922, ApJ, 56, 295
- 1505 —. 1928, ApJ, 68
- 1506 Pilleri, P., Montillaud, J., Berné, O., & Joblin, C. 2012, A&A, 542, A69
- 1507 Planck Collaboration et al. 2011a, A&A, 536, A1
- 1508 —. 2011b, A&A, 536, A20
- 1509 —. 2014a, A&A, 571, A1
- 1510 —. 2014b, A&A, 571, A8
- 1511 —. 2014c, A&A, 571, A12
- 1512 —. 2014d, A&A, 565, A103
- 1513 —. 2016a, A&A, 594, A1
- 1514 —. 2016b, A&A, 594, A10

---

*REFERENCES*

- 1515 —. 2016c, A&A, 594, A25
- 1516 —. 2016d, A&A, 586, A132
- 1517 —. 2017, A&A, 599, A51
- 1518 Puget, J. L., Leger, A., & Boulanger, F. 1985, A&A, 142, L19
- 1519 Purcell, E. M. 1976, ApJ, 206, 685
- 1520 Russell, R. W., Soifer, B. T., & Willner, S. P. 1977, ApJ, 217, L149
- 1521 Sakata, A., Wada, S., Tanabe, T., & Onaka, T. 1984, ApJ, 287, L51
- 1522 Sakon, I., Onaka, T., Ishihara, D., Ootsubo, T., Yamamura, I., Tanabé, T., & Roellig, T. L. 2004,  
1523 ApJ, 609, 203
- 1524 Sellgren, K. 1984, ApJ, 277, 623
- 1525 Sellgren, K., Werner, M. W., & Dinerstein, H. L. 1983, ApJ, 271, L13
- 1526 Sheehy, C., & Slosar, A. 2017, ArXiv e-prints
- 1527 Skrutskie, M. F., et al. 2006, AJ, 131, 1163
- 1528 Sodroski, T. J., Dwek, E., Hauser, M. G., & Kerr, F. J. 1987, ApJ, 322, 101
- 1529 Sodroski, T. J., et al. 1994, ApJ, 428, 638
- 1530 Takita, S., et al. 2015, PASJ, 67, 51
- 1531 Thorwirth, S., Theulé, P., Gottlieb, C. A., McCarthy, M. C., & Thaddeus, P. 2007, ApJ, 662, 1309
- 1532 Tibbs, C. T., et al. 2011, MNRAS, 418, 1889
- 1533 Truemper, J. 1982, 2, 241
- 1534 von Hausegger, S., & Liu, H. 2015, J. Cosmology Astropart. Phys., 8, 029
- 1535 Weingartner, J. C., & Draine, B. T. 2001, ApJ, 548, 296
- 1536 Werner, M. W., et al. 2004, ApJS, 154, 1
- 1537 Wright, E. L., et al. 2010, AJ, 140, 1868
- 1538 Young, E. T., et al. 2012, ApJ, 749, L17
- 1539 Ysard, N., Juvela, M., & Verstraete, L. 2011, A&A, 535, A89
- 1540 Ysard, N., Miville-Deschénes, M. A., & Verstraete, L. 2010, A&A, 509, L1
- 1541 Ysard, N., & Verstraete, L. 2010, A&A, 509, A12